Department of Physics and Astronomy
Heidelberg University

Master thesis in Physics
submitted by

Josef Stauber

born in Starnberg, Germany

Pulse Shape Discrimination for the CONUS Experiment in the sub-keV Regime

This master thesis has been carried out by

Josef Stauber

at the

Max-Planck Institut für Kernphysik

at

Heidelberg University

under the supervision of

Prof. Dr. Dr. h.c. Manfred Lindner

Pulse Shape Discrimination for the CONUS Experiment in the sub-keV Regime

Abstract

The CONUS experiment operates four p-type High Purity Germanium (HPGe) detectors with a total mass of 4 kg to measure Coherent Elastic neutrino Nucleus Scattering (CEνNS) in the fully coherent regime. It is located in close vicinity (17 m) to the reactor core of the nuclear power plant in Brokdorf, Germany. Next to a high neutrino flux and a sub-keV detector energy threshold, a low background is crucial to measure CEνNS with a high sensitivity. A new Data AcQuisition (DAQ) system for the ongoing RUN-5 allows the recording of the pulse shapes for the individual events. The Pulse Shape Discrimination (PSD) method, optimized and further developed in this work, aims to discriminate background events that originate from the outer, semi-active volume of the HPGe diodes. It is based on a rise time (τ) study of each single event. Accounting for the electronic response of the DAQ and preamplifier and by modeling the influence of the noise, trustworthy physical pulses from a function generator are used to calibrate the PSD-cut in the Region Of Interest (ROI) for CEνNS (sub-keV range). Based on a plausible definition of figures of merit the signal efficiencies are optimized to achieve the best sensitivity for CEνNS when applying the PSD-cut. With efficiencies between 94 and 97 %, an average background reduction in all four detectors of about 15 % is achieved within the ROI.

Zusammenfassung

Das CONUS Experiment betreibt vier Punktkontaktdetektoren aus hochreinem Germanium (HPGe) mit einer Masse von 4 kg um kohärente elastische Neutrino-Kern-Streuung (CEνNS) zu messen. Es befindet sich in unmittelbarer Nähe (17 m) des Reaktorkerns des Kernkraftwerk Brokdorfs in Deutschland. Neben einem hohen Neutrinofluss und einer sub-keV Energie Schwelle des Detektors, ist ein niedriger Untergrund essentiell um CEνNS mit einer hohen Sensitivität zu messen. Ein neues Datenerfassungssystem (DAQ) ermöglicht die Aufnahme der Pulsformen der einzelnen Ereignisse für den laufenden RUN-5. Die Pulsform Diskriminations (PSD) Methode, die in diser Arbeit optimiert und weiter entwickelt wurde, zielt darauf ab Untergrundereignisse, die im äußeren, semi-aktiven Volumen der HPGe Diode entstehen, zu klassifizieren und abzuweisen. Es basiert auf der Analyse der Anstiegszeiten (τ) der einzelnen Ereignisse. Unter Berücksichtigung der Impulsantwort der DAQ und des Vorverstärkers und durch die Modellierung des Einflusses des Rauschens, können vertrauensvolle physikalische Pulse von einem Funktionsgenerator benutzt werden um die PSD-Reduzierung in der 'Region Of Interest' (ROI) von CEνNS (sub-keV Bereich) zu kalibrieren. Durch eine plausible Definition des Gütefaktors werden die Signaleffizienzen optimiert um die höchste CEνNS Sensitivität für die PSD-Reduzierung zu erreichen. Mit Effizienzen zwischen 94 und 97 % wird eine mittlere Untergrundreduzierung in allen vier Detektoren von ungefähr 15 % innerhalb der ROI erreicht.

Contents

Chapter 1

Introduction

The Standard Model (SM) as we know it today is not complete. The first concrete evidence yielded the measurement of neutrino oscillations [1] implying tiny neutrino masses, which contradicts the SM. However, many properties of the neutrino are up to now not well understood, e.g. the question whether neutrinos are Dirac or Majorana particles, the mass hierarchy, the absolute mass scale of the neutrino and the existence of sterile neutrinos [2]. The measurement of these properties is very challenging because the neutrino mass is roughly ten orders of magnitude smaller than the lepton mass and the neutrino has no electromagnetic charge and interacts only weakly within the SM [3].
It took 26 years for the first detection of a neutrino after the postulation of Pauli in 1930 [4]. Pauli proposed a neutral particle, which he called at that time 'neutron', in order to explain the continuous beta spectrum. Enrico Fermi renamed it to 'neutrino' (Italian for 'little neutral one') in the first theory of nuclear beta decay in 1933 [5], because in the meantime James Chadwick had measured what we now know as the neutron [6]. The detection of the neutrino was achieved by Reines and Cowan in 1956 via inverse beta decay (IBD) [7] by using a nuclear power plant as antineutrino source. Together with accelerators, nuclear reactors are man-made neutrino sources, but neutrinos are also naturally produced in the sun, atmosphere, supernova explosions or as relic neutrinos from the big bang [8]. Solar neutrinos have first been observed by the Homestake experiment [9] which raised new questions with the so-called solar neutrino problem [10]. With the discovery of the neutrino oscillation the Super-Kamiokande [11] and the SNO [12] experiment brought the explanation of the discrepancy between the measured and the predicted flux of solar neutrinos. Consequently, more attraction from the theoretical as well as experimental side has been drawn towards the mysterious properties of the neutrino particle. Their fermionic nature, i.e. whether they are Dirac or Majorana particles, is investigated through neutrinoless double beta decay (e.g. GERDA [13], LEGEND [14]). The number of experiments investigating the absolute mass (ECHo [15], KATRIN [16], ...) and the search of a CP violation in the leptonic sector accompanied by the mass hierarchy (DUNE [17], Hyper-K [18], JUNO [19], ...) has increased strongly over the last two decades. Furthermore, sterile neutrinos, i.e. neutrinos that interact only via gravity, are investigated (e.g. PROSPECT [20], STEREO [21]) and high energy neutrinos are examined for astronomical purposes (IceCube [22], KM3Net [23], ...). The above mentioned experiments have in common that they all require large detector masses due to the weak coupling of the neutrinos to the particles within the detector (e.g. Super-Kamiokande uses a fiducial volume of 22.5 kilotons [1]).
The Coherent Elastic neutrino Nucleus Scattering (CEνNS) channel has a cross section $3-4$ orders of magnitude larger than the IBD, allowing for smaller detector masses (kg-size). The enhancement of the cross section is due to the interaction with the nucleus as a whole

(quantum-mechanical coherent interaction). This neutrino channel was predicted already in 1974 by D. Freedman [24] inspired by the new discovery of the Z boson during that time. To meet the full coherency condition the neutrinos need to have energies below roughly 10 MeV. Hence, the observable, i.e. the nuclear recoil, becomes very small (keV range) which has been the greatest challenge for the experiments over the last decades. It took over 40 years for the first observation of CEνNS by the COHERENT collaboration with a Spallation Neutron Source at the Oak Ridge National Laboratory in 2017 [25].

The applications of CEνNS are wide: Measuring the nuclear form factor and the Weinberg angle at the MeV scale; the possibility to "look" inside stars and supernovae (SN), as in a core-collapse SN 99 % of the binding energy is emitted by neutrinos [26] which scatter coherently while moving outwards [27]; power plants might use it in the future as an application to reactor monitoring and safe-guard [28]. Although the measurements of CEνNS by COHERENT indicate no deviation from the SM prediction, interesting Beyond the Standard Model (BSM) physics can be done [29–31]. For direct dark matter detection experiment limits are set by the so-called neutrino floor, i.e. background due to coherent neutrino interactions [32–34].

As of yet, COHERENT is the only running experiment using neutrinos from accelerators, while all other attempts to measure CEνNS use nuclear reactors as neutrino sources. Nuclear reactors produce only one neutrino flavor ($\bar{\nu}_e$) and the neutrino energies are below 12 MeV, thus they interact in the fully coherent regime. The detection technologies used for measuring CEνNS are elaborated, e.g. charge-coupled device (CCD) sensors [35], cryogenic calorimeters [36], liquid scintillator ([37]) and High-Purity Germanium (HPGe) crystals [38]. The latter technique is used by the COherent elastic Neutrino nUcleus Scattering (CONUS) experiment which operates four 1 kg HPGe detectors. It is set up at 17.1 m distance from the reactor core of the commercial power plant in Brokdorf, Germany. With a 3.9 GW thermal power of the reactor the electron antineutrino flux reaches $2.3 \times 10^{13}\,\mathrm{s}^{-1}\,\mathrm{cm}^{-2}$ at the detectors. The CONUS experiment has set competitive limits of CEνNS with Germanium (Ge) [39], but a significant signal is yet to be detected.

Further improvements of the experiment need to engage at one of the three following experimental challenges: A high neutrino flux, a sufficiently low energy threshold (sub-keV) and a low background level. Within the CONUS experiment the neutrino flux cannot be increased anymore since the reactor has a maximum power of operation and there is no suitable location closer to the core. The other two points, however, can be improved. In May 2021 RUN-5 started with a new Data AcQuisition system (DAQ) by CAEN [40] which is expected to lower the noise threshold in comparison to the previous Lynx DAQ [41]. Even more importantly for this work, the CAEN allows to record the pulse shapes of the events. By analyzing and characterizing them one is able to reject 'unwanted' background events, thus improving the signal-to-background ratio. This is called Pulse Shape Discrimination (PSD).

For (p-type) HPGe detectors operating at low energies and with an inactive wrap-around dead layer, surface background events represent a big challenge. However, surface events

have a characteristic pulse shape since the charges released in this semi-active regime (so-called transition layer) between dead and fully active volume result in slower rise times compared to those generated in the fully active regime.
Neutrinos interact homogeneously within the detector and, therefore, within the active and the semi-active volume. Background events, especially coming from particles with small absorption length (e.g. electrons or low energetic photons), are likely to occur in the outer layer. Hence, the signal-to-background ratio is much smaller in the transition layer compared to the active volume making a rejection of the slow pulses highly relevant.
The PSD for Ge detectors has already been investigated by other experiments [42–46]. For the CONUS experiment Jakob Henrichs conducted substantial preliminary studies by developing a pulse shape analysis in [47]. The parameter used to discriminate slow and normal pulses is obtained from a fit to the individual pulses. This work is built upon [47] and develops the methods further. Artificially generated pulses, modeling the real pulses from the detector, are injected via a function/pulse generator into the electronics chain directly after the diode. This allows a more precise characterization of the discrimination of the normal and slow pulses in the low energy regime. Furthermore, a tool to generate the detector specific noise is used to investigate the influence of the noise on the pulse shapes and to estimate the uncertainties of the PSD-cut. The method is applied on RUN-5 data (May 2021-August 2022) and is implemented in the analysis chain to be used by the collaboration for the upcoming data release.

Chapter 2

Foundations

The Coherent Elastic neutrino Nucleus Scattering (CEνNS) cross section is greater than the cross section of inverse beta decay (IBD), nonetheless most experiments nowadays still use IBD to detect neutrinos. This apparent contradiction gets clarified in the first section (2.1), which introduces the basics of CEνNS. The suitable neutrino sources and target materials to measure CEνNS are examined in section 2.2. Furthermore, the CONUS experiment and the measured results so far are introduced in section 2.3. The functionality of high-purity germanium (HPGe) detectors (used by CONUS) is explained in the last section of this chapter (2.4).

2.1. Coherent Elastic neutrino Nucleus Scattering (CEνNS)

Neutrinos interact with matter via the weak interaction (neglecting gravity) mediated by a $W^{\pm}$ or a Z boson. The $W^{\pm}$ boson is electrically charged ($\pm 1e$) and the Z boson carries no (electromagnetic) charge. The widely experimentally used IBD ($p + \bar{\nu}_e \rightarrow n + e^+$) is a charged current with a W boson as the mediator. The Feynman diagram is displayed in figure 2.1a. In the CEνNS channel the quantum numbers of the initial particles do not change, only energy and momentum is transferred ($A + \bar{\nu} \rightarrow A + \bar{\nu}$). Hence, the vector boson Z is the exchange particle and the process is called neutral current. The corresponding Feynman diagram is shown in figure 2.1b.
In figure 2.2 it can be seen that the cross sections of the CEνNS process is the highest among the various neutrino interaction channels, at the MeV-scale it amounts to roughly 10^{-16} barn. For comparison, the cross section for the corresponding electromagnetic process with a MeV-scale photon is around 0.1 barn [48]. By looking at figure 2.2 the question arises why is it experimentally easier to detect neutrinos via IBD. Reines and Cowan were measuring neutrinos via this channel in the first neutrino detection in 1956 [7]. The answer

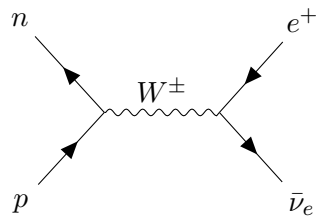

(a) IBD: an electron antineutrino $\bar{\nu}_e$ scatters off a proton, creating a positron and a neutron mediated by a vector boson $W^{\pm}$.

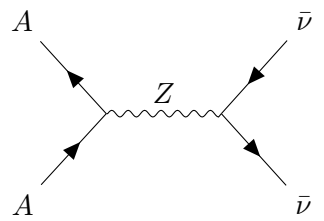

(b) CEνNS: an antineutrino $\bar{\nu}$ scatters off a nucleus A mediated by the neutral Z boson.

Figure 2.1. Feynman diagram of IBD (left) and CEνNS (right) with antineutrinos.

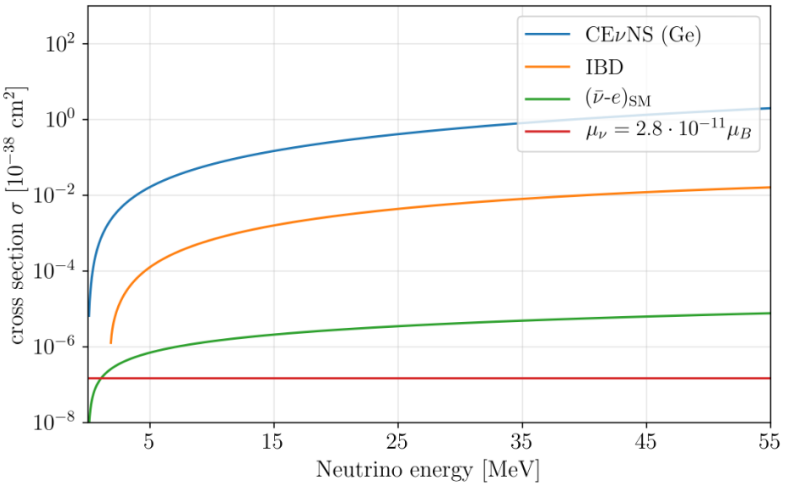

Figure 2.2. SM and BSM neutrino interaction cross sections below 55 MeV. The CEνNS cross section for Ge exceeds the one for IBD and electron neutrino scattering by orders of magnitude. The IBD has a threshold of $E = 1.8\,\mathrm{MeV}$ [49]. The neutrino magnetic moment is marked by the current best limit [50]. The plot is taken from [51].

lies in the measurable observable. In the case of the IBD the produced particles leave a unique signature. The positron promptly interacts with a nearby electron producing two photons ($e^+ + e^- \rightarrow 2\gamma$). The neutron gets captured after typically a few 10-100's µs by an appropriate nucleus releasing a characteristic gamma-ray. Reines and Cowan used water as a detecting material (hydrogen atoms consist of a single proton as a nucleus) and Cadmium as a neutron capture ($n + {}^{108}\mathrm{Cd} \rightarrow {}^{109m}\mathrm{Cd} \rightarrow {}^{109}\mathrm{Cd} + \gamma$) [7]. The unique coincidence photon signature can be measured via liquid scintillators and photomultiplier tubes.

For CEνNS, however, the observable is only the nuclear recoil [30]. The maximum nuclear recoil energy of the nucleus with mass m_A after interacting with a neutrino of energy E_ν is given by

$$T_{\max} = \frac{2E_\nu^2}{m_\mathrm{A} + 2E_\nu}. \tag{2.1}$$

Hence, to increase the nuclear recoil energy it is favorable to reduce the mass of the nucleus. However, by reducing m_A the cross section of the process gets also lowered, as can be seen in the differential cross section, where Z and N are the proton and neutron number of the nucleus, respectively:

$$\frac{d\sigma}{d\Omega} = \frac{G_f^2}{16\pi^2}\Big(N - \big(1 - 4\sin^2\theta_W\big)Z\Big)^2 E_\nu^2(1+\cos\theta)F^2(Q^2). \tag{2.2}$$

G_f denotes the Fermi constant and θ is the scattering angle. θ_W denotes the Weinberg angle and $\sin^2\theta_W \approx 0.23$ [3]. This small value implies that the dependence on Z is sub-dominant in comparison to N. F as a function of the momentum transfer Q is the nuclear form factor which describes the spatial extension of the target nucleus seen by the neutrino. Furthermore, it reflects the coherency of the scattering, e.g. for a fully coherent process the

nucleus is seen point-like and $F = 1$. The wavelength of the Z boson, which corresponds to the momentum transfer, needs to match the size of the nucleus, in order for it to be seen as point-like, i.e. interact fully coherently. Translating this so-called coherency condition into the neutrino energies, we get

$$E_\nu \leq \frac{1}{2R_A} \approx \frac{197}{2.5\sqrt[3]{A}}[\text{MeV}], \tag{2.3}$$

where R_A corresponds to the radius of the nucleus. For Germanium ($A = 32$) it yields a neutrino energy $\lesssim 20\,\text{MeV}$ to be in the coherent regime. Neglecting the Z dependence (2.2) results in a characteristic $\sigma \propto E_\nu^2 N^2$. To fulfill the coherency condition together with a large cross section and a high nuclear recoil energy (2.1), the neutrino energy E_ν and the target nucleus need to be balanced well. The different suitable neutrino sources as well as target nuclei will be discussed in the next section (2.2).

Although neutrinos have already been successfully detected via IBD, the detection of CEνNS is of great interest for various reasons. First of all, by validating the existence of this channel the SM gets confirmed. Furthermore, neutrinos have already been proven to contradict the SM because of their non-vanishing mass, thus looking for Beyond the Standard Model (BSM) physics via the CEνNS channel is suggestive. With highly precise measurements one would be able to determine the Weinberg angle θ_W and the nuclear form factor $F(Q)$ as parameters of (2.2). Via CEνNS the Weinberg angle could be measured in an energy region (MeV scale) where not many measurements have been conducted so far [52]. The most precise measurements are done at large colliders at much higher energies ($\sim 100\,\text{GeV}$), where θ_W is determined from the measured W to Z mass ratio [53]. The form factor with respect to the momentum transfer, which itself is proportional to the neutrino energy, can be measured via CEνNS using different neutrino energies. This enables the investigation of the form factor without taking any strong or electro-magnetic effects into consideration [54].

CEνNS also plays a major role in an astrophysical phenomenon, namely in supernovae (SN). During a SN explosion around 99 % of the gravitational binding energy gets released in neutrinos [26]. While travelling out of the highly dense matter the neutrinos scatter frequently with the nuclei, thus CEνNS needs to be considered when building models for SN explosions. Experiments aiming to directly detect Dark Matter (DM) look for recoils induced by DM particles [55]. These events, however, cannot be distinguished from nuclear recoils induced by neutrinos, the so-called neutrino floor consisting of CEνNS from solar, atmospheric or SN neutrinos. The ^{8}B solar neutrinos are almost within the reach of detection by the new generation of experiments [34]. On the one hand it is an unwanted background while searching for dark matter, but on the other hand one gains knowledge about the detector response to nuclear recoils.

If the measured CEνNS event rate differs from the predicted one that could also hint towards BSM physics. Non-standard neutrino quark and exotic neutral current interactions can be considered by introducing new couplings in (2.2) [30, 31]. Furthermore, the measurement

of a finite magnetic moment of the neutrino would indicate new physics [56]. The current CEνNS experiments constrain these properties and maybe in the future a new property suggesting BSM physics will be discovered [31, 50, 57].

2.2. Neutrino sources and target materials

There are two different types of man-made neutrino sources considered for CEνNS experiments:

- nuclear reactors
- π decay at rest (π-DAR) sources

To maximize the nuclear recoil (2.1) a high neutrino energy is favorable, but at the same time the neutrino energy is constrained by the coherency condition (2.3). This makes neutrinos in the MeV range the most suitable candidate for CEνNS. A well-known spectral shape is crucial as well as a high neutrino flux to enhance statistics [58]. An advantage of the man-made over natural sources is the possibility of turning the reactor/beam off, thus helping in background discrimination. Because of the controllability of the source together with the suitable energies and fluxes all CEνNS experiments so far have used either neutrinos coming from nuclear power plants [59] or from π-DAR [60] sources.
In [61] using ^{51}Cr as a neutrino source to measure CEνNS has been proposed. The advantages would be mono energetic neutrinos (2 lines at ca. 750 keV), the short distance to the source and the possibility of choosing a location with good background suppression (e.g. deep underground). However, creating such a source is very challenging and the nuclear recoils are even smaller than for reactor neutrinos. In the following the neutrino production in reactors and π-DAR sources will be explained, starting with the latter.

π-DAR sources

Until today only the COHERENT collaboration uses neutrinos coming form a π-DAR source to measure CEνNS [62]. It utilizes the Spallation Neutron Source (SNS) in Oak Ridge (USA) where high-energy ($\mathcal{O}$(GeV)) proton pulses are shot onto a mercury target. Neutrons are generated through spallation and, more importantly for us, also pions. The π mesons are stopped within the mercury. While the π^- mesons get captured, the π^+ decay according to $\pi^+ \rightarrow \mu^+ + \nu_\mu$ and microseconds later the μ^+ decay ($\mu^+ \rightarrow e^+ + \nu_e + \bar{\nu}_\mu$). Overall, monoenergetic ν_μ and a continuous spectrum of ν_e and $\bar{\nu}_\mu$ is generated. The monochromatic peak is at 30 MeV and the continuous spectrum reaches energies up to 52.6 MeV. The SNS at Oak Ridge is currently the strongest π-DAR neutrino source in the world with an approximate flux of $4.3 \times 10^7\,\mathrm{s}^{-1}\,\mathrm{cm}^{-2}$ at 20 m distance from the mercury target [62].

Nuclear reactors

At a nuclear reactor only one flavor of neutrinos is produced ($\bar{\nu}_e$). They are created via β^--decay of nuclear fission products, resulting in neutrino energies below 12 MeV[1]. Hence, they are in the fully coherent regime when using a Ge target. In a typical reactor approximately 3×10^{19} fissions happen per GW thermal power per second and on average 7.2 neutrinos are produced per fission, resulting in a neutrino emission of $2 \times 10^{20}\,\mathrm{GW}^{-1}\,\mathrm{s}^{-1}$ [64].
By comparing both neutrino sources, one notices the following differences. At a distance of 20 m the neutrino flux from the reactor, which is proportional to r^{-2}, is roughly $10^{13}\mathrm{s}^{-1}\,\mathrm{cm}^{-2}$ which is around six orders of magnitude higher than from the π-DAR source. Furthermore, reactor neutrinos have lower energies and, therefore, are within the fully coherent regime (see (2.3)), whereas neutrinos from π-DAR sources have higher energies resulting in higher nuclear recoils through (2.1). Due to the latter point the COHERENT collaboration managed to detect CEνNS with two different target materials [25, 65]. In the following we will discuss the suitable target materials for a CEνNS detection.
Formula (2.2) ($\sigma \propto N^2$) and (2.1) ($T_{\max} \propto (N+A)^{-1}$) result in a 'push-pull' situation when looking for the right target nucleus. Typically, isotopes with intermediate neutron numbers are chosen to find a compromise between enhanced cross section and still detectable nuclear recoils. In table 2.1 there is a collection of CEνNS experiments with their respective neutrino source, target material and detection technique. This list should only illustrate the various approaches of the different experiments to detect CEνNS and is not exhaustive. For more details on the detection techniques we refer to the corresponding cited paper. The concept of HPGe semiconductors will be introduced in section 2.4 since it is used by CONUS.

Experiment	ν-source	Target isotope	Detection technique
COHERENT [25]	π-DAR	CsI[Na]	Solid Scintillator
COHERENT [65]	π-DAR	Ar	Liquid Noble Gas
CONUS [38]	Reactor	Ge	HPGe Semiconductor
CONNIE [66]	Reactor	Si	CCDs
νGen [67]	Reactor	Ge	HPGe Semiconductor
TEXONO [68]	Reactor	Ge	HPGe Semiconductor
RED-100 [69]	Reactor	Xe	Liquid Noble Gas
ν-CLEUS [70]	Reactor	$CaWO_4$ and Al_2O_3	Cryogenic calorimeter

Table 2.1. An exemplary list of CEνNS experiments with their used ν-source, target isotope and detection technique. So far only the COHERENT experiment has successfully detected a CEνNS signal using sodium doped cesium iodide (CsI[Na]) [25] and Argon (Ar) [65] as target materials.

[1] Recently [63] measured reactor antineutrinos above 10 MeV.

Using (2.1), 10 MeV neutrinos yield a maximum recoil energy of a Ge or Silicon (Si) nucleus of approximately 3 and 7 keV [2]. These nuclear recoils are not measured directly, but the secondary processes like ionization or scintillation. Unfortunately, during this conversion a fraction of energy is lost due to dissipative processes (e.g. phonons). The ratio of ionisation energy (in terms of electron equivalents) E_{ee}, which can be measured by HPGe detectors, to the nuclear recoil energy E_{nr} is described by the quenching factor Q. Lindhard et al. [71] developed a theoretical description for this phenomenon already in 1965. The dependence of the quenching factor on the nuclear recoil energy is described by the parameter k which roughly corresponds to the quenching factor at $1\mathrm{keV}_{\mathrm{nr}}$. At higher energies ($10 - 100\mathrm{keV}_{\mathrm{nr}}$) it has been well measured and shown to coincide with the Lindhard theory [72]. However, at energies concerning CEνNS (few keV) the measurements are more challenging. With [73] a very precise measurement has been conducted recently in the energy region of interest. From this data a quenching factor of approximately 0.2 at 3 keV nuclear recoil energy can be taken, resulting in ionisation energies about $600\mathrm{eV}_{\mathrm{ee}}$. This demonstrates the absolute necessity of low energy thresholds for detecting CEνNS signals in the fully coherent regime.

2.3. The CONUS experiment

2.3.1. The experimental site

The CONUS experiment aims to detect CEνNS in the fully coherent regime using reactor antineutrinos. It is located within the safety containment of the nuclear power plant in Brokdorf, Germany (Kernkraftwerk Brokdorf, KBR), more precisely in room A-408, 17.1 m away from the reactor core as can be seen in figure 2.3. The nuclear power plant is owned and operated by the PreussenElektra GmbH [74]. As one of the last active power plants in Germany it was shut down at the end of the year 2021. While running it had a maximum thermal power of $3.9\,\mathrm{GW}_{\mathrm{th}}$ which leads to a $\bar{\nu}_e$-flux of $2.3 \times 10^{13}\,\mathrm{s}^{-1}\,\mathrm{cm}^{-2}$ at the detectors [38]. Once a year the reactor was shut down for approximately one month for maintenance and fuel reloading. These so-called outages were always welcome for the experiment, because they allowed us to take reactor-OFF data. Since the start of the experiment in April 2018 four RUNs have been completed with optimisations in between (e.g. environment or DAQ), for more details we refer to table 1.1 in [51]. The current RUN-5 has started in May 2021. Hence, seven months of reactor-ON data have been collected and at the moment (August 2022) reactor-OFF data is measured. Because the dismounting of the power plant is not starting before 2023, a sufficient amount of reactor-OFF data will be collected.

[2] It depends also on the chosen isotope.

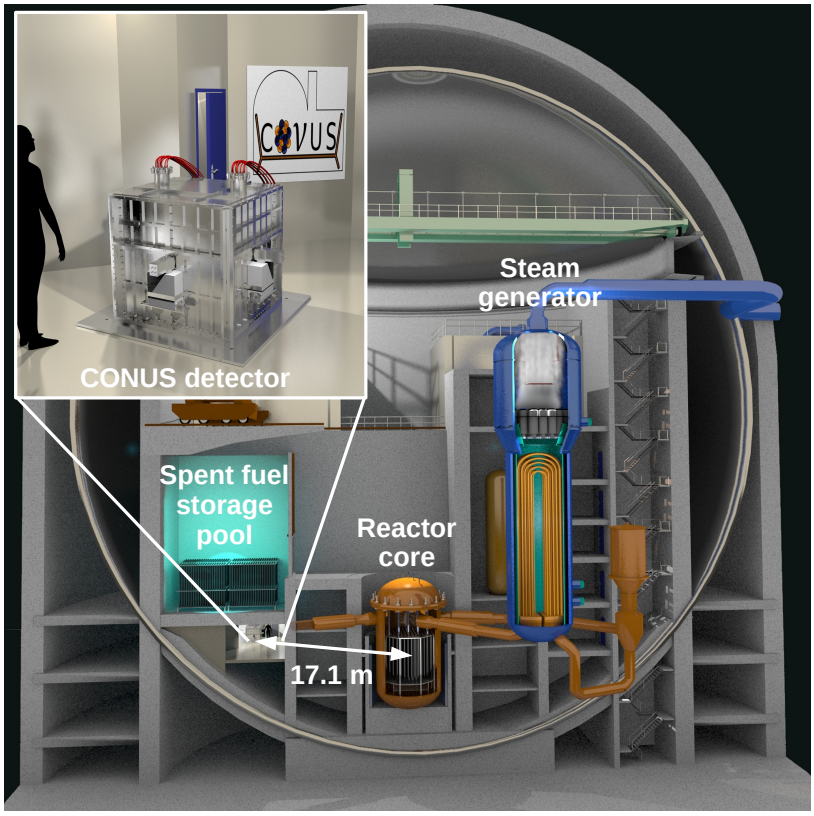

Figure 2.3. Schematic view of the CONUS experiment within the nuclear power plant in Brokdorf (KBR). The room A-408 where the CONUS detector is located is shown in the enlarged image. Courtesy by G. Vogt (MPIK).

2.3.2. Experimental challenges

To achieve stable conditions at the reactor site is very challenging, because the room is by no means a laboratory. Unstable environmental conditions like temperature, no remote access from outside the reactor and other security restrictions complicate the work. The spent fuel storage pool is located above the experiment (see figure 2.3) which yields together with the concrete an overburden of 10 - 45 m water equivalent (w.e.) depending on the azimuth angle [39]. This shields some cosmic rays, but a sophisticated shield to further suppress background is still an absolute necessity. For comparison, the Laboratori Nazionali del Gran Sasso in Italy are located deep underground ($\sim$ 3800 m w.e.) to shield their neutrino and dark matter experiments against cosmic ray particles [75].
For a successful detection of a CEνNS signals mainly three parameters need to be optimized. First, a strong neutrino flux to get sufficient statistics is required. Second, a low energy threshold, because of the low measurable ionisation energies due to quenching and, last, a low, stable and well understood background level is necessary [51]. Therefore, a sophisticated shield has been developed, which will be discussed briefly in the next section. For more details we refer to [51]. The figure 2.4 illustrates the importance and the conjunction of the three optimization parameters.

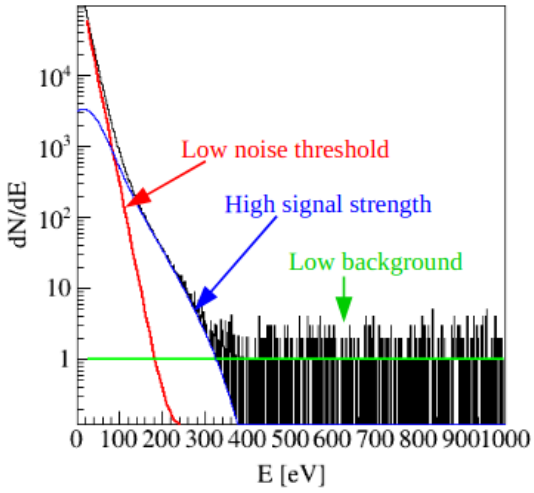

Figure 2.4. Illustration of the interplay of the three main experimental challenges for a successful CEνNS detection. A high neutrino flux (blue), a low energy threshold (red) and a low background (green) are crucial. The plot is taken from [47].

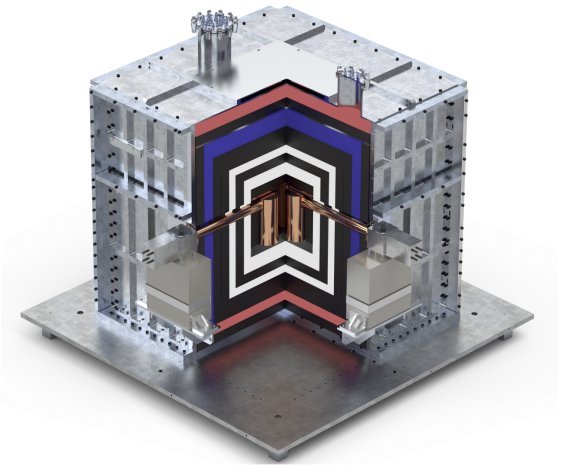

Figure 2.5. Display of the shield design for the CONUS detectors. Inside the silver steel cage are black lead layers, red PE layers, white borated PE layers and the active muon veto in blue. The four HPGe detectors (bronze) are in the middle and connected via the cooling fingers to the cryocoolers at the outside of the steel cage. Courtesy by the construction office of MPIK.

2.3.3. Background in CONUS

The Max-Planck-Institut für Kernphysik (MPIK) has a long experience in understanding background sources as well as suppressing them [76]. GIOVE (Germanium Inner Outer VEto) is a high-purity germanium spectrometer which has been developed by the MPIK and is used for material screening [77]. The shield developed for CONUS is based on the shield design of GIOVE. Figure 2.5 shows the structure of the CONUS shield.
It displays an onion-like structure with various layers of different materials. There are five layers of lead (Pb) to shield effectively against γ-ray background. The Pb closer to the middle (i.e. the detectors) has a higher radiopurity in order to avoid radioactive decays close to the detectors. The innermost layer of Pb bricks has an activity of the problematic ^{210}Pb of less than $0.2\,\mathrm{Bq\,kg^{-1}}$ [78, 79]. Besides the total thickness of 25 cm from the five Pb layers, further polyethylene (PE) layers are incorporated. The outer layer (5 cm) is to moderate neutrons coming from the outside, whereas the inner layers (10 cm) are borated to capture the moderated neutrons and neutrons induced by cosmic ray muons inside the Pb. Besides these so-called passive shielding layers there is an active muon anticoincidence system ('muon-veto') installed in form of plastic scintillator plates equipped with photomultiplier tubes (PMTs).
Because the experiment is at relatively shallow depth, the muon flux from cosmic rays is still high and the muon veto is highly necessary. Furthermore, the plastic scintillator plates act as another layer to moderate neutrons. More information about the neutron

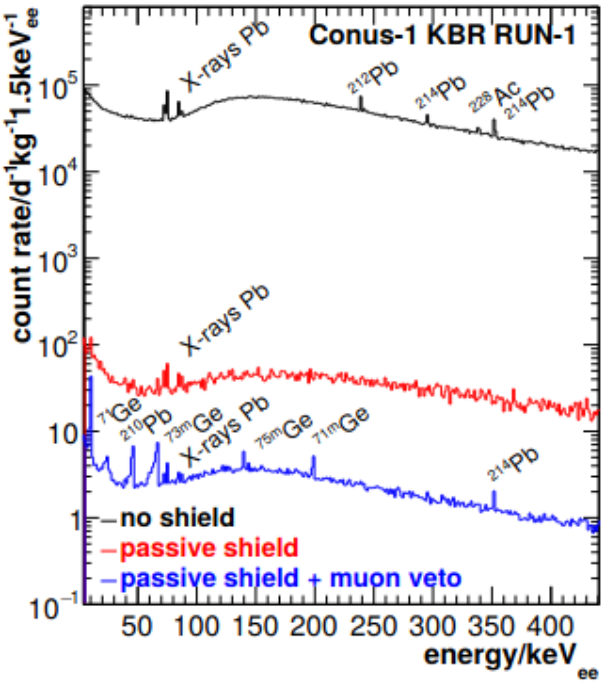

Figure 2.6. Illustration of the background suppression achieved by the CONUS shields. Without any shielding (black spectrum) lines of natural radioactivity are visible. Muon induced background dominates the red spectrum with only the passive shield. When applying the active and passive shield (blue spectrum) lines from decays of metastable states within the Ge crystal become visible. Overall, the shield design achieves a background suppression of approximately four orders of magnitude. The plot is taken from [78].

induced background can be found in [80]. A steel cage around the shield ensures on the one hand earthquake safety requirements that must be fulfilled and on the other hand it helps in the process of air-borne radon suppression. The radon within the steel cage is mitigated by constantly flushing the inside with 'radon-free' air, i.e. air that was stored for an appropriate amount of time. In total, the shield has a mass of roughly 11 tons and a volume of 1.65 m^3, making it extremely compact and fitting in the rather small room A408. Altogether, the shield suppresses the background around four orders of magnitude as can be seen in figure 2.6.

Reactor-correlated background

Apart from lowering the background, good knowledge about the origin of the background is crucial. In particular, reactor-correlated background could be mistaken for CEνNS events. Dedicated campaigns have been conducted to investigate the reactor-correlated neutron and γ background at the start of the experiment and in the second half of 2018, respectively. Neutrons are produced in the fission reactions within the reactor core. γ-rays come from the decay of ^{16}N which is produced by neutrons and transported through the cooling water cycle close to the experiment. More details about the neutron induced background can be found in [80]. There it is concluded that the reactor-correlated neutrons are negligible compared to muon induced neutrons and most importantly to expected CEνNS signals.

Cosmic Activation

Another source of background comes from cosmic activation of the Ge and the copper (Cu) parts. Activation happens when hadrons, e.g. from cosmic rays, induce spallations within the material and, thereby, producing radioactive isotopes which later decay. Thus, keeping the time that the materials spend above ground should be minimized as much as possible to avoid cosmic activation. During manufacturing and transport it is sometimes impossible to store them underground. In the case of the CONUS materials Ge was activated on average for 98 d and the Cu parts for 102 d [38]. An overburden of roughly 10 m w.e. already shields the hadronic fraction of the cosmic rays, therefore we do not have to worry about any activation at the experiment site (> 15 m w.e.).

Overall the background is well understood and described by an elaborate model via Monte-Carlo (MC) simulations [51, 78]. In the sub-keV$_{ee}$ range a stable background rate in the order of $10\,\mathrm{d}^{-1}\,\mathrm{kg}^{-1}$ is achieved [38, 51]. The pulse shape discrimination (PSD) is a further tool to suppress background. It is an active discrimination technique which utilizes characteristic features of the events. The new Data AcQuisition system (DAQ) module V1782 by CAEN (abbreviated with CAEN in the following) [40] made the development of the PSD method possible, because it allows the recording of pulse shapes. It is in operation since the beginning of RUN-5 in May 2021.

2.3.4. Results of the CONUS experiment

The first CEνNS search results have been published in February 2021 using 248.7 kg d reactor-ON and 54.8 kg d reactor-OFF data from RUN-1 and RUN-2 [39]. It set the best limit for CEνNS (SM) interaction in the fully coherent regime obtained from reactor antineutrinos. In figure 2.7 the 90%-Confidence Limit (C.L.) can be seen as a function of the k parameter which describes the energy dependence of the quenching factor. The limit is shown with respect to this parameter, because the effect on the CEνNS event rate is enormous. To get a more precise knowledge of the quenching parameter, the CONUS collaboration together with the Physikalisch-Technische Bundesanstalt (PTB) Braunschweig conducted a dedicated measurement [73]. In the nuclear recoil energy range of $[0.4, 6.3]$ keV$_{nr}$, data are compatible with the Lindhard theory with a k-value of $k = 0.164 \pm 0.004$. Translated into figure 2.7 this corresponds to a limit (blue dot) 17 times larger than the predicted value (red dot).
Furthermore, two publications looking for BSM physics with the CONUS data have been released [56, 57]. [57] investigates vector and scalar mediators and sets the world's best limits on tensor non-standard interactions (NSIs) in the neutrino-quark sector. Upper limits for the effective neutrino magnetic moment ($\mu_\nu < 7.5 \times 10^{-11} \mu_B$) and the millicharge ($q_\nu < 3.3 \times 10^{-12} e_0$) were determined at 90 % C.L. in [56].

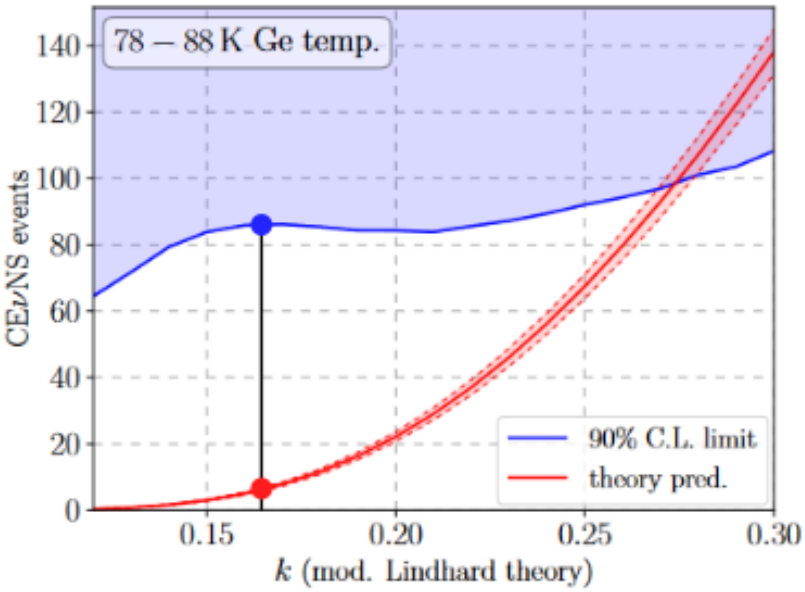

Figure 2.7. Result of the CEνNS analysis of RUN-1 and RUN-2. The 90 % C.L. upper limit on the number of CEνNS events (blue curve) and the theoretically predicted count rate (red) is plotted with respect to the quenching parameter k. The blue and red dot indicate the intercept with the measured k-value from [73]. The plot is taken from [39].

2.4. High Purity Germanium (HPGe) detectors

In this section the working principle of HPGe semiconductor detectors is explained. Besides Germanium, crystalline silicon (Si) is the most commonly applied material for low threshold semiconductor detectors.

The special property of a semiconductor compared to a conducting metal is the existence of a band gap which in turn is small compared to the band gap of a non-conducting insulator ($E_{g,\text{insulator}} > 10\,\text{eV}$) [81]. The energy gap for Ge is $E_g = 0.67\,\text{eV}$ at the liquid nitrogen temperature of $T = 77\,\text{K}$ which can be overcome by thermally excited electrons [51]. So-called doping increases the number of free charge carriers, i.e. e^- in the conduction band or holes in the valence band, by implementing single atoms from different elements into the crystal structure. Donor atoms, e.g Lithium (Li), increase the number of free electrons while acceptor atoms, e.g. Boron (B), enhance the number of free holes. After these doping processes the semiconductor is called n-type (Li) or p-type (B) material, respectively.

By bringing both types into contact a so-called pn-junction is formed as can be seen in figure 2.8 (a). The free charge carriers diffuse to the other side and recombine in the middle, generating the so-called depletion region with an electric field. By applying an external high voltage in reverse bias the depletion region can be extended over the entire Ge volume transforming it into a diode as seen in figure 2.8 (b). Without the pn-junction there would be a constant current, so-called leakage current, which overrules any charges generated through an interaction.

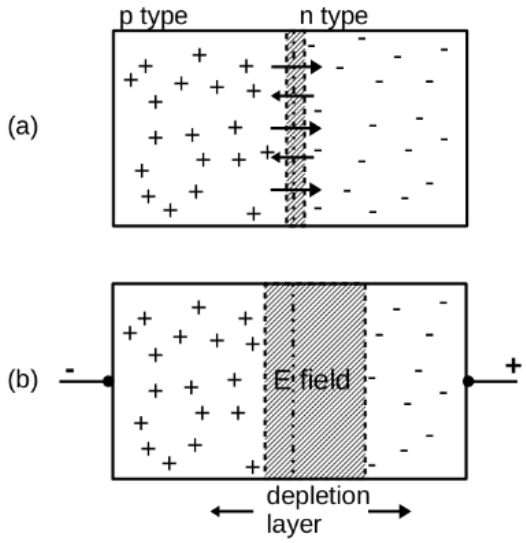

Figure 2.8. In figure (a) p-type and n-type semiconductor materials are brought into contact forming a pn-junction. In figure (b) an external HV in reverse bias increases the depletion layer and the electric field. The plot is taken from [51].

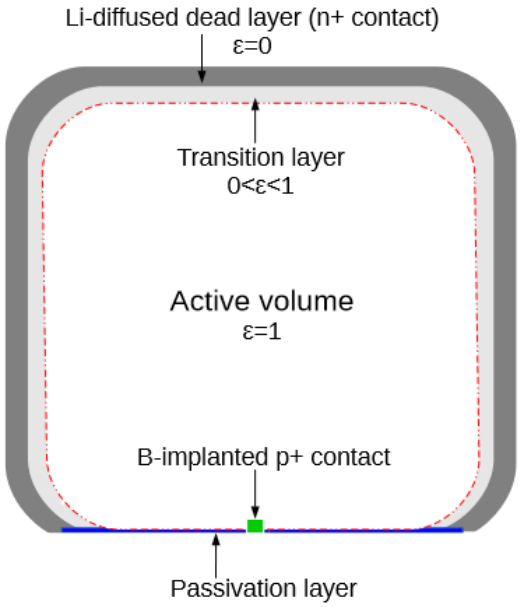

Figure 2.9. PPC HPGe diode design used in the CONUS experiment. The various layers with their corresponding charge collection efficiency ϵ are shown. Between the n+ and the p+ contact the HV is applied. The passivation layer insulates the two contacts. The plot is taken from [38].

Germanium is a preferred material due to the intrinsic high purity, e.g. the CONUS detectors achieve approximately one impurity atom per 10^{12} Ge atoms. This enables a HV of only a few kV to fully deplete the detector (CONUS detectors use $2.8 - 3.4$ kV). Moreover, it lowers the risk of charge trapping, thus a high charge collection efficiency (ϵ) can be achieved. The good energy resolution in Ge detectors is due to the small energy needed to create electron-hole pairs (2.96 eV at 77 K). An operation at liquid nitrogen temperatures is necessary to reduce the leakage current due to thermal excitations. This brief overview over semiconductors and HPGe detectors followed the book [81] which is strongly recommended for more detailed information.

2.4.1. CONUS detector design and characteristics

Due to safety restrictions at the KBR, CONUS is using electrical instead of liquid nitrogen cryocoolers to achieve the required low temperature ($\approx$ 77 K) [82]. The cryostats are made of radiopure, electrolytically produced Cu which are connected to the diodes via an extended cooling arm ($>$ 40 cm) through the shield. The cooling system and the detectors were designed in close cooperation with Mirion Technologies, Canberra, in Lingolsheim [83]. For more precise information on the cryostats we refer to [38, 51]. The following describes the design of the Germanium diode used in CONUS as well as the characteristics of the detectors.

The design of the p-type point-contact (PPC) detector used in CONUS can be seen in figure 2.9. The cylindric diode has a height and a diameter of 62 mm. It consists of a Li-diffused layer (n+ contact) surrounding the detector with a thickness of $\sim 1\,\text{mm}$. The B-implanted p+ contact is at the bottom with a diameter of only a few millimeters. Between the p+ and n+ contact is a $\sim 100\,\text{nm}$ thick passivation layer functioning as an insulator. Charges created in the outer layer are directly trapped by the Li-atoms, thus they are not registered, i.e. the charge collection efficiency $\epsilon = 0$ [3]. On the other hand, interactions within the fully depleted region (active volume) are completely recorded ($\epsilon = 1$). Because the Li-atoms diffuse out of the dead layer into the active volume the so-called transition layer with $0 < \epsilon < 1$ and a thickness of $\sim 0.2\,\text{mm}$ is formed. The pulses from events within this layer are called in the following 'slow pulses', whereas pulses originating within the active volume are called 'normal pulses'. A method to discriminate these pulses is the aim of the PSD and main subject to this thesis.
CONUS operates four PPC HPGe detectors which are called CONUS-1 to CONUS-4 or abbreviated C1 to C4. They achieve an energy threshold of $E \lesssim 300\,\text{eV}_{\text{ee}}$ and a pulser resolution $\lesssim 85\,\text{eV}_{\text{ee}}$ [38]. The mass of each diode is 0.996 kg which results in a total fiducial mass of 3.73 ± 0.02 kg when considering the dead layer. Besides the four detectors at KBR there is a fifth CONUS-5 (C5) at the MPIK. It is used to run R&D and in the making of this thesis various tests have been performed with C5 before applying them to the detectors at KBR. The numbers and information about the detectors are taken from [38] where more details are given.

2.4.2. From the interaction process to the data collection

In this section the process from the signal creation up to the final data, which are read out and saved by the computer, is described.
An interaction within the Ge crystal creates an electron-hole pair if the deposited energy is large enough, i.e. $E \gtrsim 2.96\,\text{eV}$ at 77 K for Ge [81]. The present electric field drifts the electrons and holes towards the p+ (cathode) and n+ (anode) electrodes, respectively. The movement of the charge carrier q induces a charge Q at the read-out electrodes according to the Shockley-Ramo theorem [84]

$$Q(t) = -qW(\mathbf{x}(t)), \tag{2.4}$$

where $\mathbf{x}(t)$ is the trajectory of the charge carrier. $W(\mathbf{x}(t))$ is a dimensionless form of the electrical potential, the so-called weighting potential. In the case of the p-type PC HPGe detector the dimensionless form is achieved by setting the p+ contact to unit and the n+ contact to zero potential [84]. The induced charge increases over time until it is equal to the collected charge q at the p+ contact (readout electrode), i.e. until all charges are collected [85]. Due to impurities charges can get trapped while drifting through the

[3] For this reason the layer is also called 'dead layer'.

crystal [86]. This leads to recombination of electrons and hole ('recombination centre') or trapping of them until they get thermally excited ('charge traps') [85]. Hence, in order to have a good energy reconstruction, i.e. no loss of charges during the drift process, high purity crystals are essential. As already mentioned the CONUS detectors achieve an impurity concentration of approximately 10^{12} Ge atoms per impurity [38].
In figure 2.10 the simulated weighting potential of the C1 detector is depicted. It can be seen that it is sharply peaked at the p+ contact (readout electrode), thus the holes are the main contribution towards the signal [47]. Generally, the interaction position determines the shape of the induced charge signal (2.4). However, due to the similar weighting potential throughout the diode the dependence on the interaction position is rather weak [47].
The charge sensitive preamplifier (CSP) is the first unit in the processing chain converting the induced charges into voltage steps. It is within the cryostat, thus cooled together with the diode, to minimize noise. CONUS uses a so-called transistor reset preamplifier (TRP), the functionality of it is depicted in figure 2.11. The lowest voltage level is called baseline and events are collected as voltage steps on top of the previous event. The CSP can only collect a certain amount of charges (dynamic range) until a reset to the baseline occurs [81]. This reset is done via a transistor reset circuit. Commonly, resistive feedback amplifiers are used where the capacitor discharges after every voltage step and returns exponentially to the baseline. CONUS as a low threshold experiment is not using this amplifier due to additional noise (Johnson noise) [51]. Moreover, if the count rates are too high, the RC preamplifier constantly piles up events without having the time to fully restore the baseline. Hence, no events could be read out. For a TRP the number of resets would increase at high count rates, but it will not lock-up. The reset takes about $\mathcal{O}(10\,\mu s)$, but to avoid spurious events and to get back a stable baseline a TRP veto time window of 800 µs has been applied in RUN-5. The time where no events are recorded is called dead time. Besides the TRP veto, the muon veto time window (420 µs) and pile-up events, i.e. events following too quickly after the previous [51], contribute to the dead time.
Because the voltage step is directly proportional to the induced charge it also corresponds to the deposited energy of the interaction. The energy reconstruction happens in the DAQ where the energy of a single event is given as a channel[4] relative to the maximum number of channels (dynamic range) [51]. Later on, the channels need to be calibrated with signals of known energy. CONUS operates the Lynx DAQ [41] and since RUN-5 also the CAEN DAQ [40]. Because of the pulse shape extraction only the CAEN will be considered in this work, more details on the functionality of the Lynx can be found in [51]. The CAEN reconstructs the energy with a trapezoidal filter [87] where the height of the flat top is saved in ADC. The user interface to change settings, monitor the measurement and extract data is done via the CoMPASS software [88]. To record the timestamps of the TRP resets and the muon vetos the module V1725 from CAEN [89] is used for RUN-5. This enables to choose the veto window length freely and apply the cut offline with the chosen window.

[4] Abbreviated in the future with ADC (Analogue to Digital Converter channel).

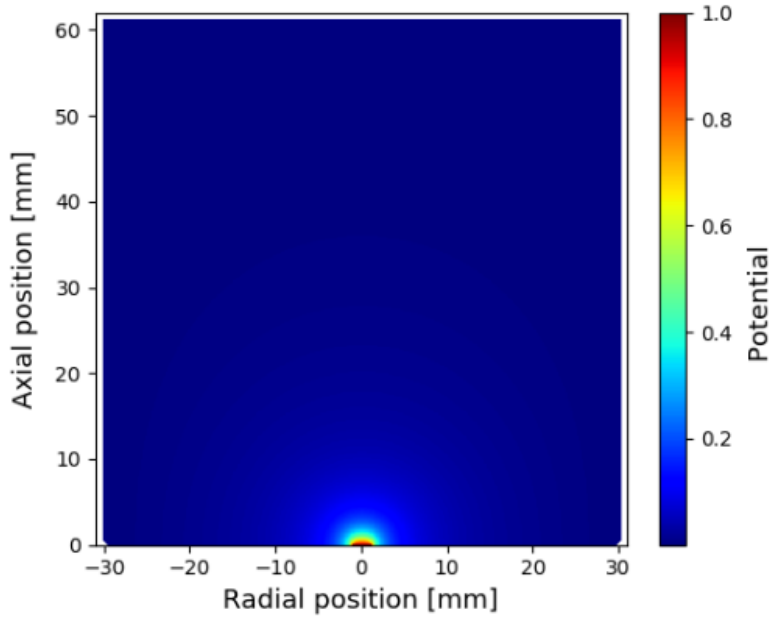

Figure 2.10. Simulated weighting potential of the C1 detector. Throughout the majority of the detector the potential is equally weak. Only towards the p+ contact it rises steeply. The plot is taken from [47].

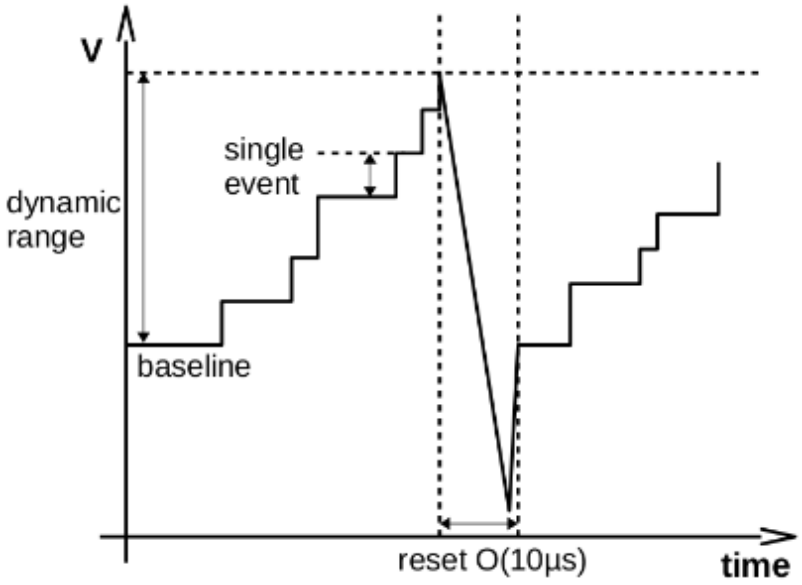

Figure 2.11. Functionality of a transistor reset preamplifier (TRP). Events are viewed as voltage steps on top of each other with the baseline as the lowest voltage level. When the dynamic range is reached the reset occurs bringing the voltage level back to the baseline. The figure is taken from [51].

Chapter 3

Basics of the PSD and risetime fit

In this chapter we introduce the various pulse shapes (section 3.1) and the different particles producing them (section 3.2). Consequently, we can justify the background suppression of the PSD when aiming to detect CEνNS. The τ-parameter from the risetime fit (section 3.3) will be used to discriminate background (slow pulses) from neutrino (normal pulses) events (section 3.4).

3.1. Pulse shapes

This section discusses the different pulse shapes the CAEN records. In figure 3.1 three mean pulses are plotted. To get a mean pulse we take the average of many events within one population in a certain energy range. In this case pulses within ca. 29-30 keV from a Thorium-228 (Th-228) measurement have been collected. Moreover, the C1 detector has been used which will also be the benchmark detector throughout this work.
The pulses can be split into three features they have in common. First, the baseline (red area) recorded before the pulse, the length depends on the pre-trigger time set in the CoMPASS settings. Second, the rise of the pulse (gray area) where the three pulses differ from one another. Last, the exponential decay (yellow area) due to the AC coupling of the DAQ which brings the pulses back to the baseline. This is an effect of the DAQ and, therefore, it is the same for all three pulses. The difference in the rise of the three pulses comes from the interaction position within the Ge detector. The blue and orange pulse are so-called 'normal pulses' because they interact within the active volume. Depending on the exact interaction position they exhibit a so-called pre-increase as can be seen by the blue pulse. Charges created by events happening further away from the p+ contact ($\gtrsim 20\,\mathrm{mm}$) experience a weak weighting potential, thus show some weak increase at the beginning (blue pulse), whereas, if the interaction occurs in the vicinity of the readout electrode the charges immediately experience a strong potential and rise strongly (orange pulse). Section 2.4.1 in [47] studies the effect of the pre-increase by simulating pulses at different positions using a one-dimensional weighting potential. Janine Hempfling from the CONUS collaboration is currently investigating the various pulse shapes by simulating them. Of course, transition between pulses with and without pre-increase is continuous because the weighting potential is continuous. However, due to the sharp peak of the weighting potential close to the p+ contact, a rather clear separation can be seen. The third pulse (green) is a so-called 'slow pulse' originating from an interaction within the transition layer. The drift field is weaker in the transition layer next to the Li-diffused dead layer [42, 90] and the holes need to diffuse out of it to reach the p+ contact. This

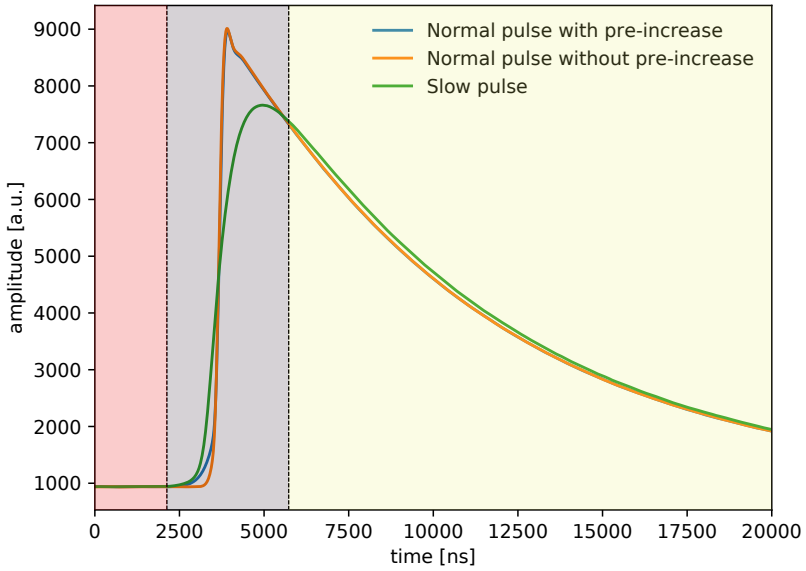

Figure 3.1. Three mean pulses ($29 \lesssim E \lesssim 30\,\mathrm{keV}$) from the different populations from a Th-228 measurement with C1 are plotted. The baseline (red area) and the exponential decay (yellow area) is similar for all three populations. In the gray area the rising edges of the pulses are different.

is the reason for a slower rise of the pulse and the origin of the name. Furthermore, the remaining Li-atoms in the transition layer lead to recombination centers and charge traps (see section 2.4.2). Hence, the charges are only partially collected at the readout electrode and the energy is not reconstructed correctly [42, 90].

The pulses shown in figure 3.1 are classified as single-site events (SSE), because only one energy deposition has occurred. There is also the possibility of multiple energy deposition within one event which results in so-called multi-site events (MSE) with a wrong energy reconstruction. MSE are more important at higher energies, e.g. interaction of photons via Compton scattering and pair production at the MeV scale. At the keV scale and below (ROI[1] of CEνNS) they occur very rarely. More details as well as the discrimination of SSE and MSE as a by-product of the PSD method can be found in section 4.7 in [47].

There are further classes of events where the energy reconstruction fails, e.g. saturation, pile-up events and events happening during the TRP reset[2]. Most of the events are either directly identified by the DAQ or cut by vetos (e.g. TRP reset time window). Overall, these 'unphysical' events need to be rejected in order to not distort the energy spectrum. The PSD offers another tool to identify and cut unphysical pulses.

[1] Abbreviation for region of interest.
[2] Examples for these events are shown in section 2.4.2 in [47].

3.2. Sources and interactions of the various particles

In this section various particles ($\nu, \gamma, \alpha, e^-, n$) and their interaction within the Ge crystal are examined.

Neutrinos

The goal of the experiment is to measure neutrinos interacting with Ge nuclei via CEνNS. Because of the very low cross section, they produce SSE and interact homogeneously throughout the entire detector. The active volume accounts for approximately $91 - 95\%$ depending on the detector [38], thus homogeneously interacting particles like neutrinos produce predominantly normal pulses.

Electromagnetic radiation

The intensity of electromagnetic radiation when traveling through matter decreases with the penetration depth x according to the Beer-Lambert law [81]

$$I(x) = I_0 e^{-\mu(E)x}, \tag{3.1}$$

where I_0 is the starting intensity, E the energy of the γ-ray and $\mu(E)$ the attenuation coefficient. For energies $\lesssim 100\,\text{keV}$ the photoelectric absorption is dominant, at higher energies ($\gtrsim$ few MeV) Compton scattering and eventually pair production become the dominant interactions as can be seen in figure 3.2. [81] provides a good overview over the three photon interactions and their energy deposition in Germanium.
Photons with energies of $\mathcal{O}(1\,\text{MeV})$ penetrate deep into the crystal, because the mean free path ($\lambda = \frac{1}{\mu}$) is several centimeter [51]. At photon energies of approximately 100 keV the mean free path becomes $\mathcal{O}(0.1\,\text{cm})$ [51] and at even lower energies it gets as low as $\mathcal{O}(1\,\text{mm})$, because of the massive increase of the attenuation coefficient towards lower energies in the photoelectric regime (see figure 3.2). For comparison the transition layer has a thickness of approximately 0.2 mm [38]. Hence, photons coming from outside the crystal interact within the transition layer as well as the active volume. Towards lower energies an increase in the fraction of photon interactions within the transition layer, i.e. slow pulses, is expected because of the decreasing mean free path. The main sources of external photons are muon induced secondary radiation inside the shield (e.g. Bremsstrahlung) and ^{210}Pb, although the daughter isotopes of ^{210}Pb decay mainly via β-decay, thus producing e^- [78]. Furthermore, cosmically activation of the material (e.g. Cu-parts close to the detector) can lead to electromagnetic radiation background. Also Ge can get cosmically activated via e.g. $^{70}\text{Ge} + n(\text{fast}) \rightarrow {}^{68}\text{Ge} + 3n$ [78]. The neutrons need energies of at least 20 MeV and ^{68}Ge has a half life of 278 d, thus it lives through a typical experimental measurement campaign [51]. ^{71}Ge ($T_{1/2} = 11.4$ d) on the contrary is created by thermal neutrons, thus in-situ activation is possible. The x-ray emission of the K-shell line at 10.37 keV is the most dominant line and clearly visible in the data [78]. Other lines are L-shell emissions

at approximately 1 keV and further emissions from the daughter nuclei, however they are by far not as dominant as the 10.37 keV line [51]. The events from cosmic activated Ge interact within the active volume due to their small energies and, consequently, small mean free paths ($\mathcal{O}(1\,\mathrm{mm})$). Because of this property the 10.37 keV line will serve as a reference for the characterisation of normal pulses (see section 4.1.4).

Electrons

As already mentioned in the decay chain of ^{210}Pb mostly β-decay occurs, i.e. electrons. Their mean free path is orders of magnitude smaller than for photons with the same energy. A 1 MeV e^- is stopped within millimeters and for an electron with a kinetic energy of 100 keV the mean free path is even a few orders of magnitude smaller. Hence, electrons coming from the outside deposit their energy in the first layers and produce, consequently, slow and normal pulses.

Neutrons

The neutron background of the CONUS experiment has to deal with ranges from 10^{-9} MeV up to $\mathcal{O}(10\,\mathrm{MeV})$ [80]. The main sources are muon induced neutrons in the shield and the concrete of the building as well as reactor correlated neutrons, whereas the latter has been shown to be negligible with respect to the expected neutrino signal [78]. Due to the broad energy range of neutrons various interaction channels need to be considered. For a more precise view on the neutron sources and their interactions within Ge we refer to [51, 78]. The mean free path of neutrons is large such that a nearly homogeneously interaction throughout the diode can be assumed and, therefore, they produce predominantly normal pulses.

α-particles

Because of their high ionization power, i.e. small mean free path, α-particles coming from the outside are shielded very easily and they do not penetrate the Cu cryostat. $^{219}\mathrm{Po} \rightarrow {}^{206}\mathrm{Pb} + \alpha$ with $T_{1/2} = 138.4\,\mathrm{d}$ and an energy of the α-particle of 5.2 MeV is the last decay in the ^{210}Pb chain [78]. In Ge they are absorbed within 20 µs [51]. Therefore, they are stopped inside the dead layer ($\mathcal{O}(1\,\mathrm{mm})$), but can penetrate the passivation layer ($\sim 100\,\mathrm{nm}$) [38]. If they reach the active volume, α-particles produce normal pulses.

In the decay chain of ^{210}Pb β- and Auger-electrons as well as γ-rays are produced. The e^- and the low energetic photons are very likely to interact in the outer layers of the diode and produce slow pulses. ^{210}Pb contamination comes from the lead layers of the shield, although it was made sure that the purity of the layers increases towards the crystal. Further ^{210}Pb contamination originates from lead based soldering wires within the cryostat [76, 78]. Apart from ^{210}Pb muon-induced x-rays and neutrons are the dominant background. At energies below $50\,\mathrm{keV_{ee}}$ the muon induced neutrons dominate over the muon induced electromagnetic bremsstrahlung. Thus, a PSD cut is expected to provide a

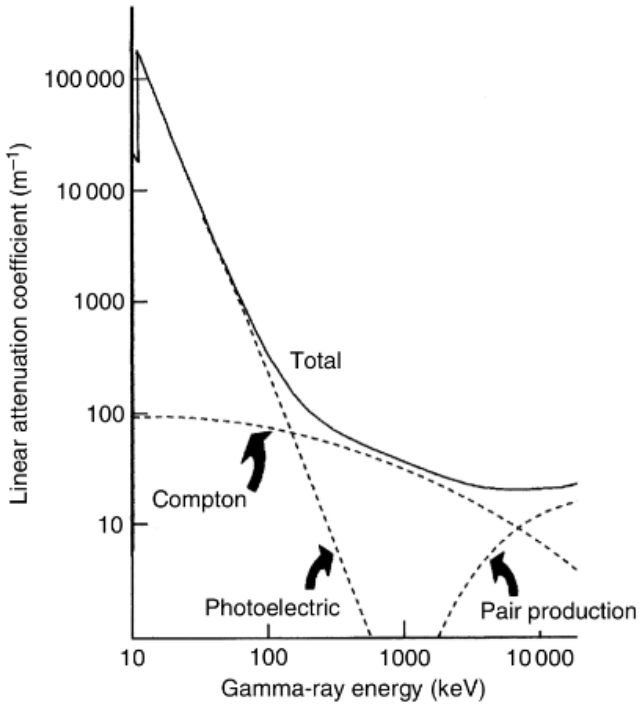

Figure 3.2. The total attenuation coefficient $\mu(E)$ of Ge for γ-rays is split into its components. At the keV scale the photoelectric absorption is dominant. The plot is taken from [81].

good discrimination for the ^{210}Pb background component, the neutrons, however, are not much affected.

Based on these physical considerations, we can conclude that PSD studies are promising in discriminating background components in form of e^- and photons because they are more likely to interact in the transition layer compared to neutrinos, which interact homogeneously throughout the diode. This results in a very small signal-to-background ratio in the transition layer compared to the active volume. [51, 78] provide more details about the different background sources for the CONUS experiment.

Having explained the possibility to use PSD as additional background suppression we will introduce the method to discriminate slow and normal pulses (so-called risetime fit) in the next section.

3.3. Risetime Fit

Jakob Henrichs investigated different discrimination methods in the third chapter of [47]. The A/E method (3.1.1 in [47]) used by the GERDA collaboration [46, 85] works to discriminate SSE and MSE but fails to discriminate slow and normal pulses at energies $\lesssim 4\,\text{keV}$. The integral ratio method (3.1.2 in [47]) would be suitable for discrimination of normal and slow pulses. However, in section 3.1.3 in [47] it is concluded that a fit to each individual pulse and using one fit parameter as the discrimination variable shows the best

discrimination power between slow and normal pulses.
A combination of a hyperbolic tangent and an exponential function will be used throughout this thesis to fit the individual pulses:

$$f(t) = A_0 \tanh\left(\frac{t - t_0}{\tau} + 1\right) e^{-\tau_c(t-t_0)} + P_0. \tag{3.2}$$

It is based on the function used by the TEXONO collaboration [42, 43, 45]. It has five free fit parameters: A_0 corresponds to the height of the pulse, thus it should reflect the energy; P_0 represents the baseline level; t_0 is proportional to the pre-trigger and τ_c characterizes the exponential decay and, therefore, the last two parameters depend on the DAQ; τ is the parameter of physical importance because it characterizes the rise time of the pulse. Hence, the risetime τ will be the parameter to discriminate between normal and slow pulses. In section 3.2.4 in [47] the different fit parameter are discussed in great detail. Besides (3.2) other functions have been investigated in section 3.2.1 in [47], the so-called error, lognormal and skew function. The skew function has been shown to perform the best fit, i.e. the best discrimination power of the risetime. However, considering practical criteria as the runtime of the fit and the percentage of failed fits it has been concluded to use (3.2) for the PSD.
In the following further improvements on the fit performance are discussed based on [47]:
The influence of smoothing (section 3.2.2 in [47]): A low pass filter to cut the noise (higher frequencies than the pulse) has been applied. However, the high frequencies are also responsible for "sharp edges", thus filtering them increases the risetime and weakens the discrimination power. Therefore, smoothing has not been further used.
Fixing the τ_c-parameter (section 3.2.3 in [47]): The τ_c-parameter resembles the exponential decay of the pulse, which depends on the AC coupling of the CAEN. Therefore, it should be the same for every pulse (slow or normal) at every energy. It has been shown that fixing the parameter at low energies (below 8000 ADC) improves the fit performance, i.e. it helps the fit to converge and fit the pulse accurately. A Gaussian fit to the τ_c-distribution of high energetic events $E \approx 15 - 32$ keV has been used to find the fixed τ_c-parameter for each detector. The fixing of this parameter for events below 8000 ADC has been implemented in the analysis chain of the data.
Different window sizes (appendix A.2 in [47]): Shortening the pre-trigger and the exponential decay could improve the fit result on the rise of the pulse, the crucial part. The first has been discarded because it lowers the stability of the baseline (P_0-parameter). The latter is in principle possible, but the influence on the fit is minor. Hence, the recording time of the CAEN stays at 20000 ns and the full pulse is fitted.
Further cuts based on the fit parameters have been investigated in the end of section 3.2.4 in [47]. So-called quality cuts to get rid of unphysical events, e.g. artifacts. By rejecting events with extremely high energies ($A_0 > 4700$) and only keeping events with expected exponential decays ($6 \times 10^{-5}\,\mathrm{ns}^{-1} < \tau_c < 16 \times 10^{-5}\,\mathrm{ns}^{-1}$), saturation events that have not been flagged by the DAQ and pile-up events can be cut. Further events can be rejected by cutting the pulses where the fit failed, this will be separately examined in section 5.4.

3.4. Discrimination based on the τ-parameter

The goal is to find a cut value τ_{cut} which keeps most of the normal pulses and rejects many slow pulses. More precisely, we want to define τ_{cut} together with the so-called cut efficiencies, which describe the percentage of neutrino events surviving the PSD-cut [47], at various energies. The explicit statement about neutrino events instead of normal pulses in the definition of the cut efficiency will be clarified in section 4.1.4.
In figure 3.3 the risetime is plotted against the energy for events from Th-228 measurements. More precisely, the decadic logarithm of the risetime ($\log_{10}(\tau)$) which will be used throughout this thesis[3]. In section 4.3 in [47] the ratio of slow to normal pulses from measurements is compared to MC simulations and estimations based on (3.1). It has been validated that the two visible populations at higher and lower risetimes in figure 3.3 indeed come from slow and normal pules, respectively.
At high energies ($\gtrsim 5\,\text{keV}$) the band of normal ($RT \approx 2.15$) and slow pulses ($RT \approx 2.8$) can be clearly separated. By eye one could draw a line at ($RT \approx 2.4$) which keeps the majority of normal pulses while cutting many slow pulses. However, while approaching lower energies the populations start to spread due to the influence of the noise. Especially within our ROI for CEνNS (0.2 - 1 keV) the two bands mix and a distinct allocation of events towards normal or slow population is not possible anymore (see the enlarged figure 3.3b). Already at higher energies identifying events between the bands as slow or normal pulses is quite challenging. However, it results only in minor uncertainties as events in between the populations are relatively rare in comparison to events within. Furthermore, below 15 keV there is no external source which can be used to study the risetime distribution as the γ-rays do not have enough energy anymore to penetrate the shield [51].
To get a reliable description of physical pulses, nevertheless, we use an arbitrary function generator, the Pulser AFG3252 by Tektronix [91]. Therewith we can simulate and study the risetime distributions of the normal and slow pulse population individually. Hence, a well-founded description of the normal pulse population from the pulser can be used directly to find the cut values. Furthermore, with the help of pulser measurements the influence of the noise on the risetime distribution can be studied more thoroughly. In the next chapter the procedure to simulate trustworthy physical pulses with the pulser is described.

[3] The $\log_{10}(\tau)$ will be called 'RT' and the unit $\log_{10}(\text{ns})$ will be omitted.

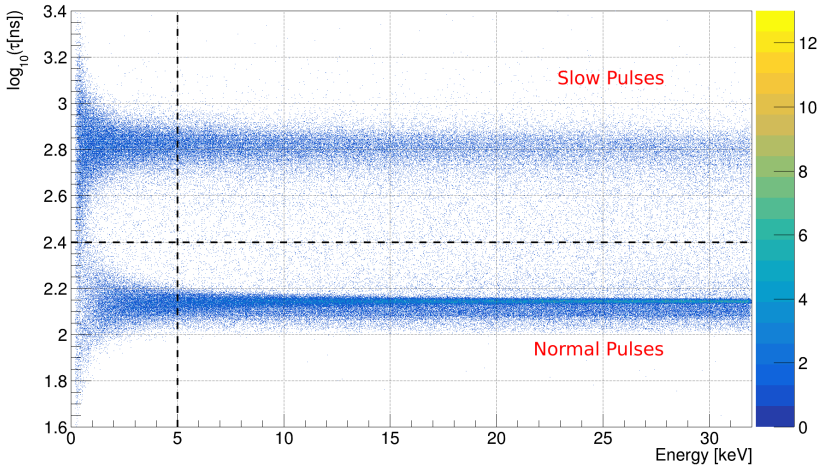

(a) Energy range from 0 - 32 keV.

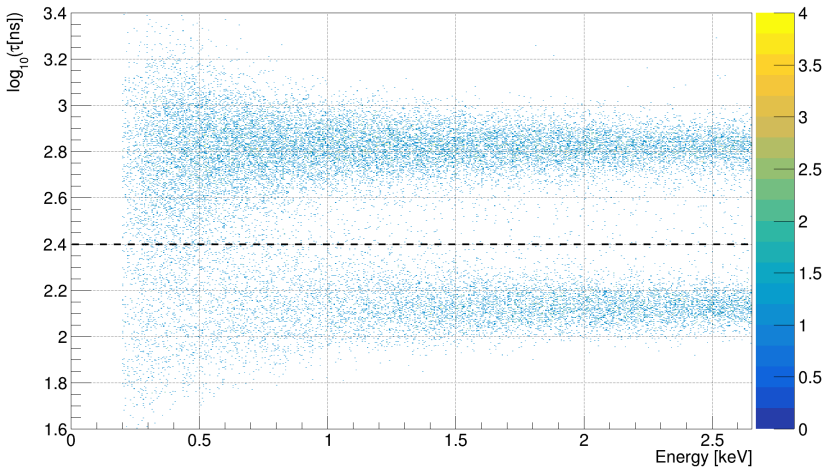

(b) Energy range from 0 - 2.6 keV.

Figure 3.3. Events with their associated decadic logarithm of the risetime (y-axis) and energy (x-axis) from multiple Th-228 measurements with C1 are plotted. At higher energies ($\gtrsim 5\,\mathrm{keV}$) the normal and slow pulse population are clearly separated by an exemplary line at $RT = 2.4$ as to be seen in (a). At lower energies the populations start to intermingle better visible in the enlarged figure (b). The colored bar at the right side represents the number of events per bin.

Chapter 4

Tools for the PSD analysis

In the previous conducted work by Jakob Henrichs [47] the PSD-cut in the region of interest had large systematic uncertainties. They arose from mainly two reasons. First, the description of the physical pulses by the pulser was imperfect. Second, the influence of the noise in the region of interest leading to a distortion of the τ-distribution was not sufficient modeled. In this chapter tools to improve the first and second aspect are introduced in section 4.1 and 4.2, respectively, to lower the systematic uncertainties on the PSD-cut.

4.1. Generating physical pulses

4.1.1. Setup and challenges of the pulser

The pulser is connected via the input 'Test' to the electronics chain of the signal directly after the diode, as can be seen in figure 4.1. Therefore, the signal does not go through the crystal, but through the preamplifier and DAQ chain. This alters the input signal due to the so-called electronic response of the devices (section 4.1.2). Hence, the input pulses for the pulser need to be adapted to reproduce the physical signals coming from the diode, whose shape is unknown since the signal is always measured at the output of the DAQ chain (section 4.1.3). The blue pulse in figure 4.2a is a mean pulse of the normal population from a Th-228 measurement done with C5, i.e. a real measured output pulse from the detector after the DAQ chain. Using it without any adaptions as input pulse for the pulser, the pulse recorded by the CAEN after going through the electronics can be seen as the black pulse in figure 4.2a.
Pulses coming from the diode are expected to be flat at the top and the exponential decay is due to the AC coupling of the DAQ. Therefore, the exponential decay of the input pulse is damped once more resulting in the stronger decrease of the output pulse (black) compared to the real measured pulse (blue) seen in figure 4.2a. This effect of the DAQ can be fixed by using a flat top[1] for the input pulses which results in an output pulse seen in figure 4.2b. One can see that the effect of the 'double exponential decay' has vanished. However, the electronic response has also an effect on the shape of the pulse before the decay, i.e. the risetime. Hence, this simple adaption on the pulse is not sufficient in order to resemble the physical pulses coming from the detector.

[1] A pulse which stays at the maximum value without exponentially decreasing.

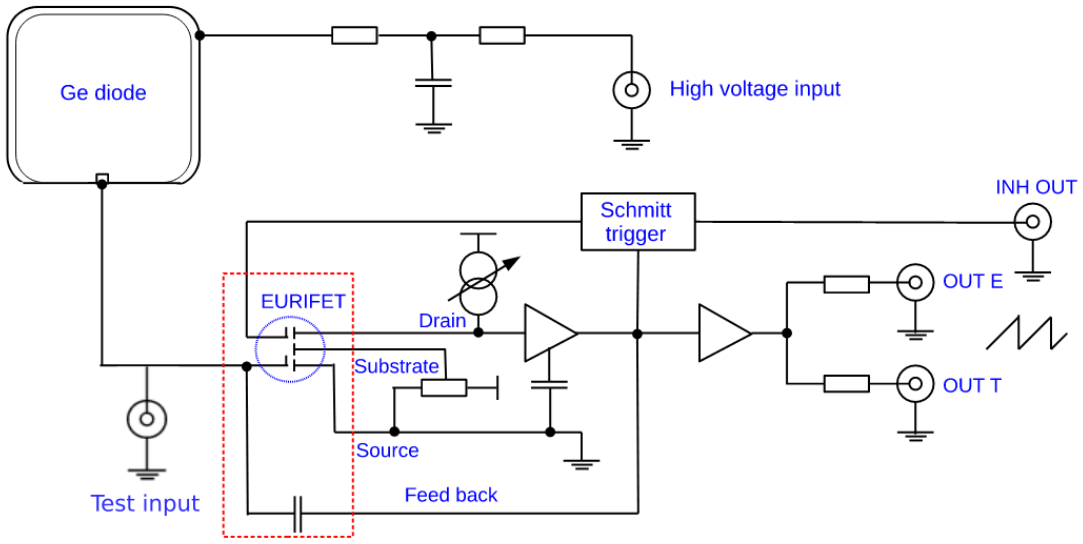

Figure 4.1. Simplified representation of the electronics of the CONUS detectors. The 'Test' input is in between the Ge diode and the preamplifier. The raw pulse traces are connected to the DAQ via the output 'OUT E'. The plot is taken from [38] with the small adaption of the 'Test' input.

In [47] pulser measurements have been conducted with the flat top input pulses, i.e. taking only the exponential decay of the electronic response into account. Therefore, the output pulses were not expected to resemble physical pulses, but were rather used to find a model function of the risetime distributions at different energies. The parameters of the models were estimated from Th-228 measurements and reactor-ON data. The calculated cut efficiencies based on the models are very accurate for higher energies, however, below approximately 7-8 keV the uncertainties propagated from the parameter estimation get large. Thus, if the pulser measurements describe physical pulses they can be directly used to calculate the cut efficiencies. This procedure is expected to lower the uncertainties. Therefore, we will characterize the electronic response in the next section in order to modify the input pulses to resemble the physical pulses more accurately.

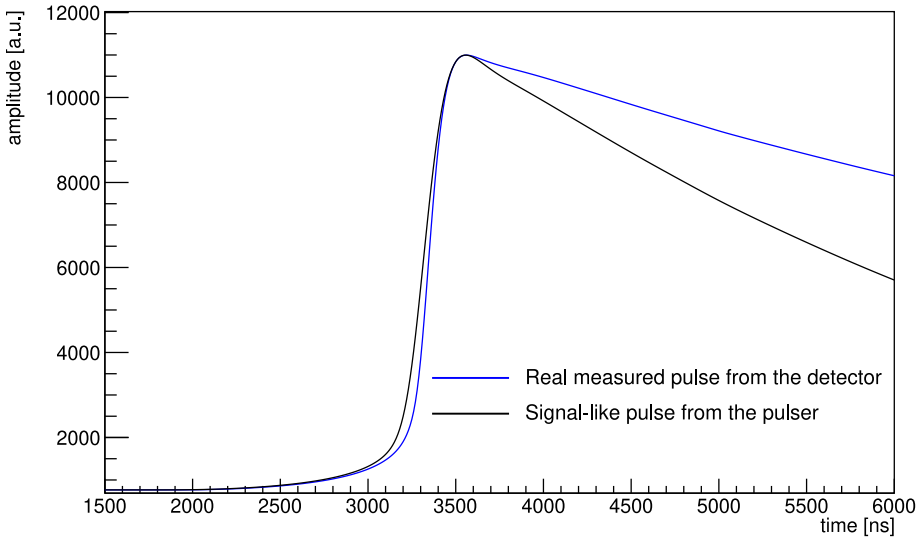

(a) Using the real measured pulse from the detector without any adaptions as input pulse for the pulser. The resulting pulse is twofold exponentially damped.

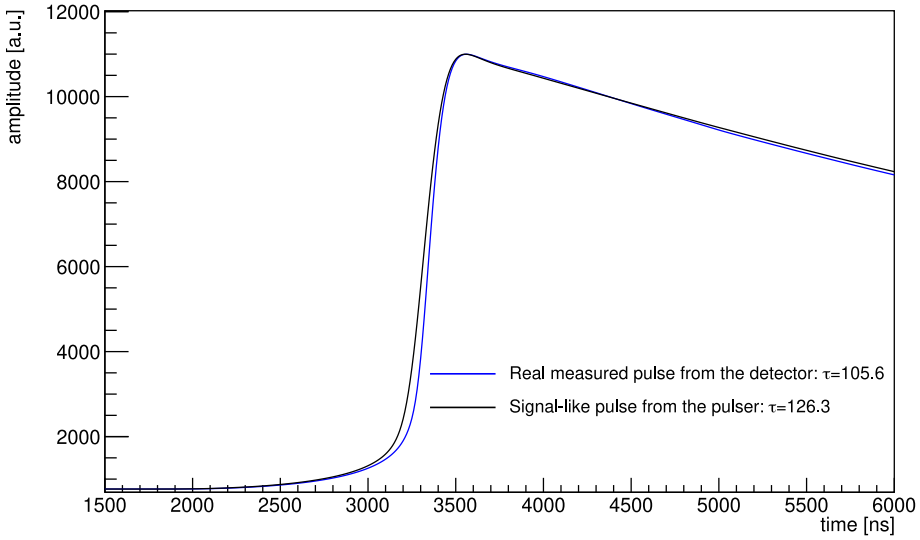

(b) Using the real measured pulse from the detector with a flat top as input pulse for the pulser. The exponential decays of the two output pulses match, but the rising edges still look different.

Figure 4.2. Influence of the electronic response. The blue pulse is a real measured output pulse from the detector. The black pulses are output pulses from pulser measurement using different input pulses.

4.1.2. Electronic response determination

In this section we investigate the influence of the electronic response onto the input signal from the pulser, i.e. how the electronics transform the input signal into the output signal. We are assuming that the electronics is a highly linear system which has been validated with various pulser and radioactive sources measurements [38]. Furthermore, the electronics is a time-invariant system since the delaying of the input signal simply delays the output signal by the same amount of time. Thus, we are dealing with a linear and time-invariant system, a so-called LTI system. The following formula and information in this section about the electronic response of LTI systems has been taken from chapter 2 in [92].
A signal x can be decomposed into a superposition of unit-samples δ

$$x[n] = \sum_{k=-\infty}^{\infty} x[k]\delta[n-k]. \tag{4.1}$$

A unit-sample $\delta[n-k]$ is a signal which is zero everywhere except for one point $n = k$. The unit-sample response $h[n]$ is defined as the output signal when using the unit-sample $\delta[n]$ as input ($\delta[n] \rightarrow$ LTI system $\rightarrow h[n]$). Because of the linearity and the time-invariance the output signal y directly follows from (4.1)

$$y[n] = \sum_{k=-\infty}^{\infty} x[k]h[n-k] = (x * h)[n]. \tag{4.2}$$

The asterisk in the latter expression denotes the convolution of the input x with the unit-sample response h. Thus, by knowing the unit-sample response the output signal can be calculated for every input signal.
The above was done for a discrete system and it equally holds for a continuous system

$$y(t) = \int_{-\infty}^{\infty} x(\tau)h(t-\tau)d\tau = (x * h)(t). \tag{4.3}$$

Using a box signal as the input signal, mathematically speaking the Heaviside step function θ, we get from (4.3)

$$y(t) = (\theta * h)(t) = \int_{-\infty}^{\infty} \theta(\tau)h(t-\tau)d\tau = \int_{-\infty}^{t} h(\tau)d\tau, \tag{4.4}$$

which yields by differentiation

$$h(t) = \frac{d}{dt}y(t). \tag{4.5}$$

For discrete signals it would result in the discrete time derivative, but the principle procedure is the same. Hence, when using a box signal as the input pulse, the derivative of the output signal is the unit-sample response[2]. For practical reasons the way of measuring $h(t)$ through (4.4) and (4.5) was introduced since the generation of a unit-sample δ is

[2] unit-sample response is called impulse response for continuous systems, they will be used synonymously.

practically speaking impossible. Hence, we decided to measure the response to an input box signal instead of a unit-sample allowing to calculate the impulse response via the derivative of the output pulse.
The result can be seen in figure 4.3 for all four detectors in KBR. The impulse responses look quite different for each detector, because of differences in the preamplifier and in the four DAQ channel settings. As a result we have to treat each detector individually.
The linearity of the impulse response has been cross-checked by applying box signals with various energies (heights). As expected from a linear behavior the impulse responses scale in the same manner and do not change in shape. The measured output pulse when using a flat top as input pulse is shown in figure 4.2b in black. The expected one by calculation via (4.2) is depicted in orange in 4.5a. Just by a rough comparison by eye they look quite similar which validates (4.2) and the calculated impulse responses $h(t)$.
Knowing the impulse responses of every detector we now want to obtain the input pulses such that the pulses, after going through the electronics, (output) coincide with physical pulses coming from the detector. Hence, we have to solve (4.3) for $x(t)$ while knowing $y(t)$ and $h(t)$. The output pulse $y(t)$ is obtained by taking the mean of many pulses at higher energies to minimize the effect of noise. Typically, a Th-228 measurement is used to enhance the statistics. In the next section various attempts to calculate the input pulse $x(t)$ will be presented.

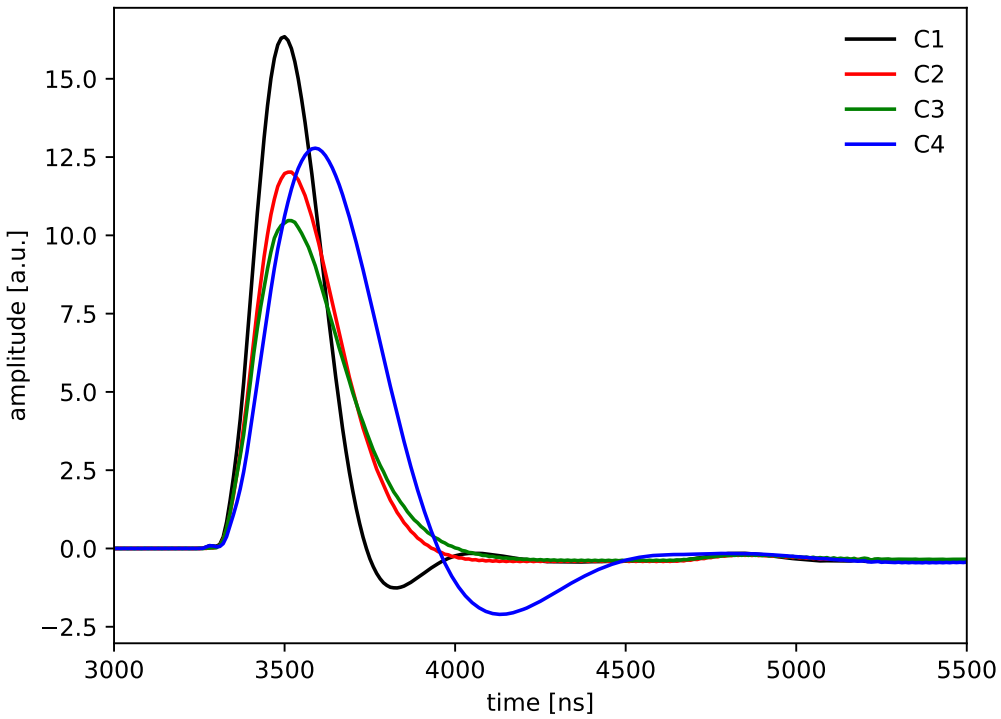

Figure 4.3. The impulse responses of all four detectors. Because of their large variations each detector has to be considered individually.

4.1.3. Input pulse determination

The goal in this section is to calculate the modified input pulses to account for the electronic response. The impulse response is known and the physical pulses are obtained by building the mean of many events within one population. The population of interest is the normal pulse population since the neutrino events are expected there. In the following three methods to calculate the input pulses are described.

Deconvolution via Fourier transform

Mathematically speaking we need to rearrange (4.3) for $x(t)$. For that the convolution theorem comes in handy

$$\mathcal{F}\{x * h\} = \mathcal{F}\{x\} \cdot \mathcal{F}\{h\}, \tag{4.6}$$

where $\mathcal{F}$ denotes the Fourier transform [92]. To put the equation in words, the convolution in time-domain (real space) becomes a normal multiplication in frequency domain (Fourier space). The Fourier transform is defined through

$$\mathcal{F}\{x\}(\xi) \equiv \hat{x}(\xi) = \frac{1}{\sqrt{2\pi}} \int_{-\infty}^{\infty} x(t) e^{-i2\pi\xi t} dt, \ \forall \xi \in \mathbb{R}, \tag{4.7}$$

for an integrable function $x : \mathbb{R} \to \mathbb{C}$ [92]. The inverse Fourier transform reads

$$\mathcal{F}^{-1}\{\hat{x}(\xi)\}(t) = x(t) = \frac{1}{\sqrt{2\pi}} \int_{-\infty}^{\infty} \hat{x}(\xi) e^{+i2\pi t\xi} d\xi, \ \forall x \in \mathbb{R} \text{ [92]}. \tag{4.8}$$

By applying the inverse Fourier transform to solve (4.3), i.e. going back to real space, we achieve

$$x(t) = \mathcal{F}^{-1}\left\{\frac{\hat{y}}{\hat{h}}\right\}(t). \tag{4.9}$$

Hence, the input pulse $x(t)$ can be calculated via the Fourier transforms of the output function $y(t)$ and the impulse response $h(t)$ [92]. By simply swapping the integral to a sum in (4.7) the discrete Fourier transform is obtained and it can be used for discrete signals. However, solving (4.9) is very challenging in our case. The biggest problem is the division by $\hat{h} = \mathcal{F}\{h\}$ which can get zero or close to zero. Hence, minor errors due to e.g. noise result in large perturbations making the result unstable [92–94]. Furthermore, an expected input pulse convolved with the impulse response has the shape seen in figure 4.4. The output pulse we get from the DAQ, however, does not show the negative part. Moreover, the negative part is not simply computable from the positive (e.g. through mirroring), it is rather complicated as it is a result from the convolution. Because of these problems we were not able to calculate the input pulse using the Fourier transform and the convolution theorem and we had to think of other ways.

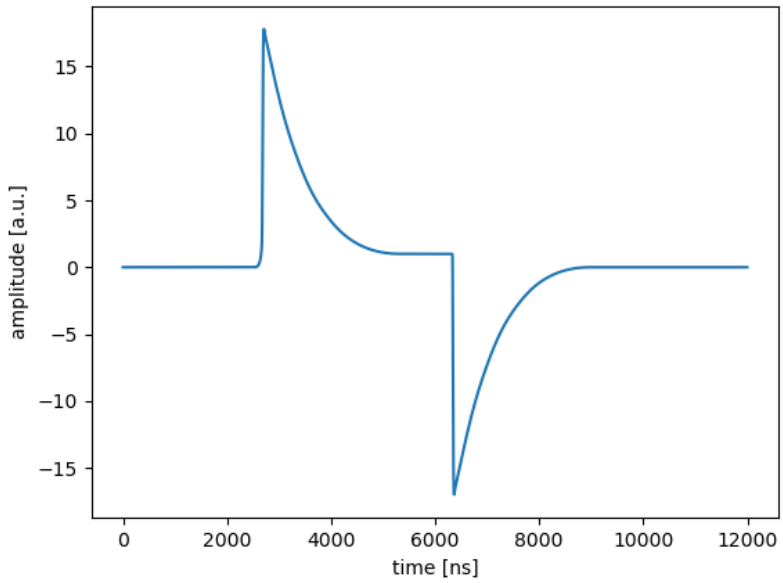

Figure 4.4. An expected input pulse convolved with the impulse response. The negative behavior of the pulse is not seen by real measured output pulses. In order to calculate input pulses via this method, the used output pulses must look similar.

Iteratively

Since we are dealing with discrete signals we can also calculate $x[n]$ iteratively via (4.2), in the following way:

$$\begin{aligned} y[0] &= x[0]h[0] && \Rightarrow x[0] = \frac{y[0]}{h[0]} \\ y[1] &= x[0]h[1] + x[1]h[0] && \Rightarrow x[1] = \frac{y[1] - x[0]h[1]}{h[0]} \\ &... \end{aligned} \tag{4.10}$$

The denominator $h[0]$ is typically close to zero and amplifies small errors in the measured output signal $y[n]$, e.g. due to noise. As we continue to use the previous calculated $x[n]$ the errors get enhanced until it gets unstable. Hence, we run once again into numerical problems. To avoid those, the so-called iterative distortion method has been developed.

Iterative distortion method

The functionality of this method will be explained by reference to figure 4.5. First, a real measured pulse $y(t)$ (blue) with a flat top as already described in the beginning of the chapter is taken. The following pulses are all calculated through convolution with the impulse response $h(t)$.

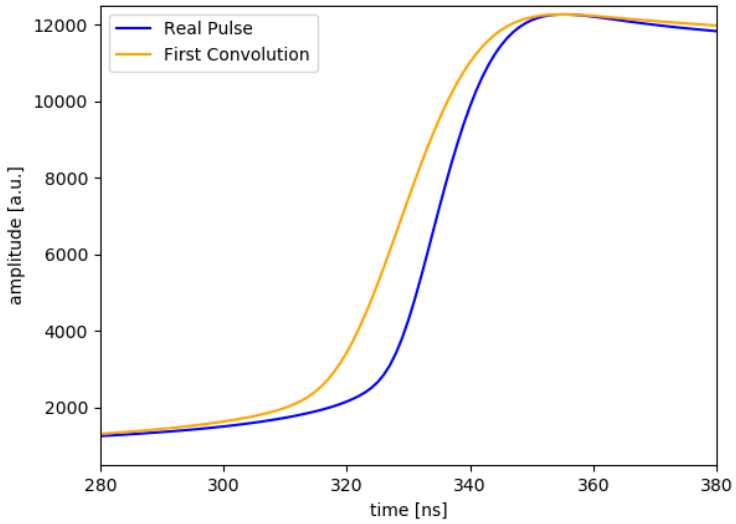

(a) The convolution of the real measured output pulse (blue) (with a flat top) with the impulse response results in the orange pulse which is not matching the blue pulse as expected.

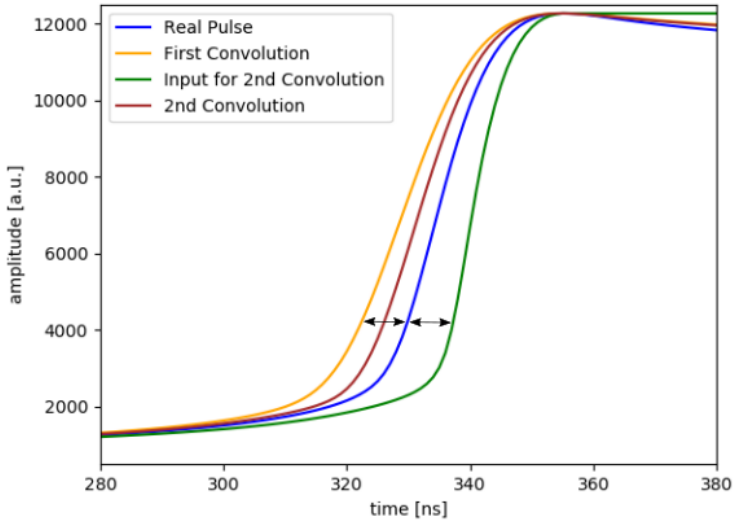

(b) The modified input pulse (green) is shifted point by point by the horizontal distance between the previous convolution (orange) and the real pulse (blue).The convolution of the green pulse yields the brown pulse which is a closer match to the blue pulse.

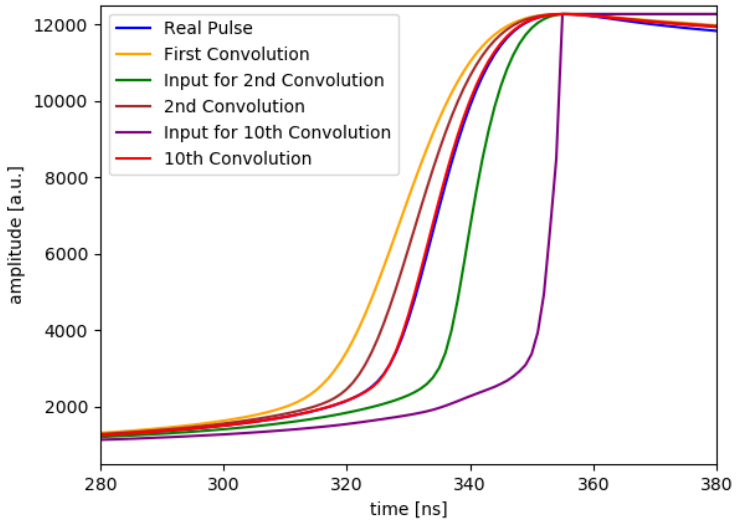

(c) The previous steps are iterated for ten times. The modified input pulse (purple) yields the theoretical output pulse (red) which is a close math to the real output pulse.

Figure 4.5. Working principle of the iterative distortion method. The goal is to match the real measured output pulse (blue) with a theoretical output pulse obtained by the convolution of the modified input pulse with the impulse response.

The first convolution of the real measured pulse (blue) and the impulse response results in the orange pulse seen in figure 4.5a. Eventually, an input pulse is desired where the output pulse (orange) coincides with the real measured output pulse (blue). Therefore, we modify the input pulse, which has so far been the flat top real pulse, by shifting it point by point. The distance of the shift corresponds to the horizontal distance between the previous input pulse (blue) and the convolved pulse (orange) but into the opposite direction. The newly modified input pulse can be seen in figure 4.5b as the green pulse. The steps so far are repeated. Thus, the modified input pulse (green) gets convolved with the impulse response to get the brown output pulse in figure 4.5b. The green pulse is shifted further to the right by the distance between the brown and the blue pulse now. As the output pulses approach the desired real pulse (blue) the shifting of the input pulses becomes less. In the case of figure 4.5c the iteration has been ceased after ten times. Hence, doing a pulser measurement with the modified input pulse (purple) an output pulse (red) similar to the real measured pulse is expected.

For the entire method the input pulses have only been modified for the rising and not the decaying region of the pulse, meaning that the maxima of all the pulses are at the same position and the input pulses stay at the maximum (flat top pulses). Neither further investigation on the decay of the pulse (τ_c) nor the translation of the maximum (T_0) is of great interest because the discriminating parameter is the risetime τ.

In figure 4.6 the various output pulses are plotted and their corresponding risetimes are obtained by fitting the pulses. The red and the green pulse correspond to the measured and theoretically expected output pulse, respectively, when using the modified input pulse. The blue pulse is the desired output pulse of a real pulse coming from the detector. For comparison the output pulse for the initial flat top input pulse from figure 4.2b is shown again in black. It is clearly visible that the modifications lowered the risetime considerably. A small discrepancy between the theoretically expected (green) and the measured pulse (red) of circa 3 ns is still present, but compared to circa 21 ns from the initial flat top pulse it is a great improvement.

To sum it up, with the modified input pulses we achieve a better match between the output pulse from the pulser and the real pulse coming from the detector which manifests itself in a reduction of the risetime discrepancy from ~ 21 ns to ~ 3 ns. In the next section it will be further examined how well the normal population from the pulser reproduces the real data. Mainly, events from the 10.37 keV line will be used as a reference to normal pulses from the detector.

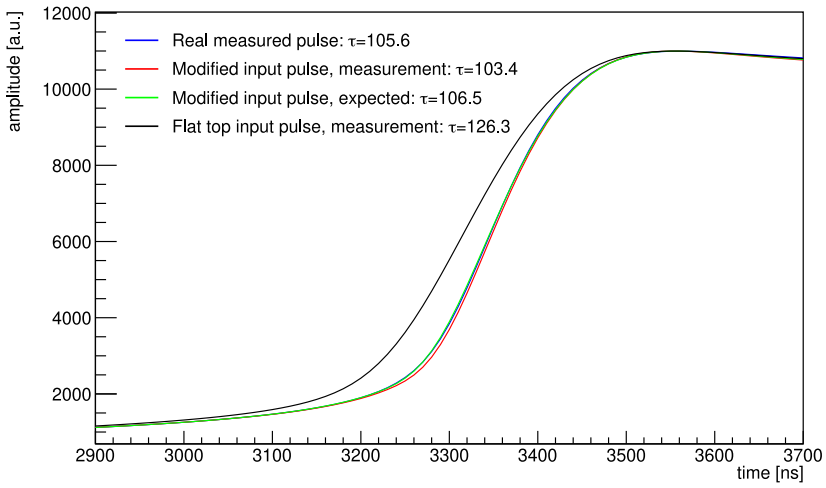

Figure 4.6. Comparison of various output pulses and their risetimes. The blue pulse corresponds as usual to the real measured output pulse from the detector. The black and the red pulse are from pulser measurements with different input pulses; The black is just modified by a flat top, the red by the iterative distortion method. The green pulse is the expected pulse using the input pulse from the iterative distortion method.

4.1.4. Validation through physical signals

We need to validate that the risetime distribution from a measurement with the pulse generator matches the risetime distribution of the physical data. In order to calculate a cut efficiency, i.e. the number of neutrino events surviving the PSD-cut, it is necessary to reproduce the risetime distribution of the normal population. At 10.37 keV is the K-shell line from the Ge isotopes ^{68}Ge and ^{71}Ge, which consists of normal pulses (see section 3.2). The events from the 10.37 keV-line are generated homogeneously throughout the active volume [38] as it is assumed for neutrino events. Because not all interactions within the active volume are distributed homogeneously, the cut efficiency is defined as neutrino events, which are homogeneously generated, surviving the PSD-cut rather than normal pulses surviving the PSD-cut. Hence, the 10.37 keV line is a perfect candidate for validation of the risetime distribution of the normal population.
Besides the 10.37 keV line the 1.3 keV line from L-shell emissions of Ge contains likewise homogeneously distributed normal events. It is also visible in the spectrum, although it is much weaker and more dominated by background than the 10.37 keV-line. At the end of this section a pulser measurement will be compared to a τ-distribution of events from the 1.3 keV line.
At energies below a few 10 keVs electromagnetic radiation of an external source can no more efficiently reach the active volume [38]. Therefore, any calibration of the populations with an outside source is not possible. In addition, they would not generate solely normal pulses but also slow pulses as they penetrate the transition layer when coming from outside the diode.

For these reasons the risetime distribution of the 10.37 keV-line is used to validate and calibrate the pulser measurements. The latter means that the input pulses for the pulser are created from the previously described method (section 4.1.3) and then slightly adjusted, by varying the number of iterations in the iterative distortion method, such that the mean of the risetime distribution of the output pulses matches the calibration τ-distribution form the 10.37 keV-line. This procedure can be seen exemplary in figure 4.7 where the risetime distributions of various input pulses is plotted. The mean μ and the standard deviation σ is obtained by fitting a Gaussian to the distribution. We only have an influence on the peak position (μ) of the distribution via adapting the risetime of the input pulses. The broadening of the distribution (σ) is an effect of the noise, and therefore, depends on the energy of the pulser measurement.
As expected from the relative contribution of the noise growing when the energy decreases, the distributions are becoming broader for low energies. This effect is illustrated by the red distribution in figure 4.7 for $E = 8.5$ keV. The green and the black distribution are measured at the same energy ($E = 10.4$ keV) and, therefore, the width (σ) is the same and only the mean (μ) is altered due to different input pulses.
In order to be able to measure low energies an attenuator needs to be added after the pulser. Although attenuators should not distort the pulse shape, it has been observed that the attenuator strength influences the risetime. An explanation would be that the damping is frequency dependent, resulting in a different damping of the rising edge (higher frequencies) compared to the rest. No further investigation has been carried out, we just optimized the pulses using a 40dB attenuator.

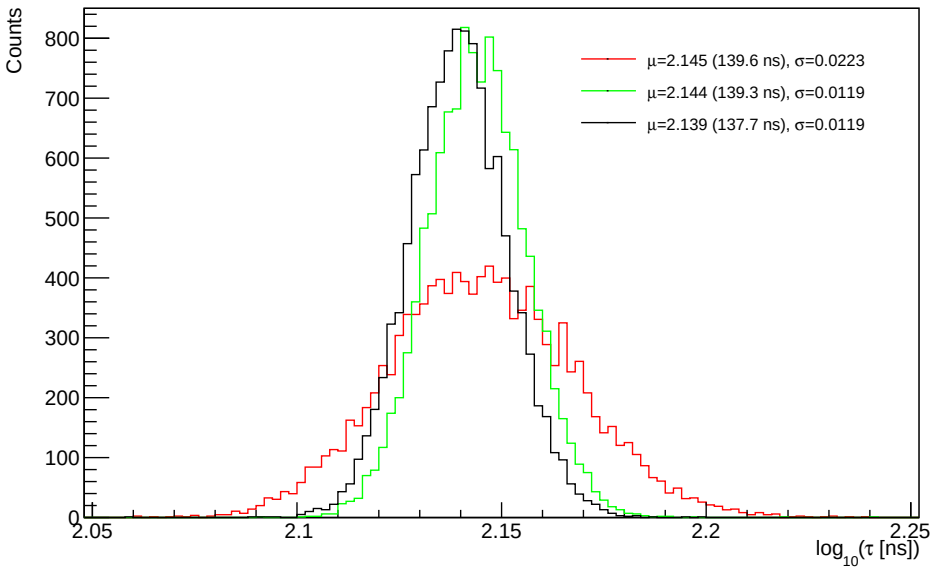

Figure 4.7. Risetime distribution from pulser measurements at circa 10.4 keV (black and green) and 8.5 keV (red). The mean μ of the distributions can be altered with different input pulses. The width ($\propto \sigma$) is energy dependent.

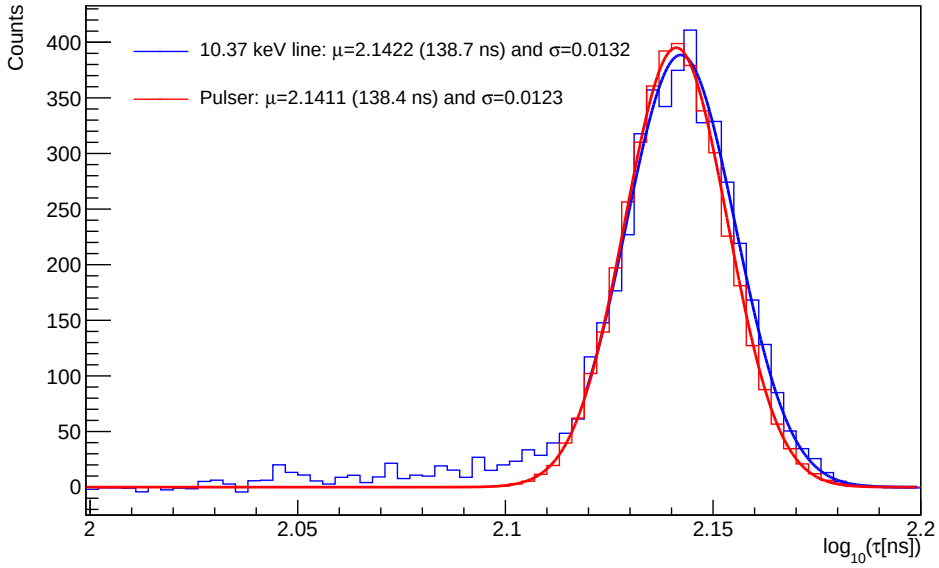

Figure 4.8. Comparison of the risetime distributions obtained from a pulser measurement and from the 10.37 keV line. The mean and the standard deviation parameter are obtained from a Gaussian fit. In the 10.37 keV line distribution the lower normal population is visible but it is not considered for the Gaussian fit. Background events in the 10.37 keV line have been subtracted. The counts on the y-axis corresponds to the events within the 10.37 keV line, the pulser measurement has been scaled accordingly. For the 10.37 keV line the available ON and OFF data from RUN-5 (about 9 months) have been taken.

The mean from a Gaussian fit is used to find the distribution which matches the best with the 10.37 keV distribution, which can be seen in figure 4.8. For the 10.37 keV distribution we considered events within the energy range $10.17 < E < 10.57$ keV. To get rid of 'background' events, meaning in this case events which do not belong to the decay of the Ge isotopes, half of the background above ($10.57 < E < 10.97$ keV) and below the line ($9.77 < E < 10.17$ keV) has been subtracted. Due to this subtraction there are no slow pulses visible in the resulting distribution[3]. Without subtracting the background there would be over 80 slow pulses, i.e. events with $RT > 2.2$. This validates the assumption that the Ge isotopes produce only normal pulses. Furthermore, one notices in figure 4.8 that within the 10.37 keV-line are more events at lower risetimes compared to the pulser distribution. We expect a contribution of a normal lower population within the 10.37 keV line due to interactions close to the readout electrode, whereas the distribution from the pulser measurement only displays pulses from the normal higher population by construction.
The input pulse used to generate the red distribution in figure 4.8 matches the 10.37 keV distribution best with an μ and σ agreement of 0.05 % and 7 %, respectively. This validates the method and the discrepancies in μ and σ will be used to estimate systematic uncertainties in section 5.3.1. With this input pulse the PSD-scan will be performed over the entire energy range, see chapter 5.

[3]Because of the x-axis range the lack of slow pulses can not be seen in figure 4.8.

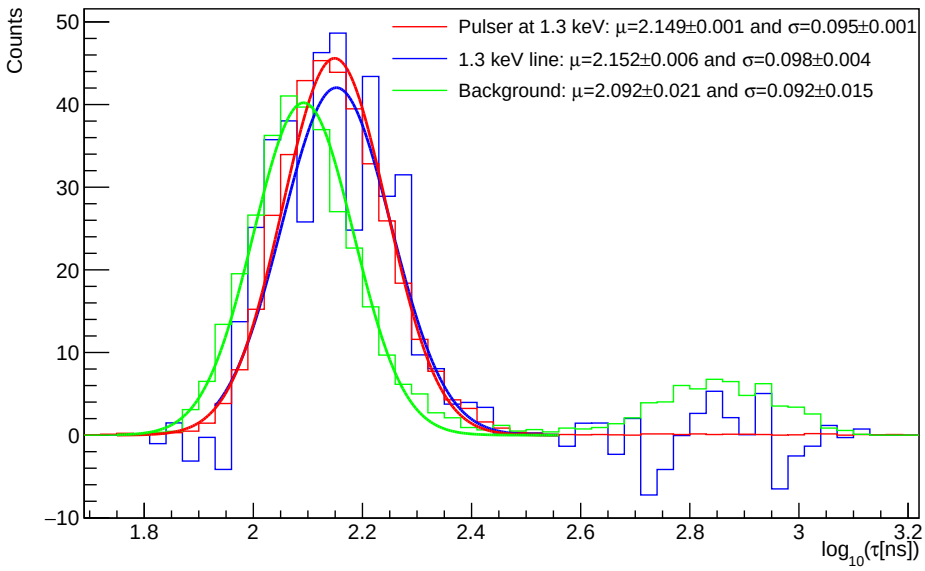

Figure 4.9. The distribution from the 1.3 keV line (blue) is compared to the pulser measurement (red) at the same energy. The background from events around the 1.3 keV line has been subtracted from the blue distribution and is plotted in green. The mean and the standard deviation parameter are obtained from a Gaussian fit. The counts on the y-axis corresponds to the events within the 1.3 keV line, the pulser measurement and the background has been scaled accordingly. For the 1.3 keV line the available ON and OFF data from RUN-5 (about 9 months) have been taken.

Comparison to the 1.3 keV linie

The L-shell X-ray lines of ^{68}Ge, ^{71}Ge, ^{68}Ga, ^{65}Zn are observed as a single peak at 1.3 keV [51]. The emission probability is around one order of magnitude smaller than the K-shell emission (10.37 keV line for ^{68}Ge, ^{71}Ge) and, therefore, weaker visible in the spectrum [78]. ^{68}Ga and ^{65}Zn are decay products of Ge isotopes [51]. Hence, the 1.3 keV line produces alike the 10.37 keV line homogeneously distributed normal pulses.
In figure 4.9 the risetime distribution of a pulser measurement at 1.3 keV (red) is compared to the τ-distribution of events from the 1.3 keV line ($1.22 < E < 1.37$ keV) (blue). Background events above ($1.37 < E < 1.52$ keV) and below ($1.07 < E < 1.22$ keV) have been subtracted to obtain a purer distribution with only normal pulses. Furthermore, the background is plotted as the green distribution in figure 4.9. The counts on the y-axis correspond to the number of events from the 1.3 keV line, illustrating the lower statistics compared to the 10.37 keV line (see figure 4.8). Because of the wider x-axis range the lack of slow pulses ($RT \gtrsim 2.6$) in the blue compared to the green distribution can be seen.
Gaussian curves have been fitted to the distributions, although below roughly 7.5 keV the so-called loggauss model fits the asymmetric distributions more accurately [47]. The pulser measurement has a sufficient statistics with approximately 10000 recorded events and the reduced chi-squared statistic ($\chi^2_\nu = \frac{\chi^2}{\mathrm{NDF}} = 7$)[4] which confirms that the Gaussian is not

[4]NDF is the abbreviation for Number of Degrees of Freedom.

the best fit function anymore. The distribution of the 1.3 keV line is not very smooth, i.e. a few dips and spikes occur, due to the lack of statistics. Nevertheless the Gaussian fit parameters together with the observations by eye are a good indicator to assess the method.
The mean (μ) and the width (σ) of the pulser measurement (red) and the 1.3 keV line (blue) coincide within the uncertainties. The shift of the background distribution (green) towards lower risetimes is reasonable as interactions close to the readout electrode become more frequent towards lower energies, i.e. the lower normal population becomes more dominant. Hence, it confirms that the pulser measurements resemble homogeneously generated pulses from within the diode, i.e. normal pulses (green distribution). Therewith, the comparison to the 1.3 keV line validates our method perfectly.

4.2. Influence of noise at low energy

4.2.1. Modeling the τ-distribution

Towards lower energies the impact of the noise on the pulse and, therefore, the risetime fit becomes significant. This can be strikingly seen in figure 4.13 where three example pulses at circa 210 eV with various risetimes are fitted. Based on them one can imagine that the risetime distribution might broaden towards lower energies, the number of failed fits might increase and the trigger efficiency might decrease.
With a model of the risetime distribution for a given input pulse at various energies one would gain knowledge about the previous mentioned properties. Furthermore, by comparing the modeled distribution from different input pulses the propagation of uncertainties concerning the input pulse towards lower energies can be estimated. This will be used in section 5.3.1 to examine the effect of the discrepancies between the pulser measurement and the 10.37 keV line towards lower energies.

4.2.2. Noise Generator

In this section an additional tool is introduced to investigate the influence of the noise on the risetime distribution and to estimate systematic uncertainties. The idea is to simulate real pulses artificially by adding randomly generated noise samples to a mean pulse.
The generated noise samples are based on real measurements of the individual baselines of the detectors. The recording window has been put to the largest value possible, 1310660 ns instead of the 20000 ns typically recorded. With the auto trigger setting by CoMPASS a random trigger can be used. The mean magnitude, i.e. the mean frequencies within the sample, and the standard deviation of all the measured samples are calculated in Fourier space, see figure 4.10. The larger window size enables the registration of lower frequencies.

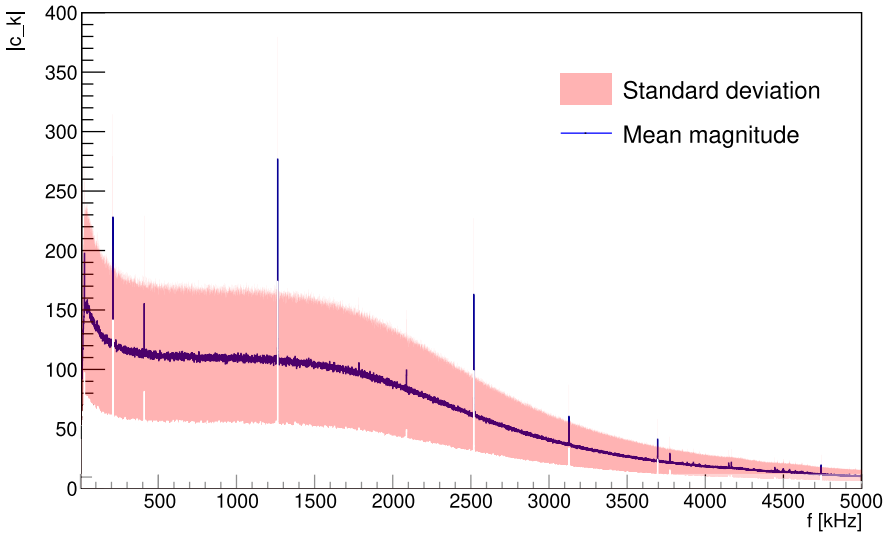

Figure 4.10. The mean Fourier spectrum (magnitude) of > 1000 baseline samples with a length of > 1 ms. The standard deviation for each frequency is represented by the shaded region around the mean. The spectrum is plotted for frequencies up to 5000 kHz. The peaks in the spectrum come e.g. from vibrations of the cryocooler.

By varying the frequencies around their corresponding standard deviation and doing the inverse Fourier transform one ends up with a generated noise sample. Thus, it is possible to generate noise samples on demand which simulate real measured noise. A more precise description of the calculation steps can be found in appendix A.

The mean pulse could either be a mean output pulse from a pulser measurement or an expected pulse from the convolution. By adding a generated noise sample onto the mean pulse and performing the risetime fit we get the τ-parameter of the generated pulse. Repeating it with many generated noise samples yields a generated risetime distribution which can be compared to a measured one.

In figure 4.11 the measured risetime distribution from a pulser measurement at 10.37 keV is compared to a generated one. The mean pulse from the measurement has been used for the generated pulses. The mean and the standard deviation of the two curves match closely (< 1 % difference) which validates the noise generator procedure. One notices that the generated distribution is slightly shifted to the right ($\Delta RT \approx 0.001$). The reason for this small deviation is the mean building process, since $RT = 2.142$ of the mean pulse from the measurement.

Comparing the risetime distribution at lower energies is of greater interest. At low energies the relative contribution of the noise to the pulse is large. Hence, a more precise pulse is obtained by building the mean pulse of a measurement at a higher energy and scaling it down, i.e. adapt the height of the pulse H to the energy. Since the relation is linear we can use $H(E) = H(10.37\,\text{keV}) \cdot \frac{10.37\,\text{keV}}{E}$. The height is defined as the difference between the maximum and the baseline[5].

[5] The baseline can be determined very precisely through the conducted noise sample measurements.

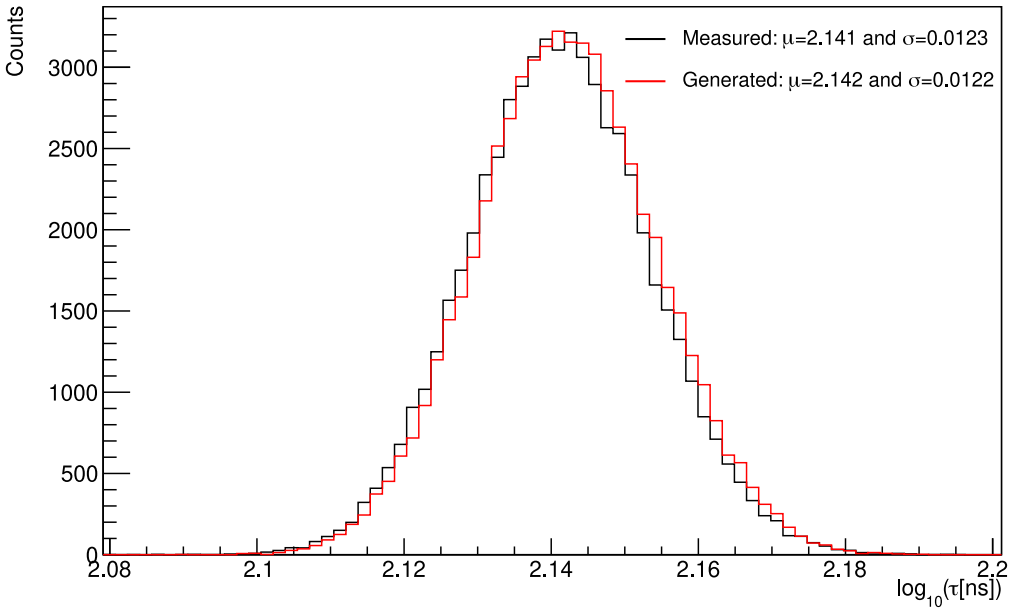

Figure 4.11. The risetime distribution from a pulser measurement at 10.35 keV compared to a generated distribution at the same energy. The mean μ and the standard deviation σ are obtained by fitting a Gaussian.

Another effect that has to be accounted for is the trigger efficiency in the sub-keV region. Below approximately 400 eV the CAEN might not trigger anymore on the pulses because the pulse height becomes too low. However, when calculating the generated risetime distribution we assume that it triggers every event (100 % trigger efficiency). Hence, we need to compare the generated distribution to a pulser measurement with 100 % trigger efficiency, which can be achieved by an external forced trigger. The used pulser [91] possesses two output channels, the first is connected to the 'Test' Input of the corresponding detector, the second channel is directly connected to the CAEN board, the so-called trigger signal. The CAEN is set up such that the trigger signal forces the recording in the 'physical' channel, i.e. the channels connected to the detectors. For a more precise description of the forced trigger setup we refer to chapter 4.4.1 in [47]. The two output signals of the pulser can be set to the same frequency but to different amplitudes. Hence, the trigger signal can have a high amplitude guaranteeing the CAEN to trigger (100% trigger efficiency), whilst the signal of interest can be set to lower amplitudes to investigate the noise. With this method we can be sure that every triggered event underlies an injected pulse, whereas, in the 'normal' trigger mode, i.e. trigger on the 'physical' channels, injected pulses could be missed (trigger efficiency $< 100\%$) or it could trigger on pure noise.

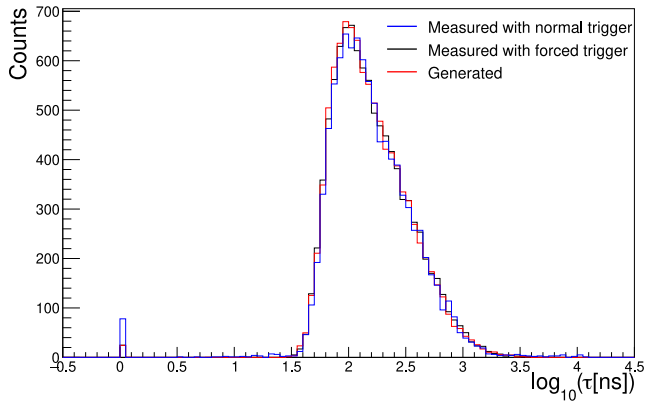

(a) Energy of 380 eV.

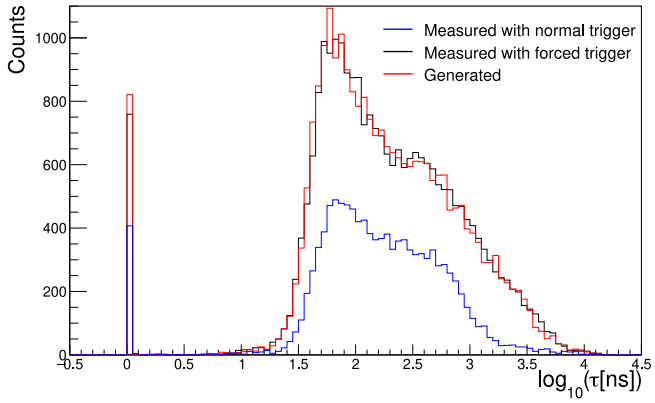

(b) Energy of 210 eV.

Figure 4.12. Comparison between a generated (red) and measured risetime distribution with normal trigger (blue) and forced trigger (black). The events at zero correspond to failed fits. The measured distributions are scaled to the corresponding measurement time and the generated distribution to the forced trigger distribution. In (a) the energy is 380 eV and in (b) 210 eV.

In figure 4.12a the generated risetime distribution with a scaled mean pulse from the 10.37 keV measurement is plotted in red and the measured distribution with forced and normal trigger in black and blue, respectively, at an energy of 380 eV. The good agreement between the measured τ-distributions is expected as we have a trigger efficiency of almost 100 % at 380 eV. Furthermore, it can be seen that the generated distribution has the same shape as the measured ones. Hence, it can be concluded that the broadening of the risetime distribution towards lower energies is indeed dominated by the noise. The zeroth bin resembles the number of events where the risetime fit did not converge, so-called failed fits. It can be seen that the blue distribution has much more failed fit events than the other two, because in the normal trigger mode sometimes noise events are recorded[6].
In figure 4.12b the distributions at an energy of 210 eV are compared. A clear discrepancy between the distributions from the two trigger modes (black and blue) is observed. The measured distributions are scaled with respect to the corresponding measurement time.

[6] With an energy cut these events would vanish.

The blue distribution contains 45 % of the events within the black distribution which corresponds to the trigger efficiency at this energy. Particularly, for events with very high and low risetimes the trigger mechanism of the CAEN is not so sensitive anymore. At this energy (210 eV) the number of failed fits is increasing, especially for the forced trigger mode, i.e. for 3 % of the total events the risetime fit does not converge anymore. The stronger influence of the noise is accountable for that. In figure 4.13 three example pulses with various risetimes are fitted. Based on the three pulses the broadening of the risetime distribution is understandable as the fit becomes weak due to the dominant noise.
Nevertheless, the generated distribution (red) is once again in very good agreement with the distribution using the forced trigger (black). Therefore, the generated distribution can be trustworthily used to estimate the systematic uncertainties related to the noise influence of the pulser measurement at low energies by varying the mean pulse and examining the corresponding τ-distribution. This will be done in section 5.3.1.

In summary of this chapter, the tools for a precise characterization of the physical pulses were developed and validated in section 4.1. Hence, the distributions obtained from the pulser measurements with the modified input pulses can be used to perform the PSD analysis which is subject to the next chapter (chapter 5). Being able to model the risetime distributions precisely with the noise generator (section 4.2) even at low energies enables the estimation and reduction of the systematic uncertainties compared to [47], as can be seen in 5.3.1.

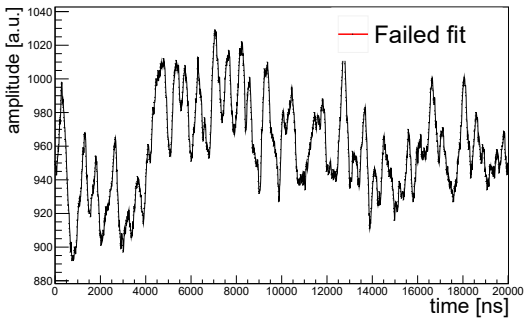

(a) Failed fit.

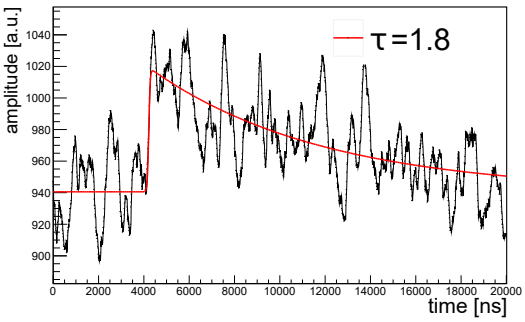

(b) $\tau = 1.8\,\mathrm{ns}$.

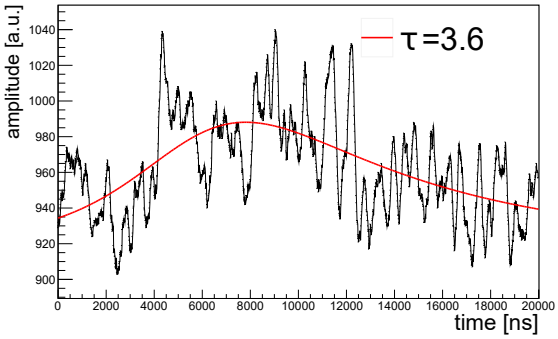

(c) $\tau = 3.6\,\mathrm{ns}$.

Figure 4.13. Example pulses with the corresponding risetime fit at energies of roughly 210 eV.

Chapter 5

Results of the PSD-cut

In this chapter the analysis of the performed PSD-scan is shown. At first, the conduction of the scan with the used input pulse and the pulse generator settings is explained (section 5.1). On the basis of so-called figure of merits the cut efficiencies are optimized such that $\frac{\Delta S}{S}$ is minimized, where S describes the CEνNS signal rate (section 5.2). With the uncertainty estimation on the efficiencies (section 5.3) the final cut values (τ_{cut}) together with the expected background suppression is presented in section 5.5 for all four detectors.

5.1. Conduction of the PSD-scan measurement

In the following the PSD-scan measurement for the C1 detector is explained, the scan for the other detectors has been conducted in the same manner.
The output from the pulse generator goes via a 40 dB attenuator into the 'Test' input of the C1 detector. The lowest and highest possible adjustable voltages at the pulser are 50 mV and 5 V, respectively. With the inserted 40 dB attenuator it covers the ROI and the 10.37 keV line. The output from the detector is as usual connected to the corresponding channel in the CAEN board.
In figure 5.1 the input pulse used for the C1 detector is depicted, it is divided into five regions: The baseline, characteristic for the detector (red); the rising edge modified via the iterative distortion method (section 4.1.3) (black); the flat top (yellow) region and a linear decay (green) back to the baseline (red). Overall, the pulse is set to take 50 µs to avoid the decay of the input pulse back to the baseline within the recorded 20 µs. Furthermore, the decay back is chosen rather moderate to prevent a trigger on the decay. The pulses are sent out periodically with a frequency of 100 Hz and the amplitude is changed to cover the entire energy spectrum.
As already described in section 4.1.4 the input pulse has been chosen because of the good agreement with the risetime distribution of the 10.37 keV line (see figure 4.8). Measurements at 18 different energies have been conducted between 210 eV and 14.1 keV. In figure 5.2 five distributions are plotted exemplarily. A clear broadening towards lower energies due to the increasing influence of the noise can be seen. The broadening is not symmetric when reaching lower energies.
In the next section 5.2 the most beneficial cut efficiencies are calculated for the various energy points within the ROI.

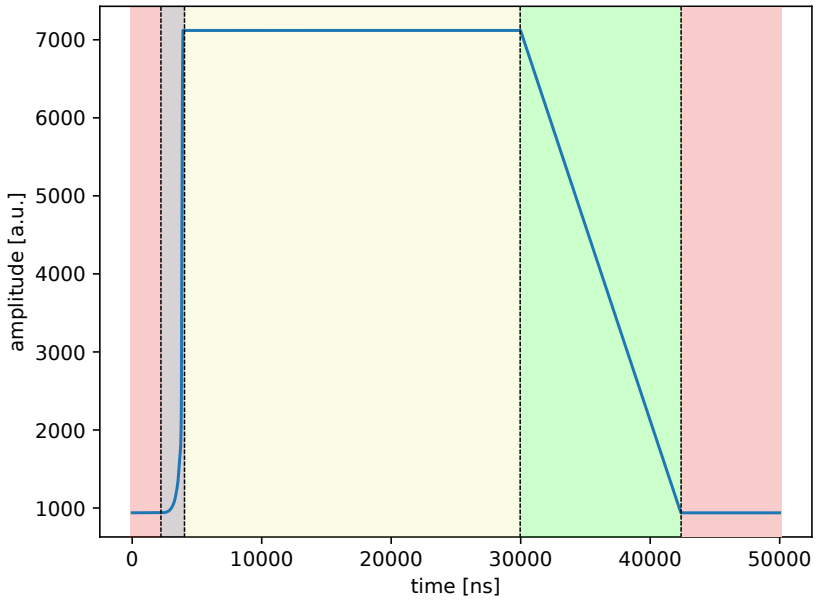

Figure 5.1. The input pulse used for the PSD-scan for C1. The length is 50 µs. It is divided into five regions whereby the rising edge in the black region has been obtained via the shifting method.

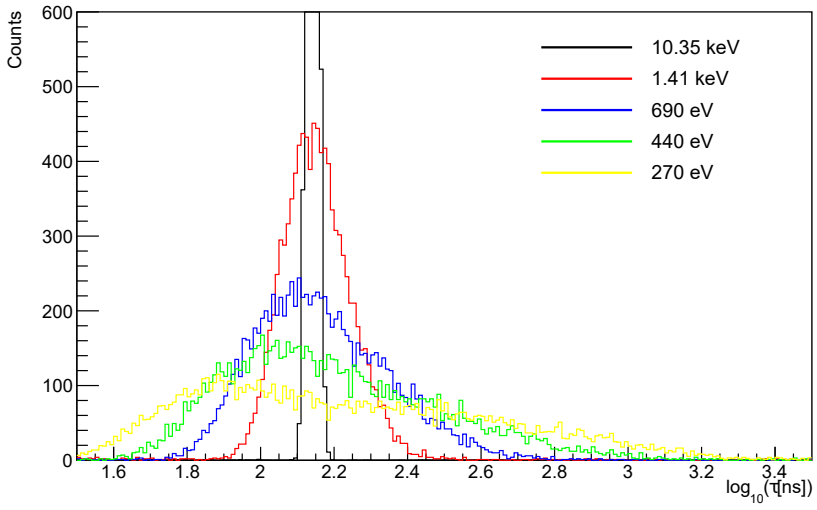

Figure 5.2. Five exemplarily distributions from the PSD-scan with the modified input pulse for C1. The distributions broaden towards lower energies due to the increasing influence of the noise.

5.2. Figure of Merit

Having measured the normal pulse distributions at different energies, cut values τ_{cut} for a given efficiency can be determined. The question arises which is the favored efficiency to obtain the best CEνNS signal. For a high efficiency τ_{cut} will be high and much background will remain. For a low efficiency a good background suppression is achieved (τ_{cut} is low), however also neutrino events get lost. Hence, these two factors need to be balanced. In principle, $\frac{\Delta S}{S}$ should be minimized to achieve the most precise signal rate S, while ΔS denotes the uncertainty, here only the statistical uncertainty.
As a simple, statistical ansatz the signal rate can be written as

$$\begin{aligned} S &= R_{\text{ON}} - R_{\text{OFF}}, \\ &= (R_\nu + R_{\text{bkg}}^{\text{ON}}) - R_{\text{bkg}}^{\text{OFF}}. \end{aligned} \tag{5.1}$$

R denotes the rate and the indices bkg and ν correspond to the background and neutrino rate, respectively. The uncertainty follows directly via

$$\Delta S^2 = \Delta R_\nu^2 + \Delta R_{\text{bkg}}^{\text{ON}\,2} + \Delta R_{\text{bkg}}^{\text{OFF}\,2}. \tag{5.2}$$

To rewrite the rates into number of counts N, a multiplication with the measured times T is necessary

$$\begin{aligned} R &= \frac{N}{T}, \\ \Delta R &= \frac{\Delta N}{T} = \frac{\sqrt{N}}{T} = \sqrt{\frac{R}{T}}. \end{aligned} \tag{5.3}$$

In the latter equation the statistical Poisson uncertainty on the number of counts $\Delta N = \sqrt{N}$ has been used. Inserting (5.3) into (5.2) yields

$$\begin{aligned} \Delta S^2 &= \Delta R_\nu^2 + R_{\text{bkg}}\Big(\frac{1}{T_{\text{ON}}} + \frac{1}{T_{\text{OFF}}}\Big), \\ &= \frac{1}{T_{\text{ON}}^2}\Big[N_\nu + N_{\text{bkg}}^{\text{OFF}}\frac{T_{\text{ON}}}{T_{\text{OFF}}}\Big(1 + \frac{T_{\text{ON}}}{T_{\text{OFF}}}\Big)\Big], \end{aligned} \tag{5.4}$$

where we utilized in the first step the equality of the background rate R_{bkg} for reactor-ON and reactor-OFF. Dividing through the squared signal rate $S^2 = R_\nu^2 = \frac{N_\nu}{T_{\text{ON}}}^2$ yields

$$\Big(\frac{\Delta S}{S}\Big)^2 = \frac{1}{N_\nu}\Big[1 + \frac{N_{\text{bkg}}^{\text{OFF}}}{N_\nu}\frac{T_{\text{ON}}}{T_{\text{OFF}}}\Big(1 + \frac{T_{\text{ON}}}{T_{\text{OFF}}}\Big)\Big]. \tag{5.5}$$

The number of neutrino events N_ν is estimated by the CEνNS signal prediction which has been kindly provided by Thomas Rink for RUN-5. For $N_{\text{bkg}}^{\text{OFF}}$ the measured spectrum during the OFF time of RUN-5 is used. By applying the PSD-cut, the observed neutrino events are reduced by the efficiency ϵ. Simultaneously, the background is suppressed by a factor $R(\epsilon) = 1 - \frac{\text{counts with PSD}}{\text{counts without PSD}}$, which depends on $\tau_{\text{cut}}(\epsilon)$ and, consequently, ϵ itself.

By inserting these factors (5.5) reads

$$\left(\frac{\Delta S}{S}\right)^2 = \frac{1}{N_\nu \epsilon}\left[1 + \frac{N_{\text{bkg}}^{OFF} R(\epsilon)}{N_\nu \epsilon}\frac{T_{\text{ON}}}{T_{\text{OFF}}}\left(1 + \frac{T_{\text{ON}}}{T_{\text{OFF}}}\right)\right]. \tag{5.6}$$

Plotting this equation with respect to the efficiency ϵ is called figure of merit because the minimum yields the most beneficial cut efficiency. The procedure to generate the figure of merit is explained in the following:
The cut values τ_{cut} are determined based on the pulser measurement for efficiencies between 80 and 99.9 % in steps of 0.1 %. By cutting the so far measured reactor-OFF spectrum (from 01/22 - 07/22) at τ_{cut} the events surviving the PSD-cut $N_{\text{bkg}}^{\text{OFF}} R$ are obtained. For the τ_{cut} determination with the pulser distribution and for the background spectrum the failed fits have been discarded. They will be specifically addressed in section 5.4.
For each pulser measurement the mean energy and the standard deviation is obtained by fitting a Gaussian to the energy distribution. For each energy point events in the OFF spectrum within 2σ are considered. Thus, $N_{\text{bkg}}^{\text{OFF}} R$ is calculated for every energy bin (10 eV) within $E_{\text{mean}} \pm 2\sigma$. With the signal prediction N_ν averaged over 10 eV bins equation (5.6) can be calculated bin-wise and afterwards added together. Since the reactor will not be ramped up again, the measured reactor-ON time (T_{ON}) is finite. The OFF-data we use here, however, are not complete as the data taking continued beyond the 01.07.22. Because $N_{\text{bkg}}^{\text{OFF}}$ scales with the first T_{OFF} in (5.6) the longer OFF-time only alters the second ratio of $\frac{T_{\text{ON}}}{T_{\text{OFF}}}$. With the used OFF-data for this analysis the fraction is slightly above 1. Since the data taking is planned to be stopped soon, a ratio slightly below 1 is expected at the end of RUN-5. For this analysis the second ratio in (5.6) is simply set to 1, for the first ratio the measured ON-time will be used and the OFF-time corresponding to the spectrum $N_{\text{bkg}}^{\text{OFF}}$.
The resulting curves of $\left(\frac{\Delta S}{S}\right)^2$ with respect to the efficiency, i.e. figure of merit, for energies between 210 and 980 eV are plotted in figure 5.3. Low efficiencies are not favored as the gain in background suppression is little compared to the loss in neutrino events. At efficiencies between 94.7 - 99.7 % minima marked by the orange lines are reached. They are separately plotted as the black curve (C1) in figure 5.4 as the most beneficial cut efficiencies. The most beneficial cut efficiencies for the detectors C2-C4 have been calculated in the same manner and are plotted in their standardized colors in figure 5.4, too. The corresponding figure of merits for each energy of C2-C4 can be found in the appendix in figure B.1.
For energies above 380 eV (figure 5.3 (a) - (g)) a steep increase after the minimum occurs because τ_{cut} reaches the clearly separated slow pulse population and slow pulses start to get cut as well. At lower energies (figure 5.3 (h) - (j)), however, the population are more intermingled resulting in a weaker increase. Furthermore, due to the strongly increasing neutrino signal expectation at lower energies as illustrated by the black line in figure 5.4 higher cut efficiencies are favored. In figure 5.5 the background τ-distributions at 690 and 270 eV are compared. At 690 eV (red distribution) the separation of the normal and slow pulse population is rather clear, resulting in the steep increase when cutting the slow pulses

in figure 5.3 (c). However, in the black distribution (270 eV) the populations are mixed, making it harder to find a distinctive minimum in figure 5.3 (i).

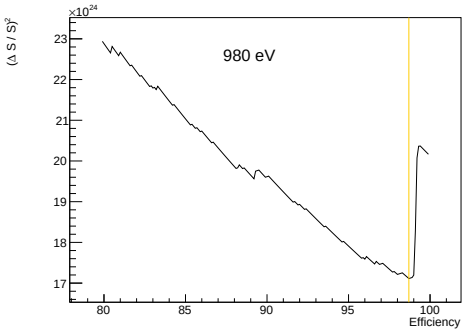

(a) 980 eV

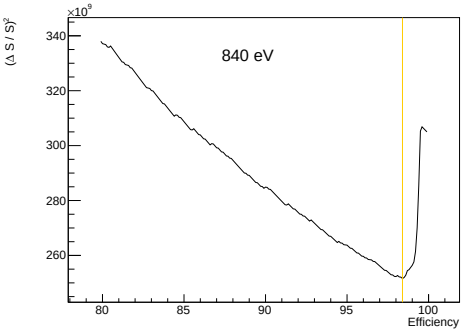

(b) 840 eV

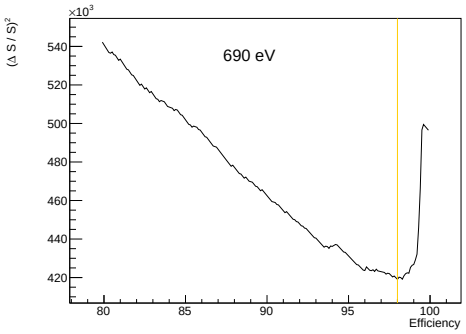

(c) 690 eV

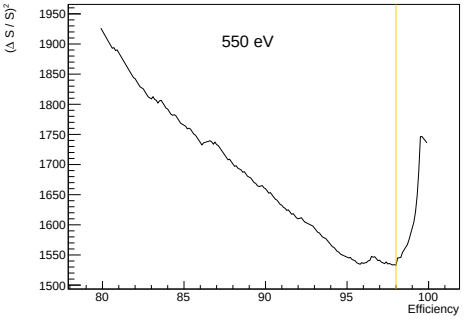

(d) 550 eV

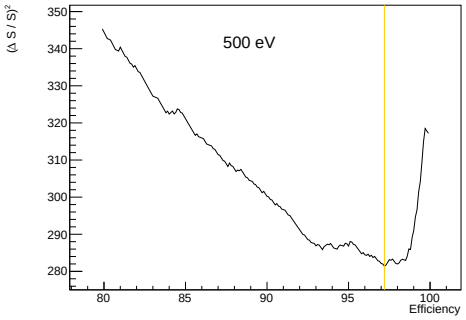

(e) 500 eV

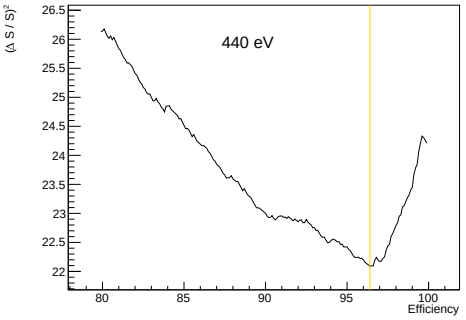

(f) 440 eV

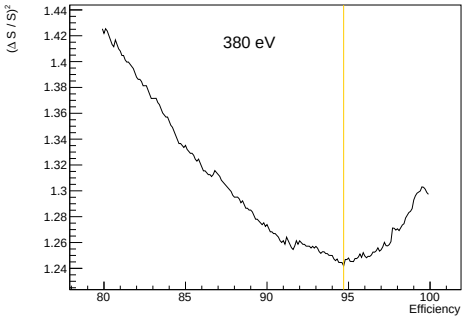

(g) 380 eV

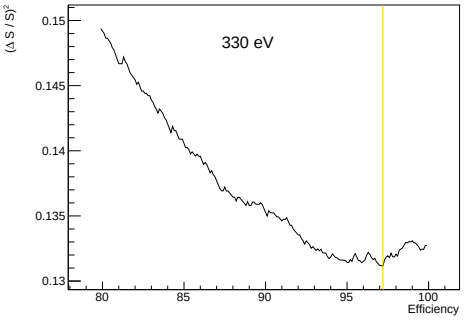

(h) 330 eV

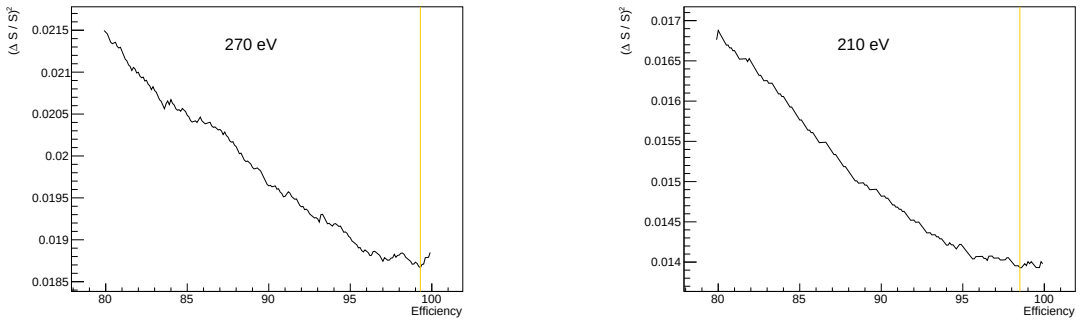

(i) 270 eV **(j)** 210 eV

Figure 5.3. The figures of merit based on (5.6) for the various pulser measurements conducted within the ROI. The minima, i.e. most beneficial cut efficiencies, are marked by orange lines.

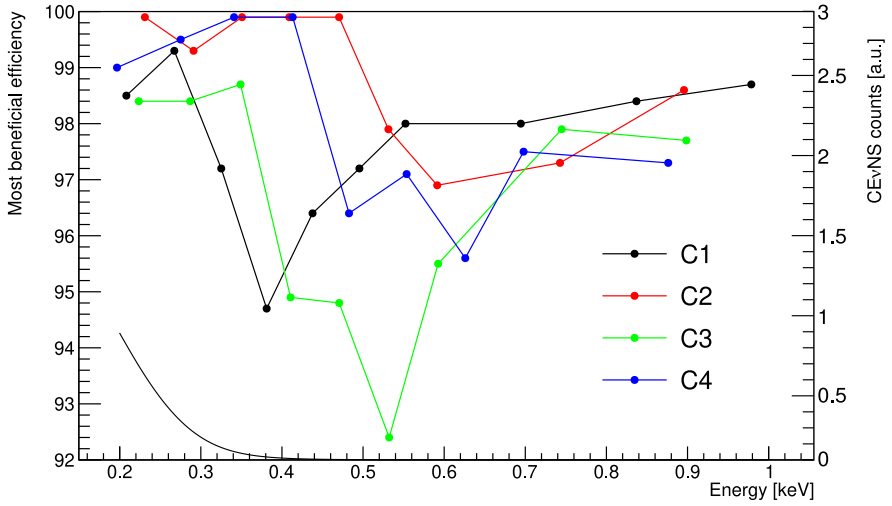

Figure 5.4. The most beneficial cut efficiencies within the ROI for the detectors C1-C4 in the standardized colors. The points are obtained from the minima of figure 5.3. The black curve illustrates the shape of the predicted CEνNS counts for the C1 detector for RUN-5.

Because of statistical limitation of the background data the figures of merit in figure 5.3 are not very smooth, especially around the minima. Hence, small deviation from the minima result still in favorable cut efficiencies. Moreover, by taking a constant efficiency of 97 %[1] throughout the ROI as well as above, the implementation into the analysis gets simplified as the neutrino spectrum is not distorted.

With the efficiency of 97 % at hand τ_{cut} can be determined for the various energies from the pulser measurements. Furthermore, from the OFF-spectrum the background suppression for the τ_{cut}-values can be assessed (section 5.5).

However, so far neither systematic nor statistical errors on the efficiency have been considered in any way. They will be estimated in the next section (5.3).

[1] By looking at figure 5.4 97 % fits quite well for all the detectors.

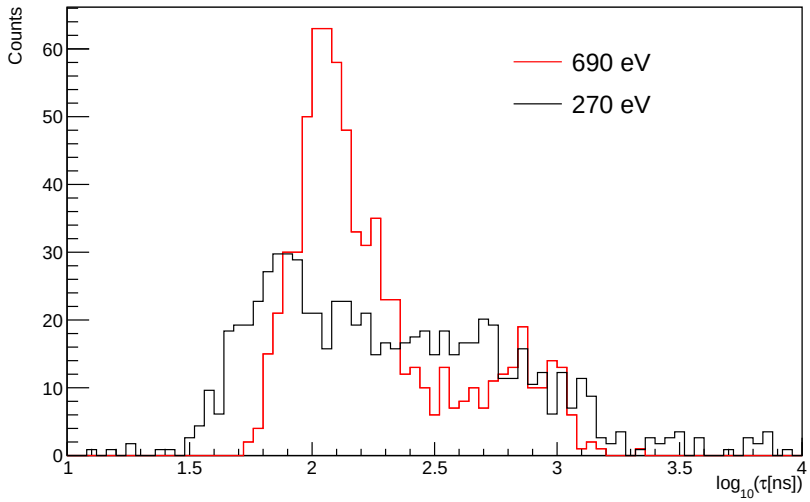

Figure 5.5. Comparison of the reactor-OFF spectrum at 270 ± 70 (black) and 690 ± 70 eV (red). At low energies the slow and normal pulse population are strongly mingled compared to higher energies.

5.3. Uncertainty estimation

In this section the uncertainties on the cut efficiencies for the chosen τ_{cut}-values are estimated. The small remaining differences in the mean (μ) and the standard deviation (σ) between the pulser measurement at 10.35 keV and the 10.37 keV line are propagated with the help of the noise generator to all of the measured energies. This is investigated in section 5.3.1 as systematic uncertainties, whereas section 5.3.2 examines the statistical uncertainties. Last, the stability of the risetime parameter from physical data as well as from the pulser measurement is checked over time (section 5.3.3).

5.3.1. Systematic uncertainties

From figure 4.8 the deviation of the mean (μ) and standard deviation (σ) between the pulser measurement and the distribution from the 10.37 keV line can be read off: $\Delta\mu = 0.0011$ and $\Delta\sigma = 0.0009$.
Since only one input pulse with a specific risetime is used for the pulser measurement, it reproduces a τ-distribution as if the pulses coming from the detector have always exactly the same risetime. However, different interaction positions within the crystal lead to slightly different pulses and risetimes. Thus, the larger σ of the 10.37 keV distribution is justified because the pulses leaving the detector vary a bit in their risetimes. The question is how do these discrepancies affect the pulser measurement at the other measured energies, especially at the lower ones.
For the investigation the simulated pulses (section 4.2.2) are an useful tool to investigate the effect without repeating measurements. The output pulses from pulser measurements

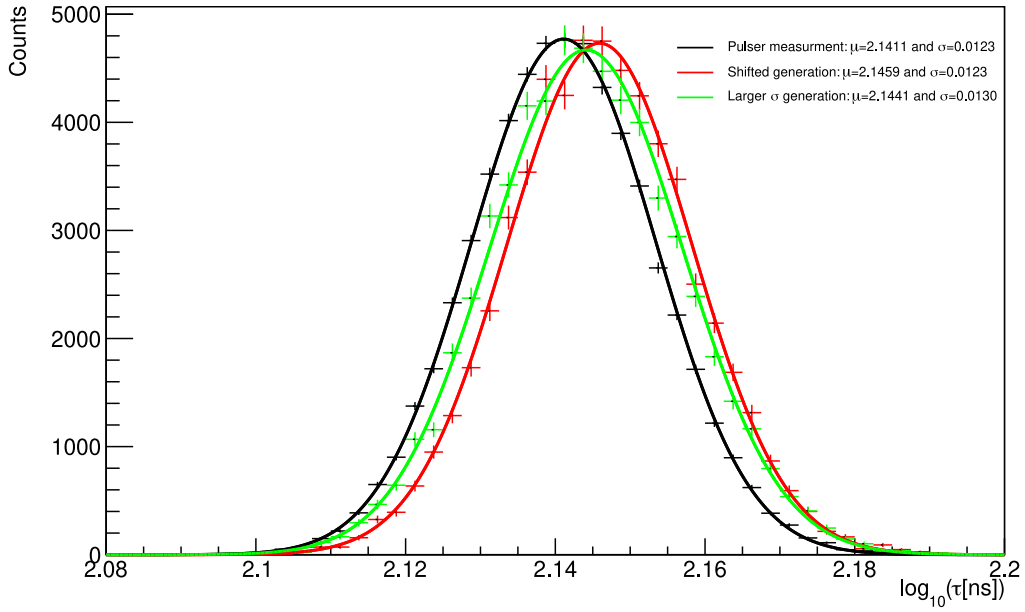

Figure 5.6. The measured pulser measurement (black) at 10.35 keV is compared to generated distributions. The red distributions resembles a shift in the μ-value ($\Delta\mu = 0.0048$) and the green shows a higher σ ($\Delta\sigma = 0.0007$). These pulses are used to investigate how the discrepancies develop at the different energies in figure 5.7.

.

resulting in shifted risetime distributions, i.e. different μ-values, (see e.g. figure 4.7) can be used as mean pulses which can then be combined with noise from the noise generator. Hence, it can be seen how the initial measured shift at 10.37 keV develops at other energies. An input pulse with a higher risetime has been used to model the discrepancy in the mean value. The shifted, generated risetime distribution (red) is compared to the measured one (black) at 10.35 keV in figure 5.6. The discrepancy of $\Delta\mu = 0.005$ is voluntarily higher compared to the real discrepancy of $\Delta\mu = 0.0011$ to exaggerate the effect.
The σ discrepancy ($\Delta\sigma$) has been investigated by generating a distribution with a wider standard deviation. For that six expected pulses from the convolution of modified input pulses with the impulse response with risetimes ranging from $2.138 \leq RT \leq 2.155$ have been combined. In figure 5.6 a distribution with an enhanced width of $\Delta\sigma = 0.0007$ (green) is compared to the measured distribution (black) at 10.35 keV. These pulses are then scaled and noise added on them to get the PSD distributions at various energies.
In figure 5.7 the generated distributions with the shifted mean value and the wider standard deviation are compared to the measured pulser and Th-228 τ-distributions at energies from 1.1 - 14.1 keV. The results of the figures are the following:

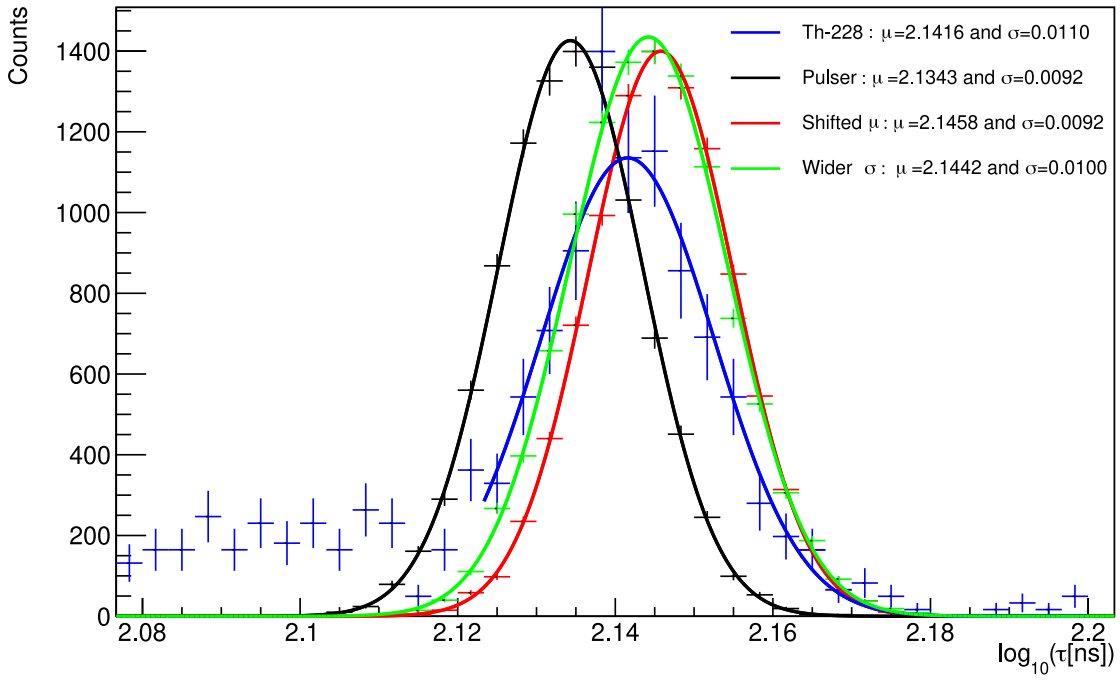

(a) 14.1 keV: $\Delta\mu = 0.0115$ and $\Delta\sigma = 0.0008$.

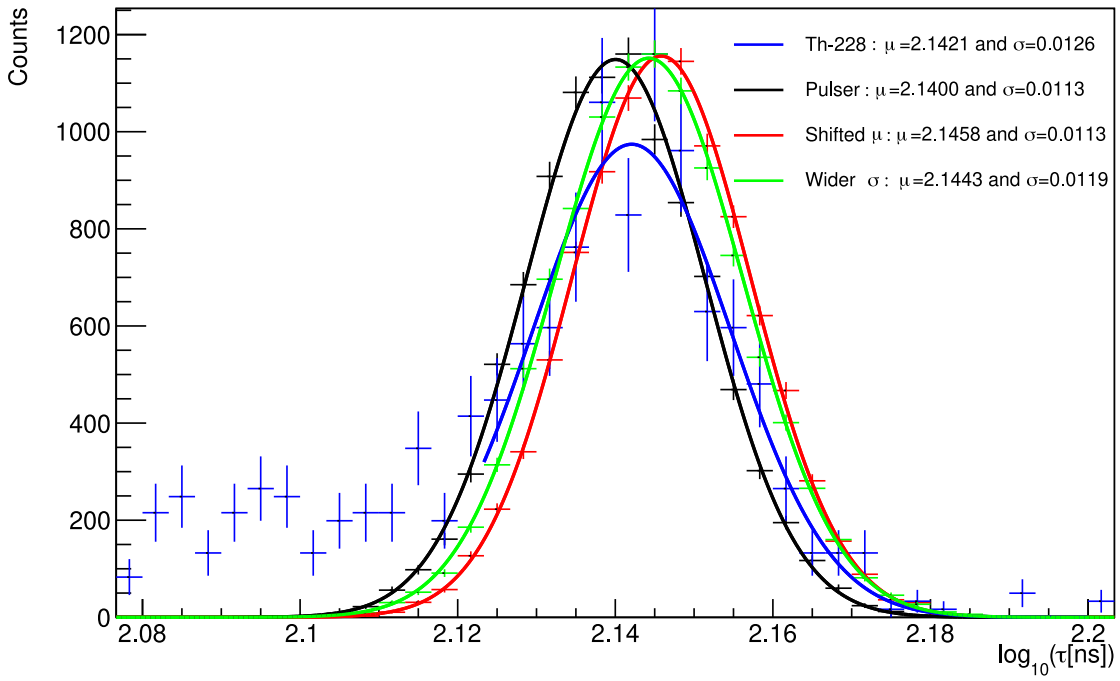

(b) 11.3 keV: $\Delta\mu = 0.0058$ and $\Delta\sigma = 0.0006$.

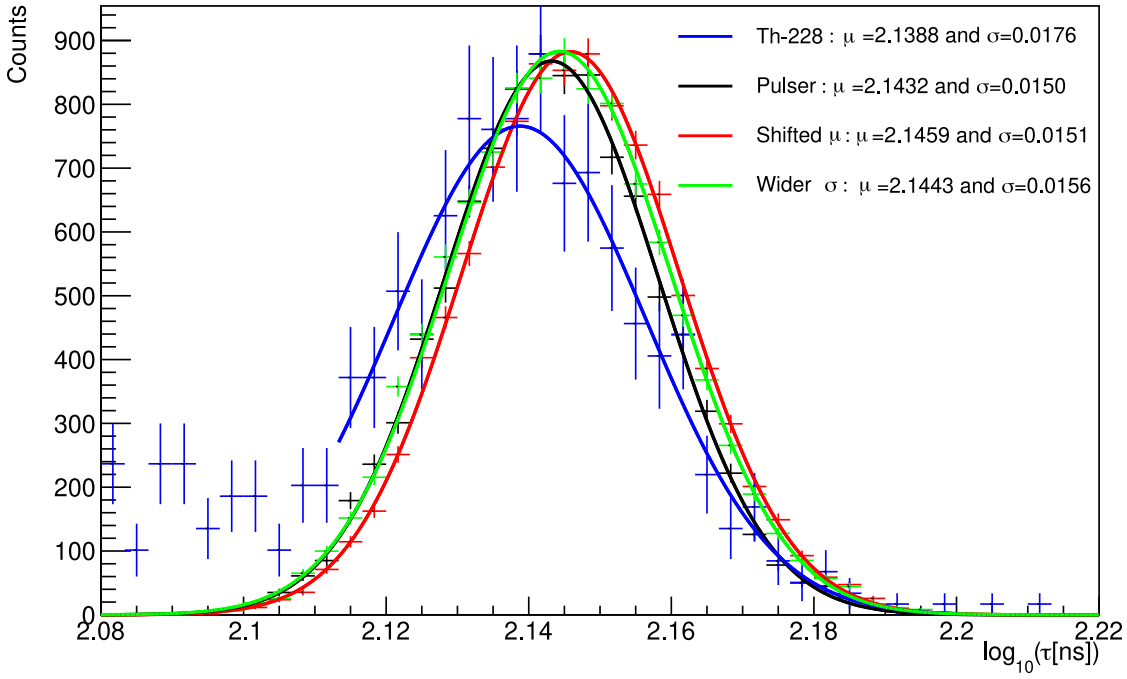

(c) 8.5 keV: $\Delta\mu = 0.0027$ and $\Delta\sigma = 0.0006$.

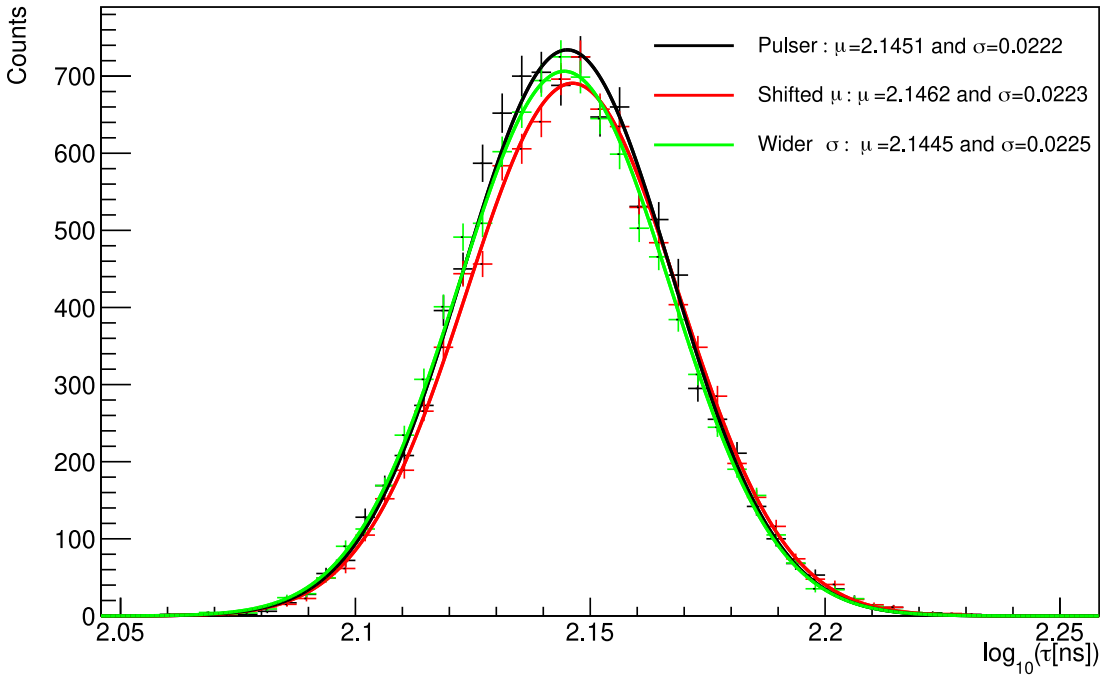

(d) 5.7 keV: $\Delta\mu = 0.0011$ and $\Delta\sigma = 0.0003$.

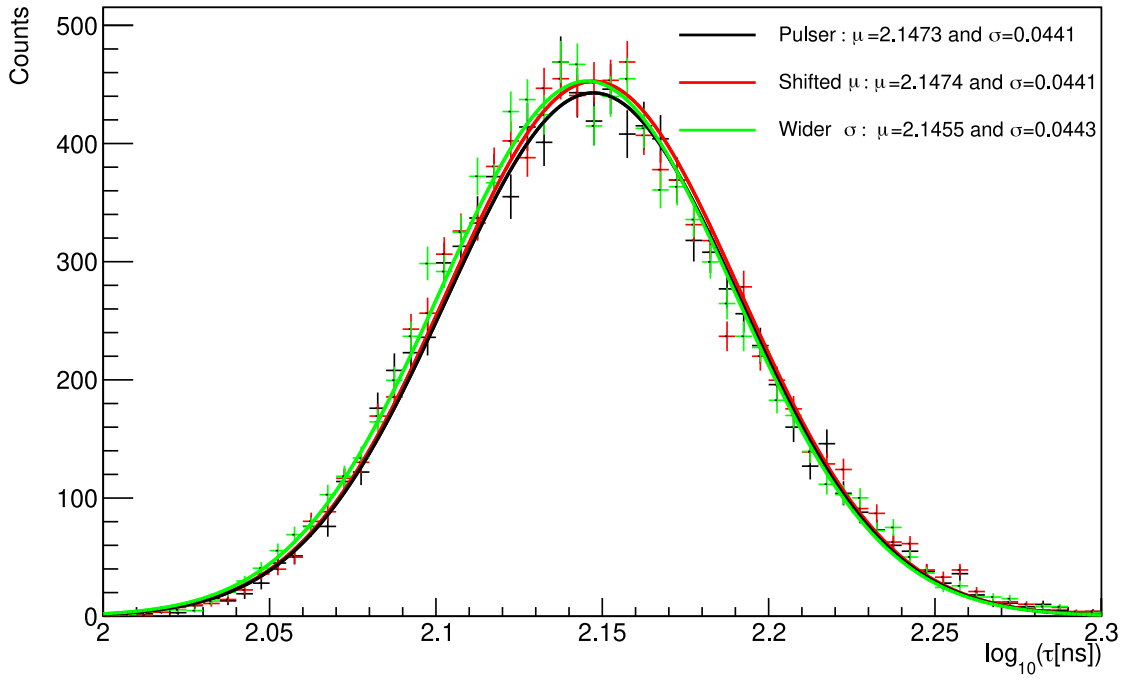

(e) 2.8 keV: $\Delta\mu = 0.0001$ and $\Delta\sigma = 0.0002$.

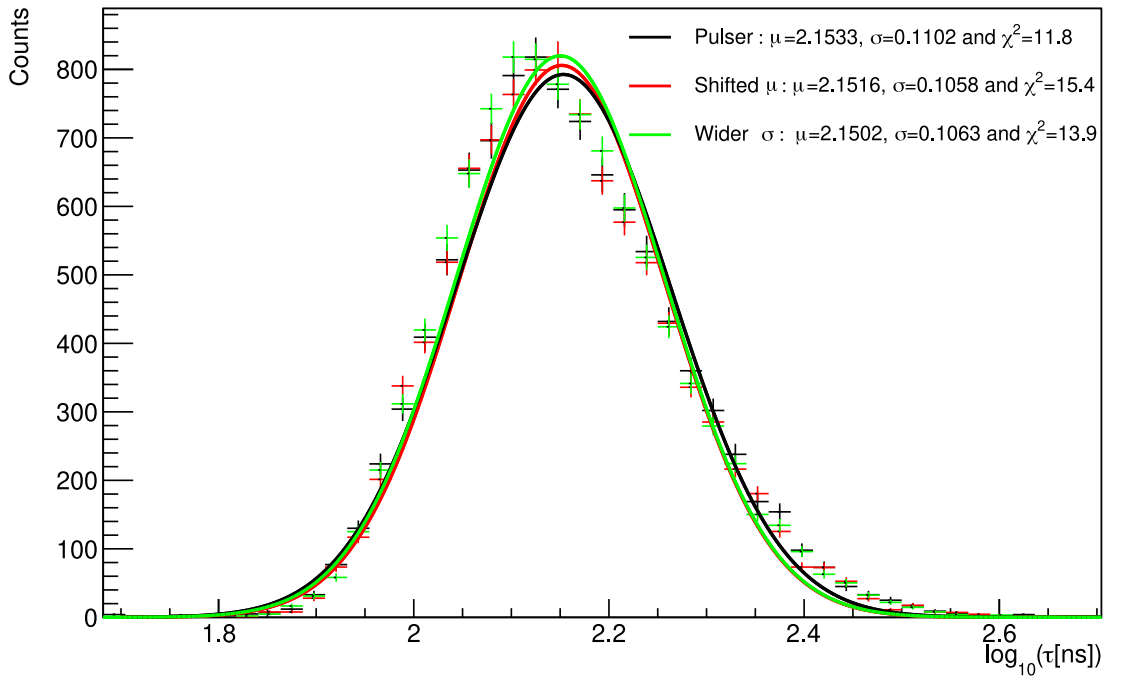

(f) 1.1 keV: Fit becomes too weak ($\chi^2_\nu > 10$) to deliver meaningful parameters.

Figure 5.7. Pulser measurements (red) at various energies are compared to generated distributions. The red distribution resembles a shift in the mean value ($\Delta\mu = 0.005$ at 10.35 keV) and the green a wider distribution ($\Delta\sigma = 0.0007$ at 10.35 keV). The blue distribution at higher energies are events from a Th-228 measurement at the corresponding energy. Together with the energy is the mean discrepancy between the black and the red distribution and the sigma discrepancy between the black and the green distribution shown in the captions of the individual plots.

μ discrepancy (red distribution)

The discrepancy of the mean value is not constant at $\Delta\mu = 0.005$ but increases towards higher and decreases towards lower energies compared to 10.4 keV. At higher energies the strong shift of the distribution from the pulser measurement towards lower risetimes is not physical, since the measured τ-distribution from a Th-228 measurement (blue) stays rather constant at $\mu = 2.142$. An explanation of the shift of the black distribution could be that the attenuator is influencing the risetime strongly at the inputs with a high voltage/energy. More investigation would be needed to understand the effect. However, as these energies are far away from the CEνNS ROI (0.2-1 keV), we simply take the discrepancy to the mean value of the 10.37 keV line as the systematic uncertainty.
As one approaches energies below 10.4 keV the lower normal population becomes more dominant and the distribution from the Th-228 is not so meaningful anymore. Furthermore, as the distribution get wider the μ discrepancy between the shifted (red) and the pulser measurement (black) diminishes. At 1.1 keV (figure 5.7f) the distribution becomes very asymmetric with a reduced chi-squared statistic (χ^2_ν) above 10 when fitting a Gaussian, thus the μ and σ have no significance anymore.

σ discrepancy

At 10.4 keV the generated green distribution is wider by ($\Delta\sigma = 0.0007$) compared to the pulser measurement (black), see figure 5.6. The larger mean value of the green distribution is not relevant as only the width is studied here. At the two energies above 10.4 keV in figure 5.7 the difference stays similar ($\Delta\sigma = 0.0008$ and 0.0006). At lower energies the distributions broaden due to noise and, therefore, the effect of $\Delta\sigma$ gets overwhelmed, e.g. at 2.8 keV the distribution is roughly four times wider $\sigma = 0.0441$ with a discrepancy of only $\Delta\sigma = 0.0002$.

With these observations at hand the systematic uncertainties can be calculated for the various energies in the following way:
For energies above 7.5 keV a Gaussian is fitted to the measured distributions and the mean and standard deviation are adapted: The new mean takes the value from the 10.35 keV measurement ($\mu = 2.1411$) if it is below, as it is the case for the measurements at 11.3 and 14.1 keV. Furthermore, the discrepancy $\Delta\mu = 0.0011$ is added and the width gets enlarged by $\Delta\sigma = 0.0007$. By integrating now the newly obtained distribution until the τ_{cut}, the systematic uncertainty on the efficiency is obtained.
For energies below 7.5 keV the Gaussian fit is not the most accurate anymore [47]. Furthermore, the distributions broaden and the influence of the σ-discrepancy decreases. Hence, solely the μ-discrepancy is added to each risetime value and the systematic uncertainties are obtained based on the newly obtained τ-values.

At higher energies the systematic uncertainties from the discrepancy to the 10.37 keV line play an important role and are roughly estimated here. However, with the help of the noise generator it becomes very clear that towards lower energies the discrepancies become sub-dominant compared to the broadening due to noise. The distribution of energies within the ROI in figure 4.12 range from $RT \approx 1.5$ to 3.5. This illustrates quite well the point that a discrepancy of $\Delta\mu = 0.0011$ and $\Delta\sigma = 0.0007$ is negligible in the ROI. Therefore, the dominant systematic uncertainties reported in [47] are now negligible thanks to the control of the input pulse shape with the method developed in chapter 4.

5.3.2. Statistical uncertainties

The efficiencies are fixed to 97% for all energies as discussed in section 5.2. By sorting the τ-values obtaind from the pulser measurements by magnitude[2], τ_{cut} can be directly read off at the position 0.97 times number of events (ca. 10000). To calculate the uncertainty on the efficiency there are two common methods 'Poisson' and 'binomial' error calculation which both fail in limiting cases [95, 96]. As we deal with an efficiency of almost 100 % the 'Bayesian' approach based on Bayes' theorem is more applicable [97, 98]. It gives the probability distribution with respect to the cut efficiency with the maximum at 97% in our case. The uncertainty can be estimated as a 68.3% confidence interval [95–98]. For low statistics the probability distribution broadens, resulting in a larger uncertainty. The lowest number of events after cutting the failed fits is 9788 at 380 eV which yields an statistical error of ±0.17 % (for an efficiency of 97.00%). The corresponding Bayesian probability distribution with the 68.3 % confidence interval can be seen in figure 5.8. With a relative error of 0.17 % the statistical error is already small, further reduction would be feasible by increasing the number of measured events. Since a frequency of 100 Hz can be set at the pulser, the recording of 10000 events just takes 100 seconds.
The statistical error is similar for every energy because the efficiency is constant and the number of recorded events varies only slightly around 10000 each measurement. The systematic error, however, decreases towards lower energies. The resulting efficiency with the relative systematic and statistical error contributions whilst also considering the converging fit efficiency (section 5.4) can be seen in figure 5.11.

5.3.3. Tau stability pulser and measurement

The stability of the τ-parameter in the data over the entire data taking period (ON and OFF) is crucial to avoid new systematics due to time dependence [47]. For that purpose the Gaussian mean of the normal population in the energy range between 25 and 32 keV is constantly monitored via Th-228 measurements which are performed about once or twice a month. The stability of the τ-parameter is plotted in figure 5.9a until July 2022. It shows

[2]The failed fits are once more neglected.

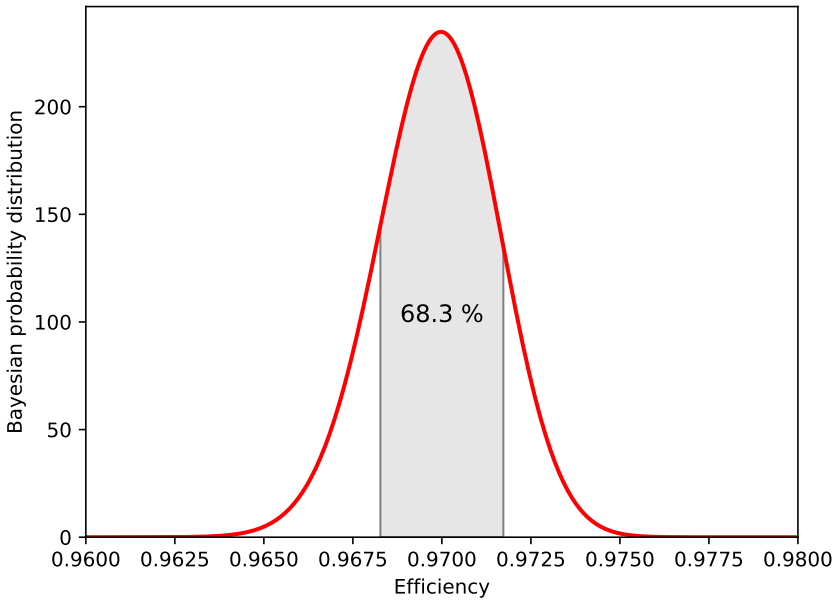

Figure 5.8. The Bayesian distribution with the 68.3 % confidence interval for the pulser measurement at 380 eV.

that the τ-parameter is stable throughout more than a year of data taking. The maximum variation from the mean value of 139.0 ns is 0.3 ns, resulting in a relative variation of 0.2 %. This variation is comparable to the discrepancy of the pulser measurement to the 10.37 keV line observed in figure 4.8 and, therefore, also covered by the investigation of the systematic uncertainties in section 5.3.1. Furthermore, the main discrepancies come only from two data points in figure 5.9a, thus when considering all of the data points the uncertainty becomes negligible compared to the systematic uncertainty observed in figure 4.8.
Apart from the stability of the τ-parameter due to effects of the diode, the stability of the risetime due to pulser and DAQ effects is complementary important to monitor. To use the modified input pulses is not possible since no continuous measurement with the same input pulse has been conducted over the whole period of RUN-5. However, the so-called pulser resolution, which correlates with the energy threshold, is constantly monitored via pulser measurements at KBR. The used input pulse is just an exponential decay. Thus, the risetime value is different to the mean values obtained from the data or with the modified input pulses. Since we just want to monitor the stability of the pulser it is sufficient. The mean τ-value, by fitting a Gaussian to the peak, is plotted with respect to the time of the measurement in figure 5.9b. The maximum deviation is only 0.07 % relative to the mean value ($\sim$ 101 ns) over the period of almost one year. Hence, it can be quite rightly assumed that the output pulses sent by the pulser are stable throughout the data taking period.
It has been shown that the risetime parameter of the data as well as the pulser is stable throughout RUN-5. As the noise is responsible for the broadening of the τ-distributions a monitoring of the noise would be of great interest, too. However, no specific baseline

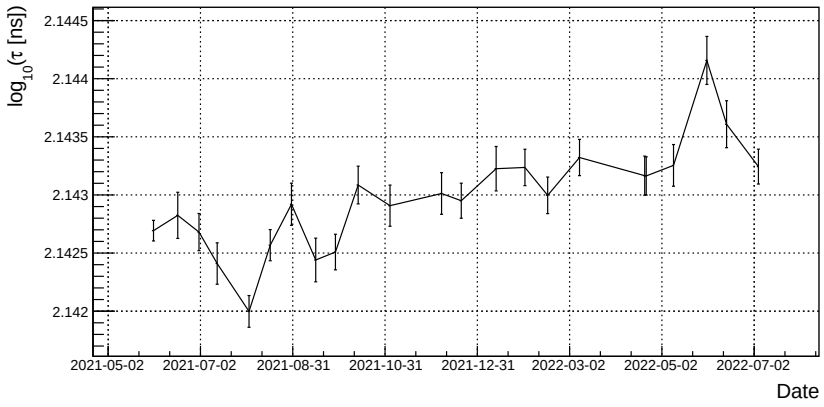

(a) τ-stability of the data.

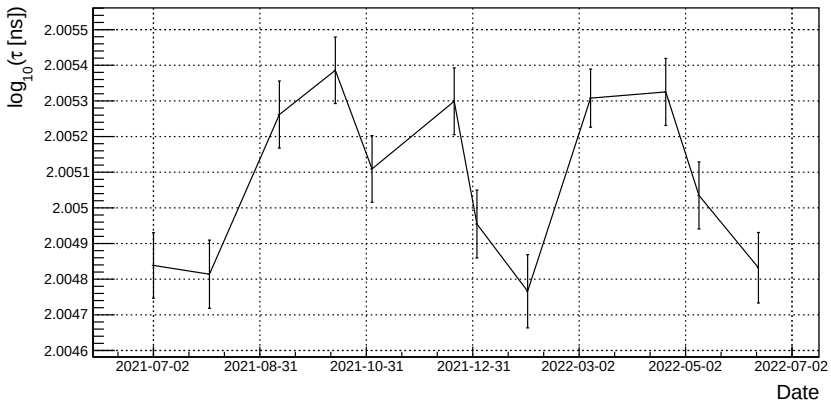

(b) τ-stability of the pulser.

Figure 5.9. Stability monitoring of the τ-parameters over time.

measurements with an increased recording window have been conducted regularly during RUN-5. The pre-trigger before the pulses could in principle be used to monitor the baseline in a future work.
In the appendix B.2 the stability of the τ-parameter is shown and discussed for the detector C2-C4. They seem to be less stable over time than C1. The deviations over time are at most $\Delta\mu = 0.007$ for C2 which is only slightly larger than the deviation of $\Delta\mu = 0.005$ studied in section 5.3.1. Hence, it is safe to say that the systematic uncertainties due to time instabilities are negligible in the ROI for all four detectors.

5.4. Converging fit efficiency

As already seen in figure 4.12 and 4.13a not all of the risetime fits converge, especially at low energies. The procedure so far to determine τ_{cut} for the most beneficial cut efficiency has neither considered the failed fits of the pulser measurement nor the background spectrum. Based on the pulser measurement the efficiency that the fit of a normal pulse converges can be defined as the so-called 'converging fit efficiency'.

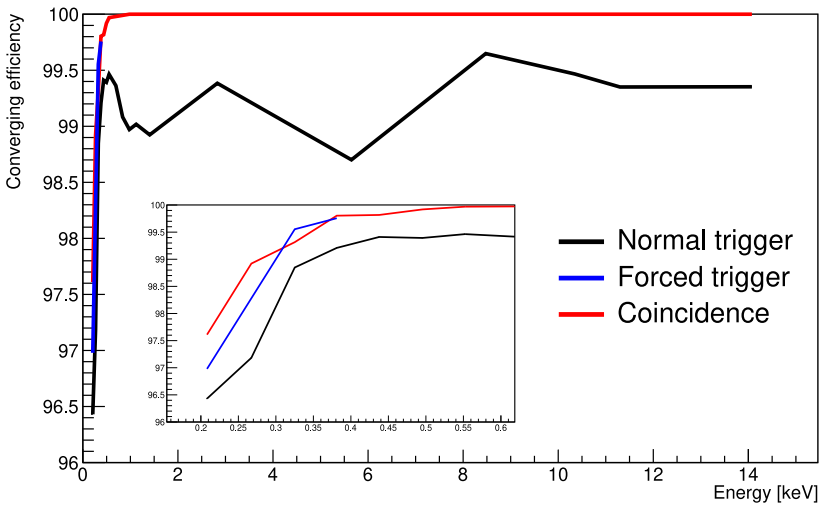

Figure 5.10. The converging fit efficiency with respect to the energy for the forced (blue) and normal trigger with (red) and without (black) coincidence. The inset shows lower energies (200 to 600 eV) in greater detail.

Considering the measurement with the normal trigger mode most of the failed fits come from triggered noise events and no physical normal pulses underlie them. The forced trigger mode is also not applicable as it forces the CAEN to trigger at every event although in the normal mode the CAEN would not trigger. The optimum procedure would be to use the normal trigger but consider only the events coming from the pulser. This can be done by connecting the second output of the pulser to a free CAEN channel and saving the timestamps of the signals. By demanding a coincidence between the timestamps of the two CAEN channels only the events which underlie a pulse from the pulser are kept. Hence, the converging fit efficiency states how many of the incoming normal pulses are actually assigned a τ-value and, conversely, for how many the fit is not converging.
In figure 5.10 the converging fit efficiencies for the three above mentioned trigger mechanism are plotted, whereby the highest forced trigger measurement has been conducted at 380 eV. In the normal trigger mode without coincidence there are failed fits even at high energies due to noise events[3]. At very low energies the forced trigger mode shows a lower converging fit efficiency compared to the coincidence mode since it forces to trigger on events where the fit is likely to fail.
Overall, by applying the coincidence there are no failed fits above 1 keV and within the ROI the converging fit efficiency is between 100 % and 97.6 %[4]. To determine the final efficiency the cut efficiency needs to be multiplied with the converging fit efficiency as seen in figure 5.11. Since it is also an efficiency the same statistical uncertainty from section 5.3.2 is applied.

[3]This is also the reason for the fluctuating behaviour.
[4]The 97.6 % correspond to a pulser measurement at 210 eV.

5.5. Efficiency and risetime curves of all four detectors

As described in section 5.2 the cut efficiency has been set to 97 % throughout the measured energy region ($\sim$ 0.2 - 14 keV). To further exclude the failed fits the converging fit efficiency has been introduced in section 5.4. The statistical uncertainty examined in section 5.3.2 is applicable for both efficiencies. Hence, the final efficiency together with the statistical uncertainties can be calculated by

$$\begin{aligned} \epsilon_{\text{stat}} &= \epsilon_{\text{cut}} \cdot \epsilon_{\text{converging}}, \\ {\Delta\epsilon_{\text{stat}}}^2 &= \epsilon_{\text{stat}}^2 \left(\left(\frac{\Delta\epsilon_{\text{cut}}}{\epsilon_{\text{cut}}} \right)^2 + \left(\frac{\Delta\epsilon_{\text{converging}}}{\epsilon_{\text{converging}}} \right)^2 \right), \end{aligned} \tag{5.7}$$

where the propagation of uncertainty has been used in the second step. The systematic uncertainty has been thoroughly estimated in section 5.3.1. The resulting efficiency curve with the corresponding errors is plotted in figure 5.11.
As expected, the systematic uncertainty dominates for high energies (above 8 keV). For lower energies the broadening of the distribution due to noise lowers the influence of the small remaining μ and σ discrepancies. In the ROI the systematic uncertainties are negligible compared to the statistical ones. Surely, the statistical uncertainties could be lower by simply repeating the pulser measurement to get more events. However, within the region of interest the relative uncertainties are already as low as 0.2 %, improving significantly the precision compared to [47].

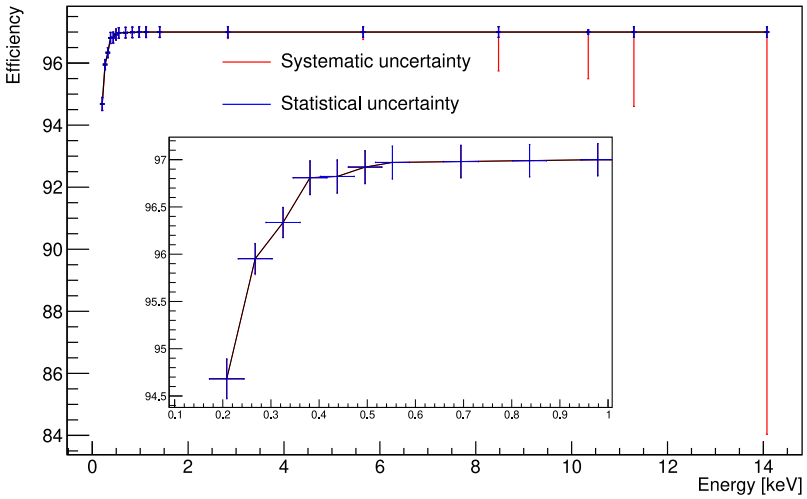

Figure 5.11. The overall efficiency as the product of cut and converging fit efficiency is shown. In red are the systematic and in blue the statistical uncertainties plotted. The systematic uncertainties dominate at high energies and are negligible towards lower energies, especially within the ROI. An inset into the ROI is shown in the enlarged picture.

For an efficiency of 97 % the τ_{cut}-values can be calculated for each pulser measurement while excluding the failed fits. They are summarized in table 5.1 together with the energy of the pulser measurement and the achieved background reduction. For the background reduction events within the mean energy $\pm 2\sigma$ are considered except for the lowest energies, because $208\,\text{eV} - 2 \cdot 35\,\text{eV} = 138\,\text{eV}$ would reach the noise peak and distort the background reduction ($R = 46\%$). Hence, only events above 170 eV are considered. Furthermore, in the last column of table 5.1 the background reduction, where the failed fits have also been cut, is shown. The pulser measurement at 14.1 and 11.3 keV is shifted to the left (see figure 5.7 (a) and (b)) resulting in a low τ_{cut}-value which in turn entails a high background suppression as many normal pulses are cut, too. Furthermore, the listed percentages of background reduction should only give a rough estimate and are not precise values as the statistics, especially at higher energies, is not very large.

Energy [keV]	Efficiency	τ_{cut}	Bkg suppression [%]	Bkg suppression cutting failed fits [%]
14.07	$97.00^{+0.17}_{-12.96}$	2.152	51.3	53.8
11.30	$97.00^{+0.17}_{-2.40}$	2.163	45.7	48.6
10.35	$97.00^{+0.07}_{-1.50}$	2.166	5.8	6.5
8.48	$97.00^{+0.17}_{-0.63}$	2.173	26.4	28.6
5.65	$97.00^{+0.17}_{-0.25}$	2.192	19.7	21.3
2.83	$97.00^{+0.17}_{-0.21}$	2.240	22.1	23.1
1.41	$97.00^{+0.17}_{-0.18}$	2.355	18.2	19.2
1.12	$97.00^{+0.17}_{-0.18}$	2.407	20.2	21.7
0.98	$97.00^{+0.17}_{-0.17}$	2.450	18.0	19.6
0.84	$96.99^{+0.17}_{-0.17}$	2.507	20.6	21.5
0.69	$96.98^{+0.17}_{-0.17}$	2.562	19.6	20.7
0.55	$96.97^{+0.17}_{-0.18}$	2.696	16.2	18.0
0.50	$96.92^{+0.17}_{-0.18}$	2.736	15.8	17.9
0.44	$96.82^{+0.18}_{-0.18}$	2.830	13.4	15.9
0.38	$96.81^{+0.18}_{-0.18}$	2.905	8.9	11.9
0.33	$96.34^{+0.16}_{-0.16}$	2.998	6.9	10.3
0.27	$95.95^{+0.16}_{-0.17}$	3.065	8.1	13.1
0.21	$94.68^{+0.21}_{-0.21}$	3.180	16.2	29.9

Table 5.1. Summarizing for each energy point the τ_{cut}-value, the efficiency and the background (bkg) suppression with and without cutting the failed fits.

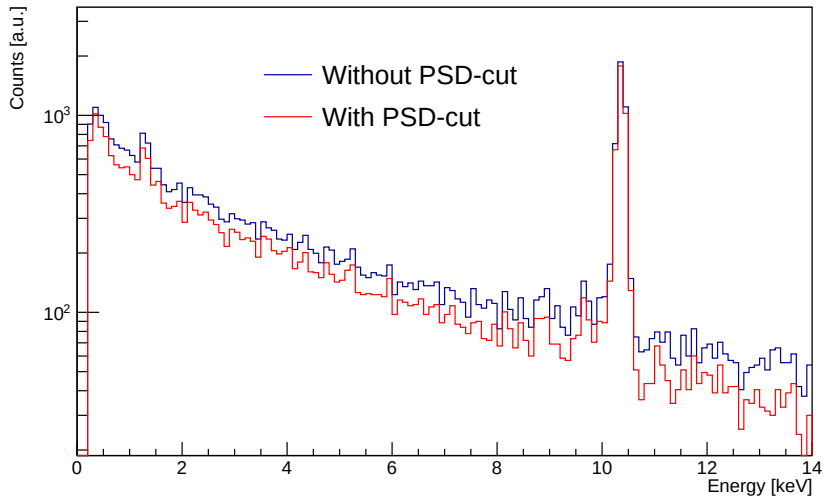

Figure 5.12. Energy spectrum for ca. 4.5 months of Reactor-OFF data with (red) and without applying the PSD-cut (blue).

In figure 5.13 the τ_{cut}-curve is drawn into the OFF spectrum which was used for the calculation of the background suppression and the figure of merits in section 5.2. It can be seen that the curve is very smooth which is another advantage of the constant cut efficiency of 97 %. This enables a liner interpolation between the τ_{cut}-values for the implementation into the CEνNS analysis.
Lowering the efficiency to ca. 90 % would increase the background reduction within the ROI to roughly 25 % due to the strongly mixed populations. However, as seen in the figure of merits 5.3 such efficiencies are not favored to obtain the best sensitivity for CEνNS.
In figure 5.12 the reactor-OFF energy spectrum is drawn without the PSD-cut (blue) and with the PSD-cut (red). The τ_{cut}-values are taken from table 5.1 with a linear interpolation as seen in figure 5.13.

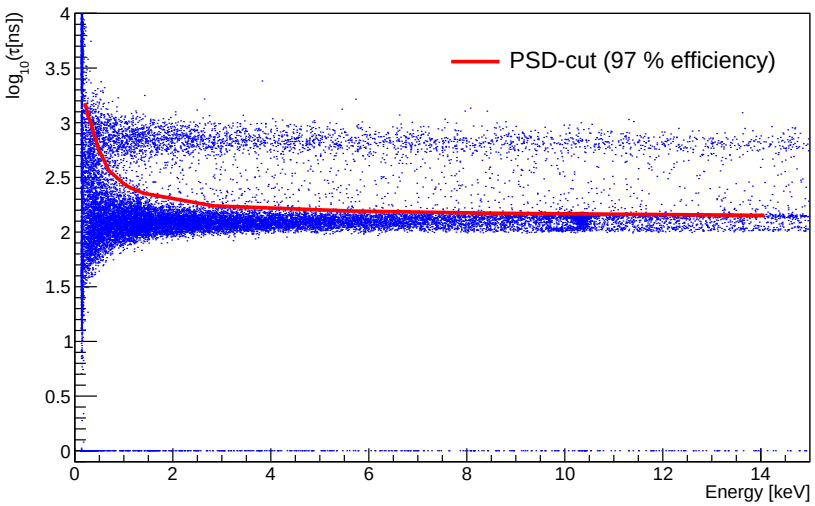

(a) $E = 0 - 15$ keV

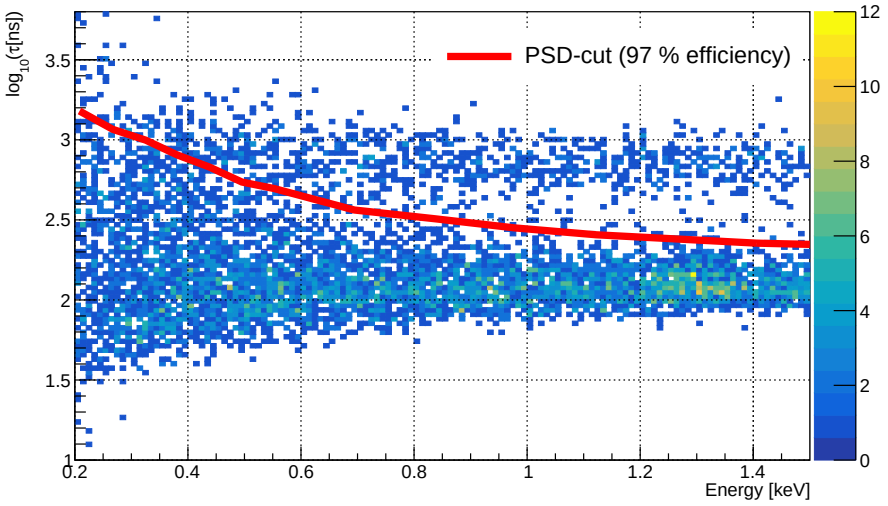

(b) $E = 0.2 - 1.5$ keV

Figure 5.13. Reactor-OFF spectrum (about 4.5 months) with the PSD-cut, i.e. τ_{cut}-values, drawn with a red line inside. (a) shows the entire energy range where pulser measurements have been conducted, (b) is zoomed towards the ROI.

Results of the detectors C2-C4

The same steps as explained throughout the thesis for the C1 detector have also been done for the detectors C2-C4.
First of all, the input pulses for the pulser have been optimized to match best the 10.37 keV distribution as it can been seen in figure 5.14.

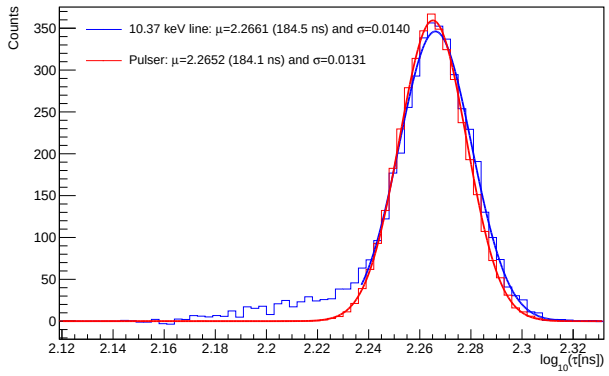

(a) C2

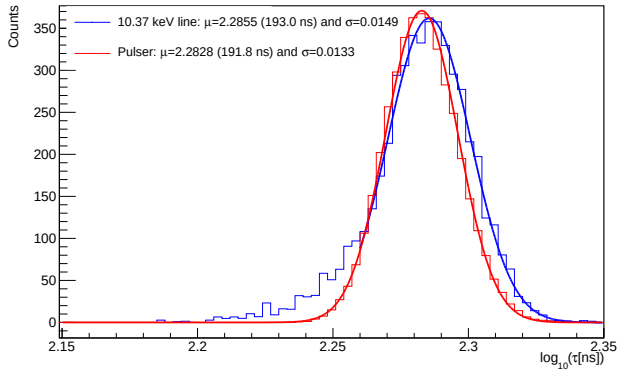

(b) C3

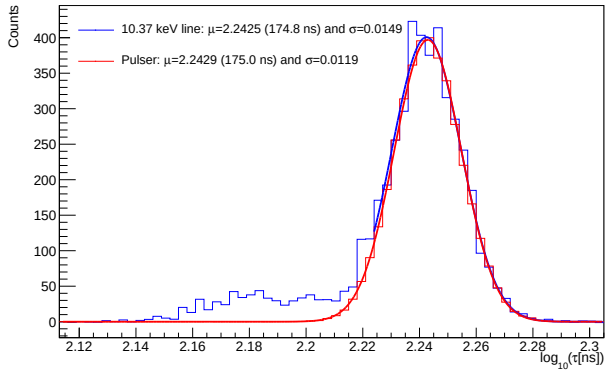

(c) C4

Figure 5.14. Comparison of the τ-distributions obtained from a pulser measurement and from the 10.37 keV line for the detectors C2-C4. They have been generated in the same manner as 4.8.

The discrepancies between the pulser measurement and the 10.37 keV line were propagated in the same way as described in section 5.3.1. The efficiency curve with the statistical uncertainties has been calculated from the cut (97 %) and the converging fit efficiency through (5.7). In figure 5.15 the resulting efficiency curves with the systematic and statistical errors for the detectors C2-C4 are plotted. The systematic uncertainties due to the time instabilities, especially for C2, have not been considered (see figure B.2). However, within the ROI they are negligible compared to the statistical uncertainties as explained in section 5.3.3.

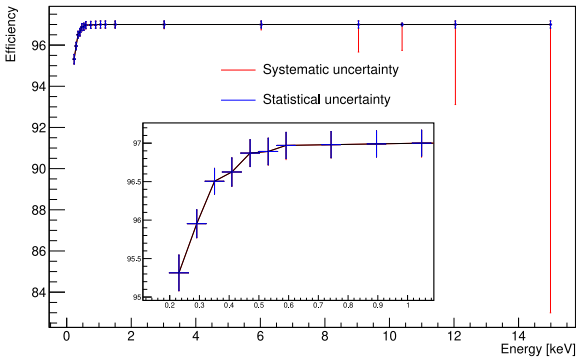

(a) C2

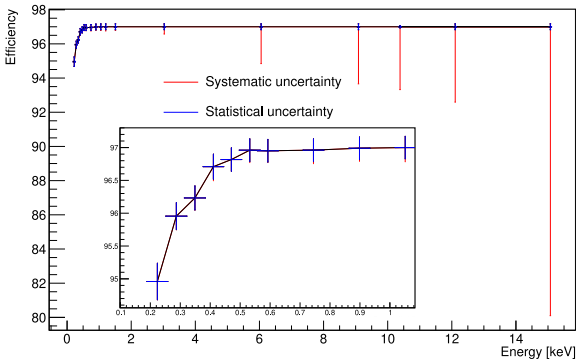

(b) C3

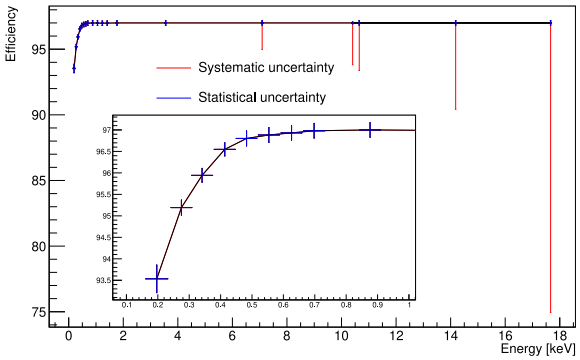

(c) C4

Figure 5.15. The efficiency curves for C2-C4, in the same manner as figure 5.11.

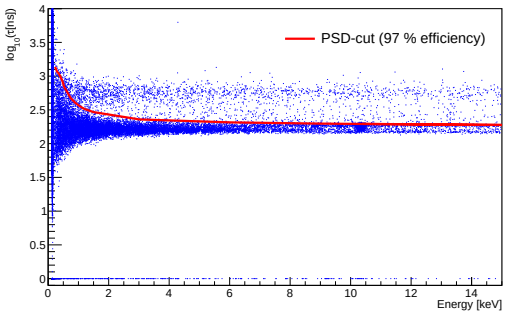

(a) 980 eV

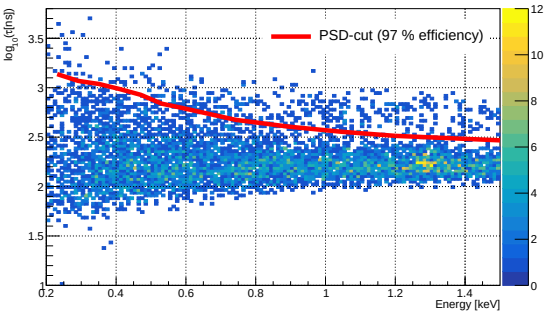

(b) 840 eV

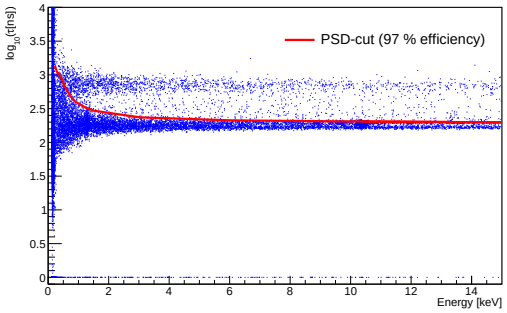

(c) 980 eV

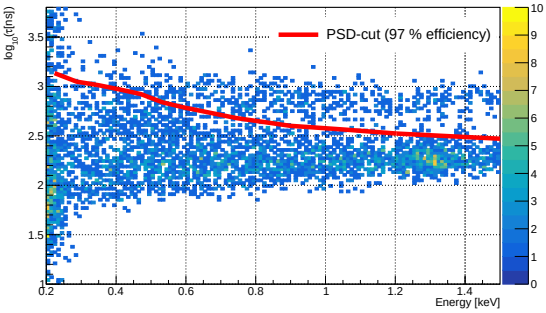

(d) 840 eV

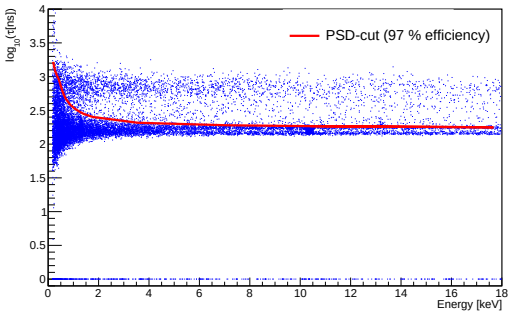

(e) 980 eV

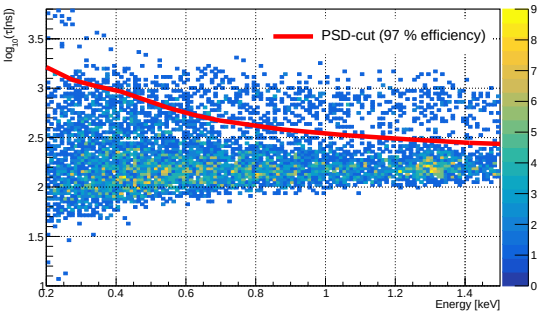

(f) 840 eV

Figure 5.16. Reactor-OFF spectra with the drawn in PSD-cut in red for C2-C4. The left side shows the entire spectra where energy points from pulser measurements exist, whereas the right side shows the ROI in more detail.

The OFF-spectra with the drawn in τ_{cut}-curves can be seen in figure 5.16. The τ_{cut}-values for the corresponding energies and efficiencies are summarized for the detectors C2-C4 in table 5.2. This table together with 5.1 holds the necessary values for the implementation of the PSD-cut for the CEνNS analysis.

C2			C3			C4		
E [keV]	Efficiency	τ_{cut}	E [keV]	Efficiency	τ_{cut}	E [keV]	Efficiency	τ_{cut}
-	-	-	-	-	-	17.66	$97.00^{+0.17}_{-22.06}$	2.249
14.99	$97.00^{+0.17}_{-14.00}$	2.277	15.07	$97.00^{+0.17}_{-16.90}$	2.296	14.18	$97.00^{+0.17}_{-6.58}$	2.258
12.04	$97.00^{+0.17}_{-3.89}$	2.285	12.11	$97.00^{+0.17}_{-4.41}$	2.306	10.65	$97.00^{+0.17}_{-3.62}$	2.265
10.39	$97.00^{+0.07}_{-1.26}$	2.293	10.39	$97.00^{+0.07}_{-3.68}$	2.309	10.41	$97.00^{+0.07}_{-3.19}$	2.266
9.04	$97.00^{+0.17}_{-1.34}$	2.296	9.09	$97.00^{+0.17}_{-3.34}$	2.314	7.09	$97.00^{+0.17}_{-2.03}$	2.279
6.03	$97.00^{+0.17}_{-0.26}$	2.315	6.05	$97.00^{+0.17}_{-2.15}$	2.327	3.55	$97.00^{+0.17}_{-0.20}$	2.317
3.02	$97.00^{+0.17}_{-0.21}$	2.359	3.03	$97.00^{+0.17}_{-0.42}$	2.371	1.77	$97.00^{+0.17}_{-0.17}$	2.403
1.50	$97.00^{+0.17}_{-0.18}$	2.467	1.51	$97.00^{+0.17}_{-0.21}$	2.470	1.41	$96.99^{+0.17}_{-0.18}$	2.447
1.20	$97.00^{+0.17}_{-0.18}$	2.513	1.20	$97.00^{+0.17}_{-0.24}$	2.523	1.23	$96.98^{+0.17}_{-0.17}$	2.483
1.05	$97.00^{+0.17}_{-0.18}$	2.554	1.05	$97.00^{+0.17}_{-0.22}$	2.565	1.05	$96.99^{+0.17}_{-0.17}$	2.525
0.90	$96.99^{+0.17}_{-0.17}$	2.606	0.90	$96.99^{+0.17}_{-0.20}$	2.602	0.88	$97.00^{+0.17}_{-0.17}$	2.583
0.74	$96.98^{+0.17}_{-0.17}$	2.675	0.74	$96.96^{+0.17}_{-0.21}$	2.680	0.70	$96.98^{+0.17}_{-0.17}$	2.672
0.59	$96.97^{+0.17}_{-0.19}$	2.794	0.59	$96.95^{+0.17}_{-0.18}$	2.789	0.63	$96.93^{+0.17}_{-0.17}$	2.727
0.53	$96.89^{+0.17}_{-0.18}$	2.838	0.53	$96.96^{+0.17}_{-0.19}$	2.840	0.55	$96.88^{+0.17}_{-0.17}$	2.796
0.47	$96.87^{+0.17}_{-0.18}$	2.928	0.47	$96.82^{+0.18}_{-0.18}$	2.923	0.48	$96.80^{+0.18}_{-0.18}$	2.883
0.41	$96.63^{+0.18}_{-0.19}$	2.988	0.41	$96.71^{+0.19}_{-0.21}$	2.969	0.41	$96.55^{+0.16}_{-0.16}$	2.967
0.35	$96.51^{+0.17}_{-0.17}$	3.038	0.35	$96.23^{+0.18}_{-0.19}$	3.013	0.34	$95.94^{+0.16}_{-0.16}$	3.022
0.29	$95.95^{+0.18}_{-0.19}$	3.069	0.29	$95.96^{+0.20}_{-0.21}$	3.049	0.28	$95.19^{+0.18}_{-0.18}$	3.084
0.23	$95.31^{+0.23}_{-0.24}$	3.138	0.22	$94.96^{+0.28}_{-0.28}$	3.135	0.20	$93.53^{+0.32}_{-0.32}$	3.219

Table 5.2. The efficiency including uncertainties and the τ_{cut}-value at the corresponding energy for the detectors C2-C4. The values from this table and table 5.1 will be used for the implementation of the PSD-cut for the CEνNS analysis.

The achieved background suppression with the PSD-cut for all four detectors can be seen in figure 5.17. The points at the lowest energy increase strongly, because the selected energy window interferes already slightly with the noise peak. The differences in the reduction between the detectors is expected as the relative contribution of the different background sources vary between the detectors [78]. For C2, the μ-induced neutrons are more dominant compared to the decay of ^{210}Pb and vice versa for C1 and C3 [78]. The γ and e^- decay products from ^{210}Pb get suppressed by the PSD-cut, the neutrons, however, are not much affected as explained in section 3.2. Hence, the lower background reduction of C2 compared to C1 and C3 is reasonable. A more quantitative comparison between the expected reduction based on the background composition and the seen reduction in figure 5.17 for the four detectors would definitely be interesting coupled with MC studies. Moreover, it illustrates that the PSD can be used to gain more knowledge about the contributions of the different background sources.

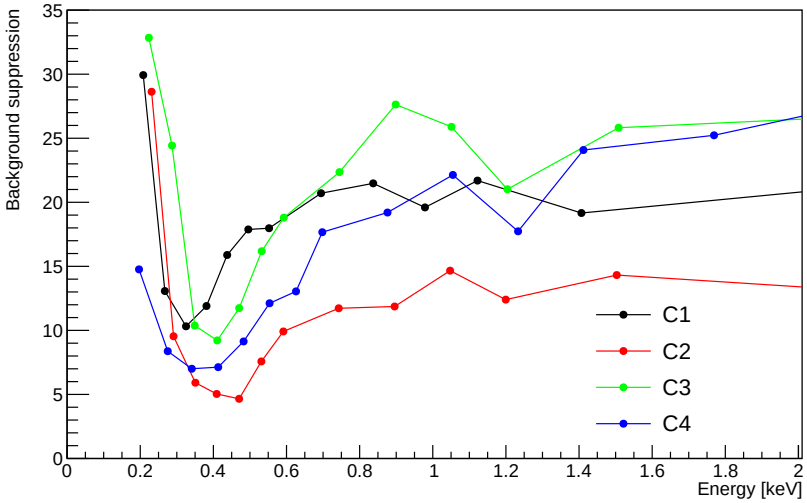

Figure 5.17. The background suppression in percentage terms for the four detectors when applying the corresponding PSD-cut is shown in the low energy regime (0-2 keV).

Chapter 6

Conclusions and outlook

Conclusion

The CONUS experiment aims at detecting Coherent Elastic neutrino Nucleus Scattering (CEνNS) with high purity germanium detectors (HPGe) using a strong flux of reactor antineutrinos at the commercial nuclear power plant in Brokdorf, Germany. Within the first runs of the experiment no significant CEνNS detection has been achieved. For the ongoing RUN-5 a new DAQ by CAEN is used which is expected to lower the noise threshold and allows the recording of the shapes of the individual pulses. The latter enables to classify and discriminate events based on their pulse shapes, so-called Pulse Shape Discrimination (PSD). In the semi-active region (transition layer) between dead and fully active volume of the p-type HPGe diode the charge collection efficiency is below 100 % resulting in a wrong energy reconstruction. Furthermore, the pulses from interactions within the transition layer feature a slower risetime ('slow pulses') compared to events happening in the active volume ('normal pulses').
Neutrinos interact homogeneously within the detector. Background events, especially particles with small absorption length like electrons or low energetic photons, are in comparison more likely to interact in the outer layers. This results in a much smaller signal-to-background ratio in the semi-active compared to the active volume.
The pulse shapes can also be used to monitor the performance of the diode and preamplifier or to discriminate single-site from multi-site events as shown for the CONUS experiment in [47]. This work, however, focused only on the discrimination of slow pulses and showed that a beneficial background reduction within the ROI of the CEνNS analysis ($0.2-1.0$ keV) is possible.
The τ-parameter from the risetime fit acts as the discrimination parameter between slow and normal pulses. At high energies ($\gtrsim 5$ keV) the bands containing the slow and the normal pulses are clearly separated, however, as one approaches the sub-keV range the two bands start to overlap. With artificially generated pulses from a function generator (pulser) the normal pulses can be simulated and studied individually throughout all energies.
In chapter 4 we developed tools to simulate trustworthy physical pulses with the pulser. By taking the electronic response into account the input pulses for the pulser were calculated through the 'iterative distortion method' and validated by comparison with the K- and L-shell line from Ge isotopes at 10.37 and 1.3 keV, respectively. With generated noise samples based on real measured samples the risetime distribution was modeled to study the influence of the noise and to estimate the systematic uncertainties. This leads to a significant reduction of the systematic uncertainties in the ROI for CEνNS (sub-keV) compared to [47].

Based on so-called figure of merits the cut efficiencies, i.e. the number of neutrino events surviving the PSD cut, have been optimized to obtain the best sensitivity for CEνNS as a function of the energy. To implement it into the CEνNS analysis the cut efficiency has been set to 97 % for all detectors and energies, yielding an average background reduction of circa 15 % in the CEνNS ROI. The tables 5.1 and 5.2 state the efficiency and the τ_{cut}-value for each energy at which a pulser measurement has been conducted. Based on these values the PSD-cut will be implemented for the upcoming CEνNS analysis of RUN-5. For the investigation of BSM models like the neutrino magnetic moment and the neutrino millicharge with a ROI of 2-8 keV [56] the method will also be applied.

Comparison to other collaborations applying a PSD-cut

The TEXONO collaboration developed the PSD analysis based on the risetime fit [43, 45]. As they use physical sources and background data and not directly the pulser measurements to calibrate the risetime distributions their main uncertainties come from the statistics [45]. In [43] a constant τ_{cut}-value is applied, which results in a huge loss of efficiency towards lower energies, the efficiency is roughly 60 % at the threshold of 500 eV for their method. Based on the figure of merits developed in this thesis this is by far not a beneficial cut efficiency.
The CoGeNT collaboration uses p-type HPGe detectors to search for Weakly Interacting Massive Particles (WIMPs) [90]. The 'electronic pulser signals are identified to be a close replica of fast radiation-induced events in the bulk of the crystal' [44], in our terminology normal pulses. They use the pulser measurements to calibrate the risetime cut as it was done in this work. The broadening of the τ-distribution towards lower energies due to the increasing influence of noise is also investigated by simulated pulses similar to our noise generation method in 4.2.2 and it shows the same behaviour [44]. However, a cut efficiency of 90 % is applied which is not favored for CEνNS but might be appropriate for WIMPs [90].

Outlook and further improvements

Pulse shape simulations[1] are a further tool to validate the experimentally developed PSD-cut. In the future, the simulations together with a precise knowledge about the radiation sources affecting the detector might be able to predict the exact τ-distributions over the entire energy range. Furthermore, the background composition affects the achievable background reduction through the PSD-cut, i.e. μ-induced neutrons are not much affected in contrast to the γ and e^- decay products of ^{210}Pb, as seen in figure 5.17. A more quantitative study in the future would be insightful. Overall, the PSD analysis provides a further tool to gain knowledge about the relative contribution of the different background sources.
Further investigation of the τ-stability, especially for the C2 detector, are necessary. Furthermore, the continuous monitoring of the baseline and the pulser τ-stability with the

[1] Under current investigation for CONUS by Janine Hempfling.

modified input pulses would be of great interest when applying the PSD-cut on future data.

Based on Monte Carlo (MC) simulations the percentage of slow pulses in the total background in the CEνNS ROI is expected to be roughly 30-40 %[2], depending on the detector. Hence, approximately 50 % of the slow pulses are cut with the developed PSD-cut. With a background reduction greater than 20 % above the ROI nearly 100 % of the slow pulses are cut. However, at the sub-keV range with the favored cut efficiencies (> 95 %) such a high slow pulse suppression is not achievable because of the strong mixing of the normal and slow pulse populations due to the great influence of the noise. Only by lowering the noise threshold a better discrimination would be achievable, which would foremost increase the number of CEνNS signals significantly. Since background events occur in the transition layer as well as the active volume, a PSD-cut is always intrinsically limited.

In the upcoming analysis of the RUN-5 data the background reduction through the PSD-cut will increase the sensitivity and might lead to a CEνNS detection with the CONUS experiment.

[2]The numbers are provided by Janina Hakenmüller.

Appendix A

Noise generator calculation details

Here, the code to randomly generate noise sample based on real measured samples is explained in more detail:
At first it is checked if the sample is purely noise or an event occurred during the recording window. This is simply done by excluding events with values above a certain height. By applying the Fourier transform to the pure noise sample, the magnitude of every frequency bin is obtained. Repeating this step for many samples (> 1000) the mean magnitude (μ) for every frequency bin can be calculated. Knowing the mean value the procedure can be repeated and the standard deviation (σ) of every frequency bin is obtained as well (see figure 4.10).
A new Fourier spectrum can now be generated by varying the mean of every frequency bin Gaussian around the corresponding standard deviation, i.e. the new magnitude is picked from a Gaussian probability distribution with the respective μ and σ. To get a sample in real space, i.e. perform an inverse Fourier transform, the magnitude and phase of every frequency bin is needed. The phase can be chosen randomly for every bin as it only resembles the translation in time but has no impact on the height or the frequency of the noise. The magnitude of the 0^{th} bin resembles the baseline of the sample and the phase is zero as it is always purely real.
By performing the inverse Fourier transform one obtains a generated noise sample (red in figure A.1) based on real measured noise samples. An exemplarily real sample is plotted in blue in figure A.1.

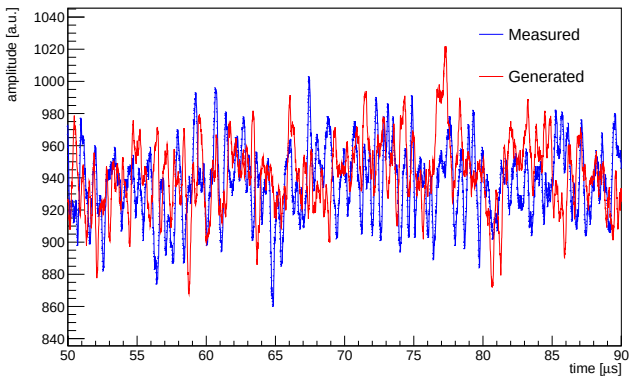

Figure A.1. A generated (red) and a measured noise sample (blue) over a time period of 40 µs. It is a zoomed extraction from the longest possible recording window of the baseline of 1.3 ms.

Appendix B

Additional plots of C2-C4

B.1. Figure of merits for C2-C4

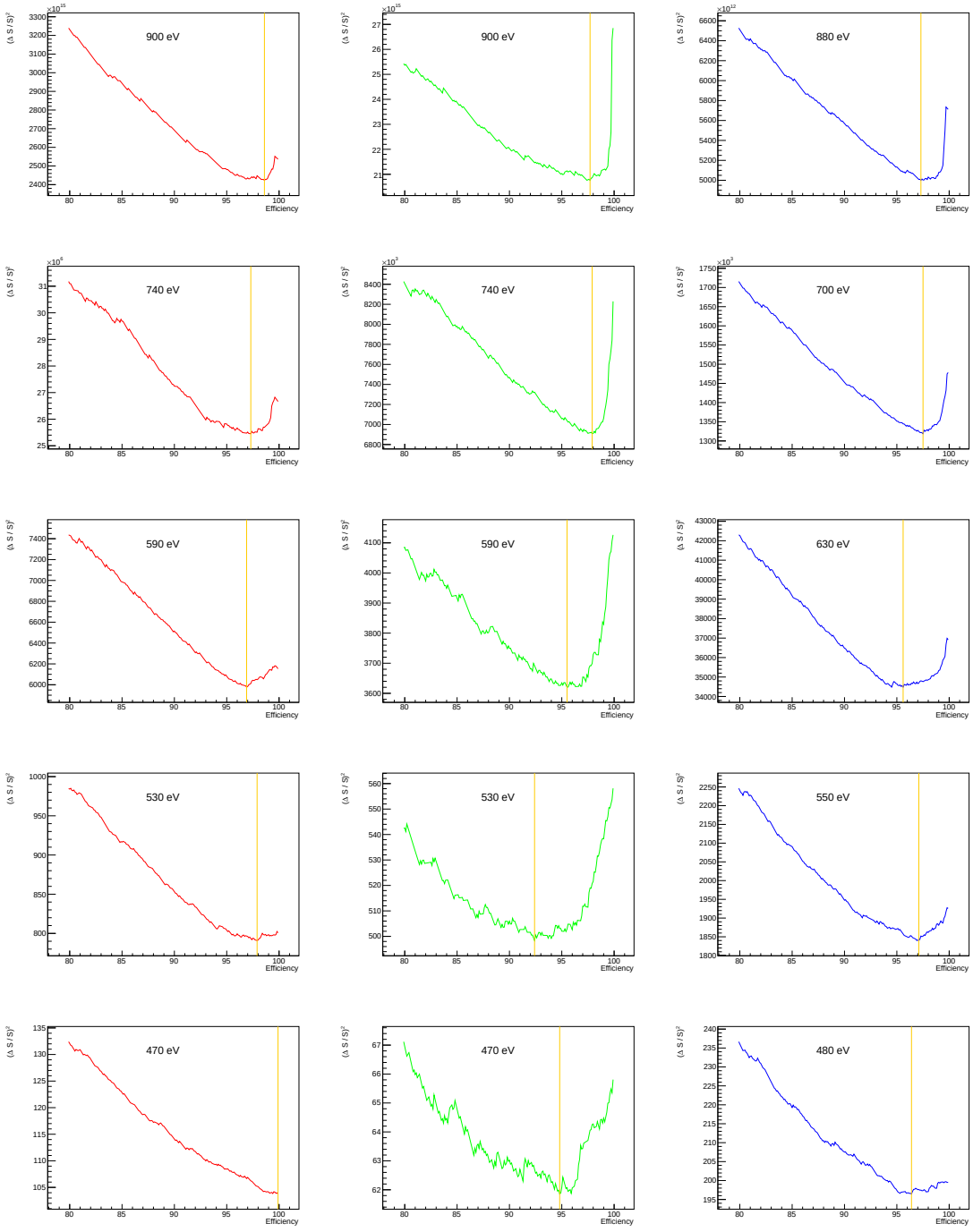

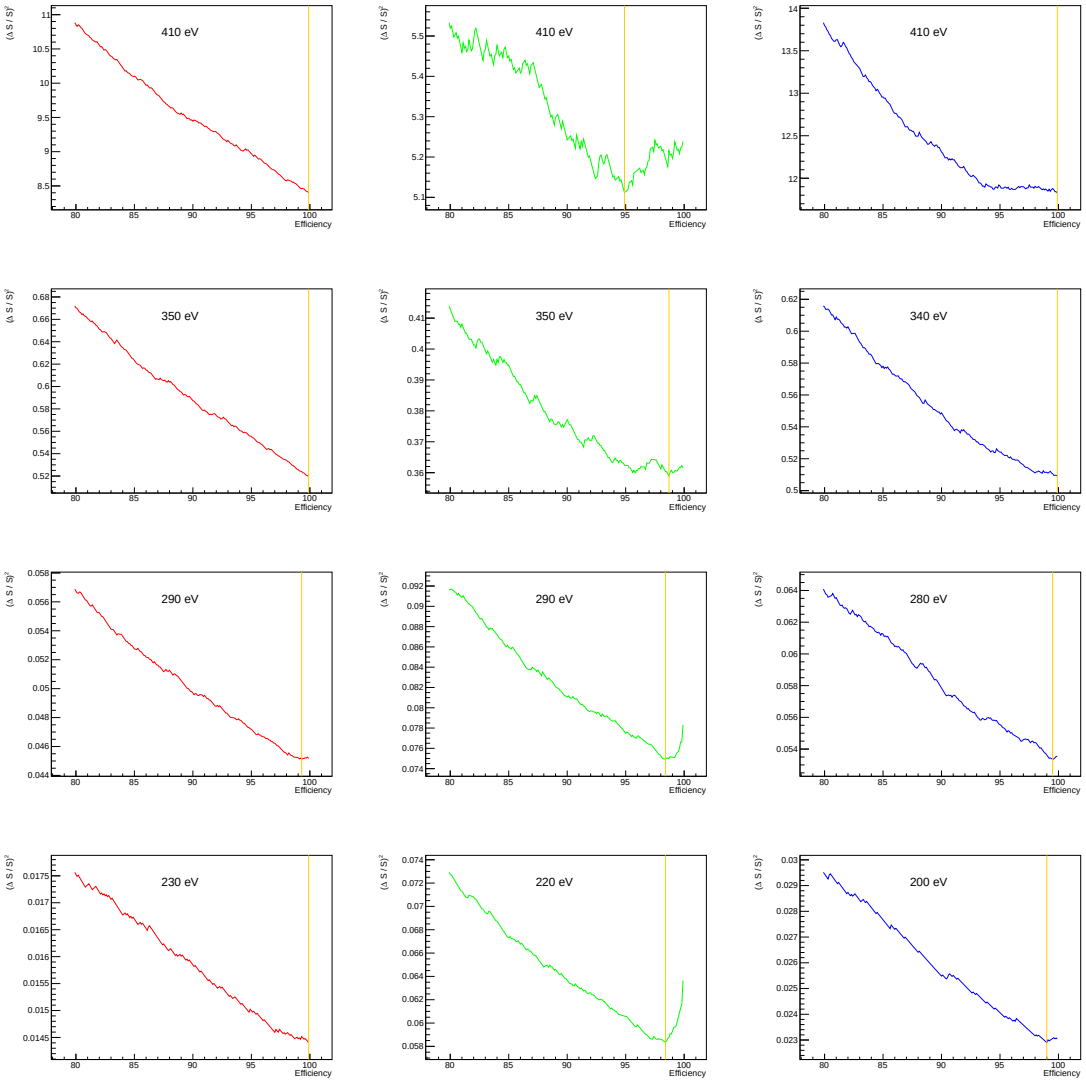

Figure B.1. The figures of merit done in the same way as figure 5.3. The first column (red curves) correspond to C2, the middle (green) to C3 and the last (blue) to C4.

B.2. Stability monitoring plots for C2-C4

The C2 and C4 detector seem to exhibit a trend towards higher risetimes in the Th-228 data, especially the C2 detector with a range of 2.8 ns within roughly one year. This needs to be further monitored and might also help to examine the performance of the diode and the preamplifier over longer time scales.
The stability of the τ-parameter of the pulser is worse for C2-C4 compared to C1, again C2 is by far the most unstable detector. These data, however, are not taken with the modified input pulses but rather just exponential decay pulses. Furthermore, the settings or the used attenuators strength might have changed, even the use of a signal splitter has a large impact. Hence, these data need to be taken with great care. A continuous monitoring with the modified input pulses is definitely desirable.

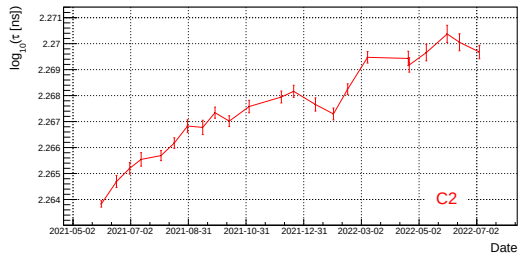

(a) τ-stability of the data.

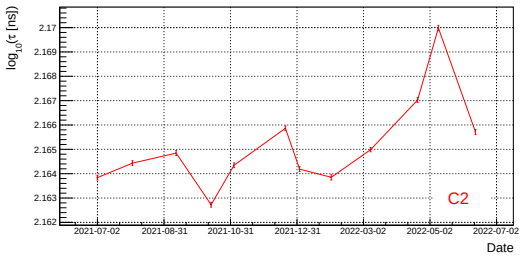

(b) τ-stability of the pulser.

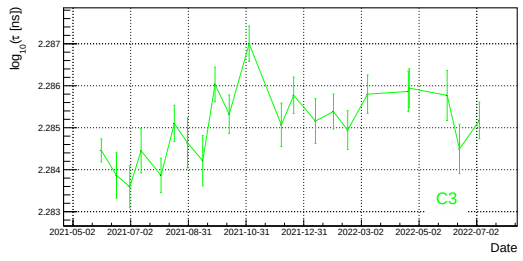

(c) τ-stability of the data.

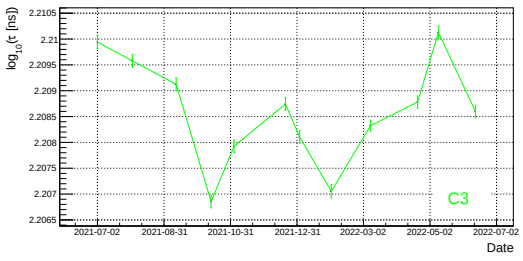

(d) τ-stability of the pulser.

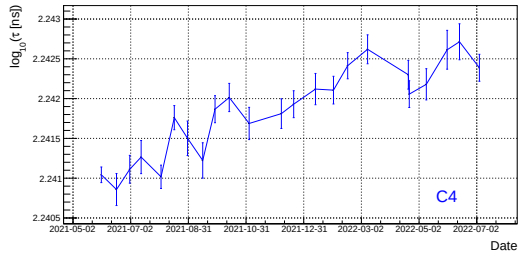

(e) τ-stability of the data.

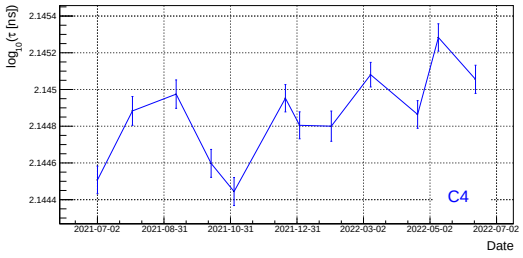

(f) τ-stability of the pulser.

Figure B.2. Stability monitoring of the τ-parameters over time for the detectors C2-C4.

References

[1] Y. Fukuda et al. "Evidence for oscillation of atmospheric neutrinos." In: *Phys. Rev. Lett.* 81 (1998), pp. 1562–1567. arXiv: hep-ex/9807003.

[2] Mohammad Sajjad Athar et al. "Status and perspectives of neutrino physics." In: *Prog. Part. Nucl. Phys.* 124 (2022), p. 103947. arXiv: 2111.07586 [hep-ph].

[3] P. A. Zyla et al. "Review of Particle Physics." In: *PTEP* 2020.8 (2020), p. 083C01.

[4] W. Pauli. "Dear radioactive ladies and gentlemen." In: *Phys. Today* 31N9 (1978), p. 27.

[5] Enrico Fermi. "Tentativo di una teoria dell'emissione dei raggi beta." In: *Ric. Sci.* 4 (1933), pp. 491–495.

[6] J. Chadwick. "Possible Existence of a Neutron." In: *Nature* 129 (1932), p. 312.

[7] C. L. Cowan et al. "Detection of the free neutrino: A Confirmation." In: *Science* 124 (1956), pp. 103–104.

[8] Francesco Vissani. "Neutrino Sources and Properties." In: *PoS* GSSI14 (2015), p. 001. arXiv: 1412.8386 [hep-ph].

[9] B. T. Cleveland et al. "Measurement of the solar electron neutrino flux with the Homestake chlorine detector." In: *Astrophys. J.* 496 (1998), pp. 505–526.

[10] John N. Bahcall and M. H. Pinsonneault. "Standard solar models, with and without helium diffusion and the solar neutrino problem." In: *Rev. Mod. Phys.* 64 (1992), pp. 885–926.

[11] S. Fukuda et al. "Constraints on neutrino oscillations using 1258 days of Super-Kamiokande solar neutrino data." In: *Phys. Rev. Lett.* 86 (2001), pp. 5656–5660. arXiv: hep-ex/0103033.

[12] Q. R. Ahmad et al. "Direct evidence for neutrino flavor transformation from neutral current interactions in the Sudbury Neutrino Observatory." In: *Phys. Rev. Lett.* 89 (2002), p. 011301. arXiv: nucl-ex/0204008.

[13] K. H. Ackermann et al. "The GERDA experiment for the search of $0\nu\beta\beta$ decay in ^{76}Ge." In: *Eur. Phys. J. C* 73.3 (2013), p. 2330. arXiv: 1212.4067 [physics.ins-det].

[14] N. Abgrall et al. "The Large Enriched Germanium Experiment for Neutrinoless Double Beta Decay (LEGEND)." In: *AIP Conf. Proc.* 1894.1 (2017). Ed. by Osvaldo Civitarese, Ivan Stekl, and Jouni Suhonen, p. 020027. arXiv: 1709.01980 [physics.ins-det].

[15] L. Gastaldo et al. "The electron capture in^{163}Ho experiment – ECHo." In: *Eur. Phys. J. ST* 226.8 (2017), pp. 1623–1694.

[16] M. Aker et al. "Improved Upper Limit on the Neutrino Mass from a Direct Kinematic Method by KATRIN." In: *Phys. Rev. Lett.* 123.22 (2019), p. 221802. arXiv: 1909.06048 [hep-ex].

[17] Babak Abi et al. "Deep Underground Neutrino Experiment (DUNE), Far Detector Technical Design Report, Volume I Introduction to DUNE." In: *JINST* 15.08 (2020), T08008. arXiv: 2002.02967 [physics.ins-det].

[18] K. Abe et al. "Physics potential of a long-baseline neutrino oscillation experiment using a J-PARC neutrino beam and Hyper-Kamiokande." In: *PTEP* 2015 (2015), p. 053C02. arXiv: 1502.05199 [hep-ex].

[19] Fengpeng An et al. "Neutrino Physics with JUNO." In: *J. Phys. G* 43.3 (2016), p. 030401. arXiv: 1507.05613 [physics.ins-det].

[20] J. Ashenfelter et al. "The PROSPECT Physics Program." In: *J. Phys. G* 43.11 (2016), p. 113001. arXiv: 1512.02202 [physics.ins-det].

[21] N. Allemandou et al. "The STEREO Experiment." In: *JINST* 13.07 (2018), P07009. arXiv: 1804.09052 [physics.ins-det].

[22] M. G. Aartsen et al. "Evidence for High-Energy Extraterrestrial Neutrinos at the IceCube Detector." In: *Science* 342 (2013), p. 1242856. arXiv: 1311.5238 [astro-ph.HE].

[23] S. Adrian-Martinez et al. "Letter of intent for KM3NeT 2.0." In: *J. Phys. G* 43.8 (2016), p. 084001. arXiv: 1601.07459 [astro-ph.IM].

[24] Daniel Z. Freedman. "Coherent effects of a weak neutral current." In: *Phys. Rev. D* 9 (5 1974), pp. 1389–1392.

[25] D. Akimov et al. "Observation of Coherent Elastic Neutrino-Nucleus Scattering." In: *Science* 357.6356 (2017), pp. 1123–1126. arXiv: 1708.01294 [nucl-ex].

[26] H. -Th. Janka. "Neutrino Emission from Supernovae." In: (2017). arXiv: 1702.08713 [astro-ph.HE].

[27] James R. Wilson. "Coherent Neutrino Scattering and Stellar Collapse." In: *Phys. Rev. Lett.* 32 (15 1974), pp. 849–852.

[28] Adam Bernstein et al. "*Colloquium*: Neutrino detectors as tools for nuclear security." In: *Rev. Mod. Phys.* 92 (2020), p. 011003. arXiv: 1908.07113 [physics.soc-ph].

[29] Amir N. Khan and Werner Rodejohann. "New physics from COHERENT data with an improved quenching factor." In: *Phys. Rev. D* 100.11 (2019), p. 113003. arXiv: 1907.12444 [hep-ph].

[30] Manfred Lindner, Werner Rodejohann, and Xun-Jie Xu. "Coherent Neutrino-Nucleus Scattering and new Neutrino Interactions." In: *Journal of High Energy Physics* 2017 (2016).

[31] Thomas Rink. "Investigating Neutrino Physics within and beyond the Standard Model using CONUS Experimental Data." PhD thesis. U. Heidelberg, 2022.

[32] Jocelyn Monroe and Peter Fisher. "Neutrino Backgrounds to Dark Matter Searches." In: *Phys. Rev. D* 76 (2007), p. 033007. arXiv: 0706.3019 [astro-ph].

[33] Louis E. Strigari. "Neutrino Coherent Scattering Rates at Direct Dark Matter Detectors." In: *New J. Phys.* 11 (2009), p. 105011. arXiv: 0903.3630 [astro-ph.CO].

[34] E. Aprile et al. "Search for Coherent Elastic Scattering of Solar ^{8}B Neutrinos in the XENON1T Dark Matter Experiment." In: *Phys. Rev. Lett.* 126 (2021), p. 091301. arXiv: 2012.02846 [hep-ex].

[35] Guillermo Fernandez Moroni et al. "Charge Coupled Devices for detection of coherent neutrino-nucleus scattering." In: *Phys. Rev. D* 91.7 (2015), p. 072001. arXiv: 1405.5761 [physics.ins-det].

[36] R. Strauss et al. "Gram-scale cryogenic calorimeters for rare-event searches." In: *Phys. Rev. D* 96.2 (2017), p. 022009. arXiv: 1704.04317 [physics.ins-det].

[37] V. Chepel and H. Araujo. "Liquid noble gas detectors for low energy particle physics." In: *JINST* 8 (2013), R04001. arXiv: 1207.2292 [physics.ins-det].

[38] H. Bonet et al. "Large-size sub-keV sensitive germanium detectors for the CONUS experiment." In: *Eur. Phys. J. C* 81.3 (2021), p. 267. arXiv: 2010.11241 [physics.ins-det].

[39] H. Bonet et al. "Constraints on Elastic Neutrino Nucleus Scattering in the Fully Coherent Regime from the CONUS Experiment." In: *Phys. Rev. Lett.* 126.4 (2021), p. 041804. arXiv: 2011.00210 [hep-ex].

[40] CAEN. *V1782 - Octal 32K Digital Multi Channel Analyzer*. https://www.caen.it/products/v1782/, accessed 2022-11-06.

[41] Mirion Technologies. *Lynx Digital Signal Analyzer*. https://www.mirion.com/products/lynx-digital-signal-analyzer, accessed 2022-11-06.

[42] L. T. Yang et al. "Bulk and Surface Event Identification in p-type Germanium Detectors." In: *Nucl. Instrum. Meth. A* 886 (2018), pp. 13–23. arXiv: 1611.03357 [physics.ins-det].

[43] H. B. Li et al. "Differentiation of Bulk and Surface Events in p-type Point-Contact Germanium Detectors for Light WIMP Searches." In: *Astropart. Phys.* 56 (2014), pp. 1–8. arXiv: 1311.5957 [physics.ins-det].

[44] C. E. Aalseth et al. "CoGeNT: A Search for Low-Mass Dark Matter using p-type Point Contact Germanium Detectors." In: *Phys. Rev. D* 88 (2013), p. 012002. arXiv: 1208.5737 [astro-ph.CO].

[45] A. K. Soma et al. "Characterization and Performance of Germanium Detectors with sub-keV Sensitivities for Neutrino and Dark Matter Experiments." In: *Nucl. Instrum. Meth. A* 836 (2016), pp. 67–82. arXiv: 1411.4802 [physics.ins-det].

[46] Dusan Budjas et al. "Pulse shape discrimination studies with a Broad-Energy Germanium detector for signal identification and background suppression in the GERDA double beta decay experiment." In: *JINST* 4 (2009), P10007. arXiv: 0909.4044 [nucl-ex].

[47] J. Henrichs. "Development of a Pulse Shape Analysis for the CONUS Experiment." Master's thesis. Heidelberg University, 2021.

[48] Kevin Scott McFarland. "Neutrino Interactions." In: *61st Scottish Universities Summer School in Physics: Neutrinos in Particle Physics, Astrophysics and Cosmology (SUSSP61)*. 2008, pp. 65–90. arXiv: 0804.3899 [hep-ex].

[49] P. Vogel and John F. Beacom. "Angular distribution of neutron inverse beta decay, anti-neutrino(e) + p —> e+ + n." In: *Phys. Rev. D* 60 (1999), p. 053003. arXiv: hep-ph/9903554.

[50] M. Agostini et al. "Limiting neutrino magnetic moments with Borexino Phase-II solar neutrino data." In: *Phys. Rev. D* 96.9 (2017), p. 091103. arXiv: 1707.09355 [hep-ex].

[51] Janina Dorin Hakenmüller. "Looking for coherent elastic neutrino nucleus scattering with the CONUS experiment." PhD thesis. U. Heidelberg, 2020.

[52] B. C. Cañas et al. "Future perspectives for a weak mixing angle measurement in coherent elastic neutrino nucleus scattering experiments." In: *Phys. Lett. B* 784 (2018), pp. 159–162. arXiv: 1806.01310 [hep-ph].

[53] W. N. Cottingham and D. A. Greenwood. *An Introduction to the Standard Model of Particle Physics*. 2nd ed. Cambridge University Press, 2007.

[54] Philip S. Amanik and Gail C. McLaughlin. "Neutron Form Factor from Neutrino-Nucleus Coherent Elastic Scattering." In: (2007). arXiv: 0707.4191 [hep-ph].

[55] Julien Billard et al. "Direct detection of dark matter—APPEC committee report∗." In: *Reports on Progress in Physics* 85.5 (2022), p. 056201.

[56] H. Bonet et al. "First limits on neutrino electromagnetic properties from the CONUS experiment." In: (2022). arXiv: 2201.12257 [hep-ex].

[57] H. Bonet et al. "Novel constraints on neutrino physics beyond the standard model from the CONUS experiment." In: *Journal of High Energy Physics* 2022.5 (2022).

[58] G. C. McLaughlin and C. Volpe. "Prospects for detecting a neutrino magnetic moment with a tritium source and beta beams." In: *Phys. Lett. B* 591 (2004), pp. 229–234. arXiv: hep-ph/0312156.

[59] T. Lasserre and H. W. Sobel. "Reactor neutrinos." In: *Comptes Rendus Physique* 6 (2005), pp. 749–757. arXiv: nucl-ex/0601013.

[60] A. Bolozdynya et al. "Opportunities for Neutrino Physics at the Spallation Neutron Source: A White Paper." In: 2012. arXiv: 1211.5199 [hep-ex].

[61] C. Bellenghi et al. "Coherent elastic nuclear scattering of^{51} Cr neutrinos." In: *Eur. Phys. J. C* 79.9 (2019), p. 727. arXiv: 1905.10611 [physics.ins-det].

[62] D. Akimov et al. "COHERENT 2018 at the Spallation Neutron Source." In: (2018). arXiv: 1803.09183 [physics.ins-det].

[63] F. P. An et al. "First measurement of high-energy reactor antineutrinos at Daya Bay." In: (2022). arXiv: 2203.06686 [hep-ex].

[64] A. G. Beda et al. "First Result for Neutrino Magnetic Moment from Measurements with the GEMMA Spectrometer." In: *Phys. Atom. Nucl.* 70 (2007), pp. 1873–1884. arXiv: 0705.4576 [hep-ex].

[65] D. Akimov et al. "First Measurement of Coherent Elastic Neutrino-Nucleus Scattering on Argon." In: *Phys. Rev. Lett.* 126.1 (2021), p. 012002. arXiv: 2003.10630 [nucl-ex].

[66] A. Aguilar-Arevalo et al. "The CONNIE experiment." In: *J. Phys. Conf. Ser.* 761.1 (2016). Ed. by Eduard de la Cruz Burelo, Arturo Fernandez Tellez, and Pablo Roig, p. 012057. arXiv: 1608.01565 [physics.ins-det].

[67] V. Belov et al. "The νGeN experiment at the Kalinin Nuclear Power Plant." In: *JINST* 10.12 (2015), P12011.

[68] H. T. Wong. "The TEXONO research program on neutrino and astroparticle physics." In: *Mod. Phys. Lett. A* 19 (2004). Ed. by W. Y. Pauchy Hwang, Guey-Lin Lin, and J. H. P. Wu, pp. 1207–1214.

[69] D. Yu Akimov et al. "First ground-level laboratory test of the two-phase xenon emission detector RED-100." In: *JINST* 15.02 (2020), P02020. arXiv: 1910.06190 [physics.ins-det].

[70] R. Strauss et al. "The ν-cleus experiment: A gram-scale fiducial-volume cryogenic detector for the first detection of coherent neutrino-nucleus scattering." In: *Eur. Phys. J. C* 77 (2017), p. 506. arXiv: 1704.04320 [physics.ins-det].

[71] J Lindhard. "Influence of Crystal Lattice on Motion of Energetic Charged Particles." In: *Kongel. Dan. Vidensk. Selsk., Mat.-Fys. Medd.* 34.14 (1965).

[72] C. Chasman et al. "Measurement of the Energy Loss of Germanium Atoms to Electrons in Germanium at Energies below 100 keV. II." In: *Phys. Rev.* 154 (2 1967), pp. 239–244.

[73] A. Bonhomme et al. "Direct measurement of the ionization quenching factor of nuclear recoils in germanium in the keV energy range." In: (2022). arXiv: 2202.03754 [physics.ins-det].

[74] Preussen Elektra GmbH. *Kernkraftwerk Brokdorf*. https://www.preussenelektra.de/de/unsere-kraftwerke/kraftwerkbrokdorf.html, accessed 2022-09-06.

[75] G. Alimonti et al. "The Borexino detector at the Laboratori Nazionali del Gran Sasso." In: *Nucl. Instrum. Meth. A* 600 (2009), pp. 568–593. arXiv: 0806.2400 [physics.ins-det].

[76] G. Heusser. "Low-radioactivity background techniques." In: *Ann. Rev. Nucl. Part. Sci.* 45 (1995), pp. 543–590.

[77] Gerd Heusser et al. "GIOVE - A new detector setup for high sensitivity germanium spectroscopy at shallow depth." In: *Eur. Phys. J. C* 75.11 (2015), p. 531. arXiv: 1507.03319 [astro-ph.IM].

[78] H. Bonet et al. "Full background decomposition of the CONUS experiment." In: (2021). arXiv: 2112.09585 [physics.ins-det].

[79] L. Pattavina et al. "Radiopurity of an archaeological Roman lead cryogenic detector." In: *Eur. Phys. J. A* 55.8 (2019), p. 127. arXiv: 1904.04040 [physics.ins-det].

[80] J. Hakenmüller et al. "Neutron-induced background in the CONUS experiment." In: *Eur. Phys. J. C* 79.8 (2019), p. 699. arXiv: 1903.09269 [physics.ins-det].

[81] Gordon R. Gilmore. *Practical Gamma-Ray Spectrometry*. John Wiley & Sons, Ltd, 2008. Chap. 3, pp. 39–60.

[82] R. Arts D. Willems and J. Douwen. "State-of-the art cryocooler solutions for HPGe detectors." Technical Paper. Mirion technologies, 2015.

[83] Lingolsheim Office Mirion Technologies (Canberra) SAS. https://www.mirion.com/mirion-technologies-canberra-sas-lingolsheim, accessed 2022-12-06.

[84] Zhong He. "Review of the Shockley–Ramo theorem and its application in semiconductor gamma-ray detectors." In: *Nuclear Instruments and Methods in Physics Research Section A: Accelerators, Spectrometers, Detectors and Associated Equipment* 463 (2001), pp. 250–267.

[85] Dusan Budjas. "Germanium detector studies in the framework of the GERDA experiment." PhD thesis. U. Heidelberg (main), 2009.

[86] G. Knoll. *Radiation Detection and Measurement*. 2000.

[87] Valentin T. Jordanov and Glenn F. Knoll. "Digital synthesis of pulse shapes in real time for high resolution radiation spectroscopy." In: *Nuclear Instruments & Methods in Physics Research Section A-accelerators Spectrometers Detectors and Associated Equipment* 345 (1994), pp. 337–345.

[88] CAEN. *CoMPASS - Multiparametric DAQ Software for Physics Applications*. https://www.caen.it/products/compass/, accessed 2022-14-06.

[89] CAEN. *V1725 - 16/8 Channel 14-bit 250 MS/s Digitizer*. https://www.caen.it/products/v1725/, accessed 2022-14-06.

[90] C. E. Aalseth et al. "Results from a Search for Light-Mass Dark Matter with a P-type Point Contact Germanium Detector." In: *Phys. Rev. Lett.* 106 (2011), p. 131301. arXiv: 1002.4703 [astro-ph.CO].

[91] Tektronix. *AFG 3252 - 240 MHz, 2-Ch Arbitrary Function Generator*. https://www.tek.com/en/signal-generator/afg3000-manual/afg3000-series-2, accessed 2022-18-06.

[92] Gang Li, Liping Chang, and Sheng Li. *Signals and systems. fundamentals*. eng. De Gruyter textbook. Berlin ; Boston: De Gruyter [u.a.], 2015, XV, 267 S.

[93] B.R. Hunt. "The inverse problem of radiography." In: *Mathematical Biosciences* 8.1 (1970), pp. 161–179.

[94] B. Hunt. "A theorem on the difficulty of numerical deconvolution." In: *IEEE Transactions on Audio and Electroacoustics* 20.1 (1972), pp. 94–95.

[95] T. Ullrich and Z. Xu. *Treatment of Errors in Efficiency Calculations*. 2007.

[96] Marc F. Paterno. "Calculating efficiencies and their uncertainties." In: 2004.

[97] Diego Casadei. "Estimating the selection efficiency." In: *JINST* 7 (2012), P08021. arXiv: 0908.0130 [physics.data-an].

[98] G. Cowan. "Error Analysis for efficiency." In: 2008.

[99] D. Akimov et al. "The COHERENT Experimental Program." In: *2022 Snowmass Summer Study*. 2022. arXiv: 2204.04575 [hep-ex].

[100] G. Angloher et al. "Exploring CEνNS with NUCLEUS at the Chooz nuclear power plant." In: *Eur. Phys. J. C* 79.12 (2019), p. 1018. arXiv: 1905.10258 [physics.ins-det].

List of Figures

List of Tables

Acknowledgements

First of all, I would like to thank Prof. Dr. Dr. h.c. Manfred Lindner for the opportunity to carry out this thesis in his division at the Max-Planck Institut für Kernphysik. Further, I want to thank all the members of the CONUS collaborations for the joyful and productive discussions at the insitute. Since I never got the approval to enter the nuclear power plant I want to give special thanks to all the shifters who conducted many measurements for me at the KBR. Most of all, I like to thank my co-supervisor Dr. Aurélie Bonhomme for her constant support and help with every problem. I am further grateful for the proof-reading of Dr. Werner Maneschg . Special gratitude is directed to my classmates/friends since the first Bachelor semester for the proofreading of this thesis and for all the physics and not physics related discussions throughout the years. Further, I would like to thank apl. Prof. Dr. Monica Dunford, the second examiner of this thesis.

Declaration of Authorship

I hereby certify that this thesis has been composed by me and is based on my own work, unless stated otherwise.

Heidelberg, 20.08.22